The Astrophysical Journal, 994:233 (42pp), 2025 December 1 https://doi.org/10.3847/1538-4357/ae0619

ALMA-IMF. XX. Core Fragmentation in the W51 High-mass Star-forming Region

T. Yoo[1,27], A. Ginsburg[1], J. Braine[2], N. Budaiev[1], F. Louvet[3,4], F. Motte[3], A. M. Stutz[5], B. Thomasson[3], M. Armante[6,7], M. Bonfand[8], S. Bontemps[2], L. Bronfman[9], G. Busquet[10,11,12], T. Csengeri[2], N. Cunningham[13], J. Di Francesco[14], D. J. Díaz-González[15], M. Fernández-Lopez[16], R. Galván-Madrid[15], C. Goddi[17,18,19], A. Gusdorf[6,7], N. Kessler[2], A. Koley[5], H.-L Liu[20], T. Nony[15,21], F. Olguin[22], P. Sanhueza[23,24,25], M. Valeille-Manet[2], L. A. Zapata[15], and Q. Zhang[26]

[1] Department of Astronomy, University of Florida, PO Box 112055, FL, USA; astro.taehwa.yoo@gmail.com
[2] Laboratoire d'Astrophysique de Bordeaux, University of Bordeaux, CNRS, B18N, Allée Geoffroy Saint-Hilaire, 33615 Pessac, France
[3] University of Grenoble Alpes, CNRS, IPAG, 38000 Grenoble, France
[4] DAS, Universidad de Chile, 1515 Camino el Observatorio, Las Condes, Santiago, Chile
[5] Departamento de Astronomía, Universidad de Concepción, Casilla 160-C, Concepción, Chile
[6] Laboratoire de Physique de l'École Normale Supérieure, ENS, Université PSL, CNRS, Sorbonne Université, Université de Paris, Paris, France
[7] Observatoire de Paris,Université PSL, Sorbonne Université, LERMA, 75014 Paris, France
[8] Departments of Astronomy and Chemistry, University of Virginia, Charlottesville, VA 22904, USA
[9] Departamento de Astronomía, Universidad de Chile, Casilla 36-D, Santiago, Chile
[10] Departament de Féisica Quàntica i Astrofísica (FQA), Universitat de Barcelona, Martí i Franquès 1, E-08028 Barcelona, Catalonia, Spain
[11] Institut de Ciències del Cosmos (ICCUB), Universitat de Barcelona, Martí i Franquès 1, E-08028 Barcelona, Catalonia, Spain
[12] Institut d'Estudis Espacials de Catalunya (IEEC), Esteve Terradas 1, Edifici RDIT, Parc Mediterrani de la Tecnologia (PMT) Campus del Baix Llobregat - UPC 08860 Castelldefels (Barcelona), Catalonia, Spain
[13] SKA Observatory, Jodrell Bank, Lower Withington, Macclesfield, SK11 9FT, UK
[14] Herzberg Astronomy and Astrophysics Research Centre, National Research Council of Canada, 5071 West Saanich Road, Victoria, Canada
[15] Instituto de Radioastronomía y Astrofísica, Universidad Nacional Autónoma de México, Morelia, Michoacán 58089, Mexico
[16] Instituto Argentino de Radioastronomía (CCT-La Plata, CONICET; CICPBA), C.C. No. 5, 1894, Villa Elisa, Buenos Aires, Argentina
[17] Instituto de Astronomia, Geofísica e Ciências Atmosféricas, Universidade de São Paulo, R. do Matão, 1226 São Paulo, SP 05508-090, Brazil
[18] Dipartimento di Fisica, Universitá degli Studi di Cagliari, SP Monserrato-Sestu km 0.7, 09042 Monserrato (CA), Italy
[19] INAF—Osservatorio Astronomico di Cagliari, Via Della Scienza 5, 09047 Selargius (CA), Italy
[20] School of Physics and Astronomy, Yunnan University, Kunming 650091, People's Republic of China
[21] INAF—Osservatorio Astrofisico di Arcetri, Largo Enrico Fermi 5, 50125 Firenze, Italy
[22] Institute of Astronomy, National Tsing Hua University, Hsinchu 30013, Taiwan
[23] Department of Astronomy, School of Science, The University of Tokyo, 7-3-1 Hongo, Bunkyo, Tokyo 113-0033, Japan
[24] National Astronomical Observatory of Japan, National Institutes of Natural Sciences, 2-21-1 Osawa, Mitaka, Tokyo 181-8588, Japan
[25] Institute of Astronomy and Department of Physics, National Tsing Hua University, Hsinchu 30013, Taiwan
[26] Center for Astrophysics, Harvard & Smithsonian, 60 Garden Street, Cambridge, MA 02138, USA
Received 2025 February 27; revised 2025 September 3; accepted 2025 September 5; published 2025 November 27

Abstract

We present a study of core fragmentation in the W51-E and W51-IRS2 protoclusters in the W51 high-mass star-forming region. The identification of core fragmentation is achieved by the spatial correspondence of cores and compact sources, which are detected in the short- (low-resolution) and the long-baseline (high-resolution) continuum images from the Atacama Large Millimeter/submillimeter Array (ALMA) in Bands 3 (3 mm) and 6 (1.3 mm), respectively. We characterize the compact sources found in the long-baseline images, and conclude that the compact sources are pre-/protostellar objects (PPOs) that are either prestellar dust cores or dust disks or envelopes around protostars. The observed trend of core fragmentation in W51 is that (i) massive cores host more PPOs, (ii) bright PPOs are preferentially formed in massive cores, and (iii) equipartition of flux between PPOs is uncommon. The thermal Jeans masses of the parent cores are insufficient to explain the masses of their fragments, and this trend is more prominent for high-mass cores. We also find that unfragmented cores are large, less massive, and less dense than fragmented cores.

Unified Astronomy Thesaurus concepts: Star formation (1569); Star forming regions (1565); Protoclusters (1297); Initial mass function (796); Millimeter astronomy (1061)

1. Introduction

Unveiling the origin of stellar masses is of great importance to many astrophysical fields. Not only is it an ultimate question in star formation theory, but also the stellar initial mass function (IMF) is a keystone to build models of galaxies, stellar clusters, and planet formation since the initial stellar mass is the most important factor in determining stellar evolution. One of the remaining unresolved problems is whether the IMF is universal. While the observations for nearby clusters show almost invariant IMFs (see the references in N. Bastian et al. 2010; S. S. R. Offner et al. 2014; M. R. Krumholz 2015), extending the targets to diverse environments, e.g., the Galactic center (e.g., J. R. Lu et al. 2013; M. W. J. Hosek et al. 2019), other nearby galaxies (e.g., D. R. Weisz et al. 2015; T. M. Wainer et al. 2024), and young massive clusters of the Galaxy (e.g., F. F. S. Maia et al. 2016), provide some cases where the IMF slope has nonnegligible scatter and deviation from the canonical slope ($dN/M \equiv \alpha = -2.35$; E. E. Salpeter 1955).

[27] Corresponding author.

Observations resolving the internal structure of molecular clouds has shown that they collapse under self-gravity into dense substructures, known as cores (which have $r \sim 0.01$–0.3 pc), which are the first stage in the formation of new stars. The mass function of these structures, the core mass function (CMF), has often been found in nearby, low-mass protoclusters, to have a similar shape to the stellar IMF (e.g., F. Motte et al. 1998; J. Alves et al. 2007; R. J. Simpson et al. 2008; P. André et al. 2010). However, in high-mass star-forming protoclusters, the high-mass end of the CMF has been found to have a top-heavy (shallow) slope compared with the standard IMF (e.g., F. Motte et al. 2018; S. Kong 2019; P. Sanhueza et al. 2019; X. Lu et al. 2020; Y. Pouteau et al. 2022; T. Nony et al. 2023; F. Louvet et al. 2024).

Overall, the primary parameter for setting the initial stellar mass is still an open question. The turbulent fragmentation model (e.g., P. Padoan & Å. Nordlund 2002) suggested that the power-law slope of the CMF derives from the density distribution of the supersonic turbulent interstellar medium (ISM) and demonstrated that the slope of the CMF is consistent with that of the Salpeter IMF (E. E. Salpeter 1955). On the other hand, mass accretion onto cores has been suggested as another process affecting the initial stellar masses. For instance, the competitive accretion model (e.g., I. A. Bonnell et al. 2001; I. A. Bonnell & M. R. Bate 2002) suggested the picture that star-forming cores grow by competing with each other for gas accretion, and the initial core mass in this model is less important in setting the initial stellar masses. A recent numerical study, P. Padoan et al. (2020), proposed an initial inflow model where the gas inflow generated by supersonic turbulence has a more dominant role in setting stellar mass than the inertial core mass.

One important process affecting the transition between the CMF and the IMF is core fragmentation. S. S. R. Offner et al. (2014) suggested that several conditions, including that there is the same degree of core fragmentation over the full mass range, are required to maintain the same power-law slope of the CMF to the IMF. Over the decades, several analytic models of fragmentation have been developed. D. Guszejnov & P. F. Hopkins (2015) established an analytic model of core fragmentation based on the turbulent fragmentation scheme, and found a slightly flatter CMF slope ($\alpha = -2.1$) compared with the IMF slope ($\alpha = -2.3$). On the other hand, E. Vázquez-Semadeni et al. (2019) proposed the global hierarchical collapse model where gravitational infall rather than supersonic turbulence induces fragmentation (as initially suggested by F. Hoyle 1953).

Early observations of massive dense cores or clumps at a scale of ∼0.1 pc have revealed that they host condensations or fragments in high spatial resolution images (e.g., Q. Zhang et al. 2009; S. Bontemps et al. 2010; Q. Zhang et al. 2015). With the advent of new telescopes such as the Submillimeter Array and the Atacama Large Millimeter/submillimeter Array (ALMA), observations of smaller structures have been conducted for nearby, low-mass, star-forming regions (e.g., R. Pokhrel et al. 2018) and high-mass, star-forming regions at a farther distances (e.g., A. Palau et al. 2021; M. Tang et al. 2022; N. Budaiev et al. 2024; S. Li et al. 2024). A study of the Perseus star-forming region compiled various observational data with five different spatial scales—the entire cloud, clumps, cores, envelopes, and protostellar objects— and showed that the thermal Jeans mass is not high enough to explain the observed number of core fragments (R. Pokhrel et al. 2018). A. Palau et al. (2021) investigated the fragmentation of 18 massive dense cores and found a tentative correlation between the number of fragments and the mass-to-flux ratio, suggesting that magnetic fields could have a role in determining core fragmentation. In contrast, M. Tang et al. (2022) argued that the number of core fragments in the central region of high-mass protocluster W51-IRS2 can be well explained by the thermal Jeans mass.

In this study, we utilize ALMA millimeter-wavelength observational data of the W51 star-forming complex, which is the nearest (5.1–5.41 kpc; Y. Xu et al. 2009; M. Sato et al. 2010) extreme high-mass ($M \gtrsim 10^4\ M_\odot$; M. S. N. Kumar et al. 2004) star-forming region in the Milky Way (see the review by A. Ginsburg 2017). The main star-forming region, W51-A, has two subregions that are protoclusters, W51-E and W51-IRS2. This cloud is one of the best targets to study high-mass star formation given its very young age ($\lesssim$1 Myr; S.-i. Okumura et al. 2000), such that most of the massive stars are on the (pre-)main sequence; the region is at a very early stage of high-mass star formation (e.g., L. A. Zapata et al. 2009, 2010; A. Ginsburg et al. 2015; A. Ginsburg 2017). The cloud shows abundant evidence of high-mass star formation: hot cores and hypercompact H II (HCH II) regions such as W51e2, W51e8, and W51-North (e.g., Q. Zhang & P. T. P. Ho 1997; A. Ginsburg et al. 2016, 2017; C. Goddi et al. 2016), X-ray stars (e.g., L. K. Townsley et al. 2014), and masers from OH (S. Etoka et al. 2012), H_2O (e.g., R. Genzel et al. 1981; J. A. Eisner et al. 2002; H. Imai et al. 2002), CH_3OH (e.g., C. Phillips & H. J. van Langevelde 2005; S. Etoka et al. 2012), SiO (e.g., K.-I. Morita et al. 1992; J. A. Eisner et al. 2002), CS (A. Ginsburg & C. Goddi 2019), complex molecules (J. Rong et al. 2016), and NH_3 (e.g., R. D. Brown & D. M. Cragg 1991; R. A. Gaume et al. 1993; C. Henkel et al. 2013). W51 therefore provides an optimal laboratory in which to study the formation of the upper end of the IMF.

Two subregions in the W51 cloud, W51-E and W51-IRS2, were targets of the ALMA-IMF large program (F. Motte et al. 2022), surveying embedded massive protocluster with ALMA Band 3 (3 mm) and Band 6 (1.3 mm) continuum images. The physical resolution of the ALMA-IMF image for W51 is ∼2000 au, at the size scale of dust cores. These two protoclusters were recently revisited with higher-resolution (∼100–300 au) ALMA observations (C. Goddi et al. 2020) that detected a considerable number of compact sources. We will use "high-resolution sources" (shortened to "high-res sources") to refer to the compact, centrally peaked sources identified in the high-res images throughout the paper. By spatially associating high-res sources with cores found in low-resolution ALMA-IMF images of W51, we will see how each ALMA-IMF core fragments in a high-mass star-forming region.

The paper is organized as follows. In Section 2, we describe our observational data and the method to identify sources in the continuum images. In Section 3, we characterize the sources. In Section 4, we investigate core fragmentation by linking cores and fragments, and we analyze the behavior of fragmentation as a function of core mass. In Section 5, we discuss whether core fragmentation follows Jeans fragmentation and compare the physical properties of unfragmented and fragmented cores. In Section 6, we summarize our main results and discuss the implication of this study in terms of high-mass star formation models and the relation between the CMF and the IMF.

2. Observational Data

In this section, we introduce the archival data we used for this study and the data reduction process. For the ALMA-IMF data set, we illustrate the core catalog extracted from the continuum images.

2.1. ALMA-IMF Continuum Images and Core Catalog

We utilized the 3 mm (Band 3) and 1.3 mm (Band 6) continuum archival data of the W51 from the ALMA large program ALMA-IMF (2017.1.01355.L, PIs: Motte, Ginsburg, Louvet, and Sanhueza; A. Ginsburg et al. 2022; F. Motte et al. 2022). The continuum images are obtained from 12 m array mosaic observations. As summarized in Table 2 of F. Motte et al. (2022), the 3 mm and 1.3 mm continuum images of W51-E have fields of view of $150'' \times 160''$ and $100'' \times 90''$, and angular resolutions of $0''.28$ and $0''.30$, respectively. For W51-IRS2, the fields of view of 3 mm and 1.3 mm are $160'' \times 150''$ and $92'' \times 98''$, and the angular resolutions are $0''.27$ and $0''.48$, respectively. We use `cleanest` continuum images, which use only the line-free channels, in this study. The detailed data processing of the continuum image is described in F. Motte et al. (2022) and A. Ginsburg et al. (2022). A combined continuum image of W51-E and W51-IRS2 is shown in Figure 1.

The physical resolution of the ALMA-IMF continuum image is ∼2000 au, resolving the cores in protoclusters. F. Louvet et al. (2024) extracted cores from the continuum images using the source finding algorithms `getsf` (A. Men'shchikov 2021) and `GExt2D` (S. Bontemps et al. 2025, in preparation). In this study, we used the core catalogs created by `getsf` from the 1.3 mm and 3 mm images smoothed to 2700 au resolution as described in F. Louvet et al. (2024).

Among the 41 and 127 `getsf` sources in W51-E and W51-IRS2, we applied selection criteria to remove unreliable flux and size measurements. We adopt the selection criteria described in A. Men'shchikov (2021) and Y. Pouteau et al. (2022) to filter out sources with a low signal-to-noise ratio (S/N) and high ellipticity in each band. Following the description in Y. Pouteau et al. (2022), we divided the core samples into `getsf` sources with robust 1.3 mm measurements and sources with robust 1.3 mm and 3 mm measurements (Figure 2)—the robust 1.3 mm flux measurement criterion is used to ensure the presence of cores because 1.3 mm flux better traces dust emission, and the 3 mm criterion can be used if 3 mm flux is needed. For the analysis of comparing core fluxes and high-res sources fluxes, we made groups depending on whether cores are found inside the field of view of either the 1.3 mm or 3 mm high-res images. We label three of four groups as follows:

1. *Group A*. Robust 1.3 mm core flux measurement within the field of view of the 3 mm high-res image.
2. *Group B*. Robust 1.3 mm core flux measurement within the field of view of the 1.3 mm high-res image.
3. *Group C*. Robust 1.3 mm and 3 mm core flux measurements within the field of view of the 3 mm high-res image.

The fourth group in Figure 2, i.e., core samples with robust 1.3 mm and 3 mm core flux measurements within the field of view of the 1.3 mm image, is not used in this study because no analyses require this sample.

Note that, the field of view of the 3 mm high-res image includes the whole field of view of the 1.3 mm high-res image. Therefore, core group A provides the largest number of cores. This setup allows us to use different numbers of cores in different situations. For example, we have two options, group A and group B, in using the 1.3 mm core fluxes. The former includes cores outside of the 1.3 mm high-res image field of view; the 1.3 mm fluxes of high-res sources associated with these cores are not measurable. We use group A in the analysis in Section 4.2.1, where the number of fragments can be determined by a single band detection. When we compare the 1.3 mm fluxes of cores and high-res sources, we use the core samples from group B instead. In all analyses using the 3 mm fluxes of cores and high-res sources, we use group C.

In each group, we removed free–free-contaminated sources with a spectral index $\alpha < 2$ (Y. Pouteau et al. 2022; F. Louvet et al. 2024). For those cores where 3 mm flux is not available, a pixel-by-pixel spectral index map was produced; if cores reside in pixels with $\alpha < 1$ then they are discarded (F. Louvet et al. 2024). We further discarded duplicate cores in the overlap between the two regions—#30, #31, and #20 in W51-E, and #38, #108, and #22 in W51-IRS2. We removed these three cores from W51-E. The number of cores in each group is listed in Figure 2.

2.2. High-resolution ALMA Continuum Images

To find the signature of core fragmentation in the W51 region, we utilized archival high-res ALMA data sets from the ALMA cycle 3 program 2015.1.01596.S (PI: C. Goddi) at 1.3 mm and the ALMA cycle 5 program 2017.1.00293.S (PI: A. Ginsburg) at 3 mm observing W51-E and W51-IRS2. Both observations used the 12 m array with a baseline ranging from 85 to 16,196 m. The angular resolution of the continuum images is 27.3 mas × 20.0 mas in 1.3 mm and 66.1 mas × 41.8 mas in 3 mm, corresponding to ∼100–300 au in physical resolution. The central frequency of each image is approximately 86 GHz in Band 3 and 218 GHz in Band 6. Details about the observations in 1.3 mm can be found in C. Goddi et al. (2020).

The data reduction and self-calibration were conducted with the Common Astronomy Software Applications (CASA) package (version 5.7.0; J. P. McMullin et al. 2007). To produce the image files, we run the Python scripts provided with the ALMA raw data, `ScriptforPI.py` and `ScriptforImaging.py`. Then we self-calibrated the images with the script as follows:

1. separate the science data from the whole data set using CASA task `split`;
2. produce a dirty image of the long-baseline data with the `tclean` task;
3. regrid the `startmodel` using the CASA task `imregrid` with the dirty image as a template to make the `startmodel` available for the `tclean` process; and
4. start the eight stages of the iterative phase self-calibration process with `tclean`, `gaincal`, and `applycal`.

During the `tclean` process, we used the ALMA-IMF continuum model image as the `startmodel` to complement the flux from the short baseline. We started our cleaning shallowly and gradually deepened the cleaning process during the iteration to include the diffuse emission into the continuum image. For this reason, we used a gradually decreasing threshold of `tclean` for each step: `threshold` = [0.2, 0.2, 0.15, 0.15, 0.15, 0.15, 0.1, 0.1] mJy for 1.3 mm and [0.1, 0.075, 0.075, 0.075, 0.075, 0.075, 0.075, 0.075] mJy for 3 mm. We also applied two different types of `cleanmask`, the shallower one in steps 1 to 3 and the deeper one in steps 4 to 8. Each mask covers any sources identified by visual inspection from the continuum image. For the weighting scheme, we employed Briggs weighting with `robust` = 0. The `tclean` parameters were chosen as the result of a set of experiments with different parameters. We visually evaluated the quality of the final image produced by self-calibration and tweaked

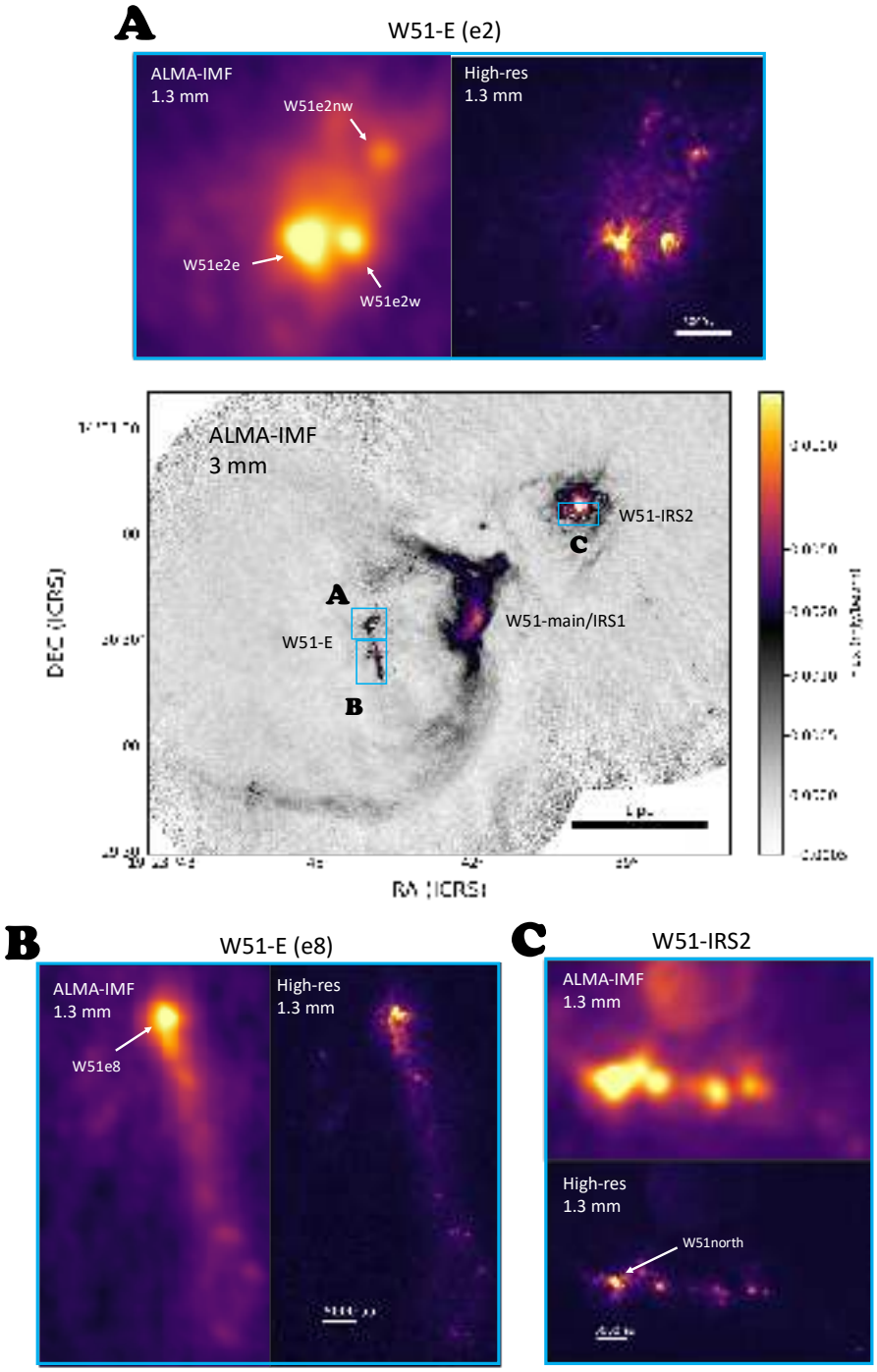

Figure 1. An overview of the W51-A region. The image at the center is the ALMA 3 mm continuum image of ALMA-IMF combining two subregions, W51-E and W51-IRS2. Each continuum image is truncated and merged in the middle to look seamless. Three regions marked with the blue boxes are magnified with the 1.3 mm continuum images from the ALMA-IMF data (left) and high-res data (right). We annotate massive young stellar objects (YSOs) studied in previous studies (e.g., C. Goddi et al. 2020), W51e2 (#39) and W51e8 (#32) in W51-E and W51-North (#11) in W51-IRS2.

parameters to find the optimal set. The parts of the final continuum images in 1.3 mm are displayed in Figure 1.

3. Characterization of High-resolution Sources

In this section, we describe the identification process of high-res sources from the high-res ALMA continuum images. We then present the physical properties of the high-res sources such as spectral indices, sizes, masses, and separations. By doing so, we characterize and classify the high-res sources to better understand the results of the core fragmentation process in high-mass star-forming regions. The characterized properties are summarized in Appendix C.

3.1. High-resolution Source Identification

The high-res ALMA continuum images reveal many compact sources that were unresolved in the ALMA-IMF images (Figure 1). To make a catalog of high-res sources, we visually selected sources that are compact, centrally peaked,

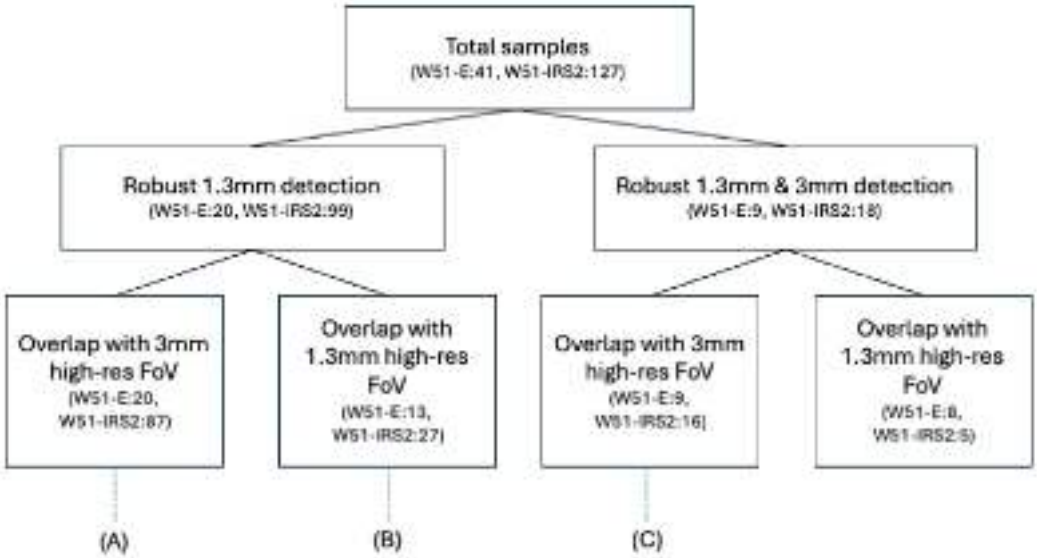

Figure 2. Core groups used in this study. Total ALMA-IMF cores detected in `getsf` are first divided into two groups by the criteria passing a robust 1.3 mm detection or a robust 1.3 mm and 3 mm detection in the `getsf` core catalog. The core samples are further classified into two groups by examining the spatial overlap with the high-res continuum images. The number of cores in each group is listed in parentheses. Each group used in the analyses of this study is labeled.

significant, and independent from the background. Here, a compact source means that we did not include any extended structure, such as filamentary structure or diffuse H II regions (larger than several times the image beam size). However, it is possible that compact sources surrounded by patchy extended emission exist, which still can be identified as high-res sources if the sources are centrally peaked.

To ensure whether the selected sources are significant, we used a watershed-based algorithm (`dendrogram`;[28] E. W. Rosolowsky et al. 2008). The `dendrogram` algorithm finds local maxima and generates a hierarchical tree structure based on the parameters of the minimum value (`min_value`), the minimum significance (`min_delta`), and the minimum number of pixels (`min_npix`). We adopted the following set of parameters, `min_value` $= 3\sigma$, `min_delta` $= 1.5\sigma$, and `min_npix` $= 15$ for our source finding scheme, where σ is the rms noise. Any insignificant visually selected sources that are not matched with `dendrogram`-selected sources are removed from the final catalog.

The high-res sources need to be independent from the background, as the main goal of the source identification is to find fragments. The populated areas of the protocluster are often surrounded by extended emission, which possibly makes compact sources apparently connected to larger structures. Thus, independent sources include any significant peaks that are partially detached from their parent structure. This unavoidably gives rise to some ambiguity in visual selection. To minimize the ambiguity, only sources identified by more than two of the three coauthors (T. Yoo, A. Ginsburg, and N. Budaiev) are included into the final catalog. During the identification process, three independent coauthors changed the color scale stretches of the images. This helps human visual recognition to compact sources in a wide range of contrast. We have two groups of sources that will not be used in this study: (i) low-S/N sources that were visually identified by more than two observers but not chosen by `dendrogram` and (ii) candidates that were not selected by eye more than two times. We report these sources separately in Appendix F and will not use these sources in this paper.

We then crossmatched the sources in both bands when the sky coordinate offsets are smaller than the beam size at each wavelength. Among the matched sources, we found 13 common sources in the overlapping regions between the two regions, and removed those sources from the W51-E image. As a result, we identified 118 high-res sources in W51-E: 73 matched sources, 23 sources seen in only 3 mm, and 22 sources seen in only 1.3 mm. For W51-IRS2, out of 93 high-res sources, we have 23 matched sources, 59 sources only seen in 3 mm, and 11 sources only seen in 1.3 mm. The number of detections is summarized in Table 1 and their snapshots and positions are displayed in Appendix D (Figures 23–27) and Appendix E (Figures 28–38). We also summarize the detailed information including sky coordinates and the derived physical properties in Tables 2, 3, 4, and 5 in Appendix C.

3.2. Spectral Indices

The spectral index, defined as the power-law slope of the spectral energy distribution (SED) at specific wavelength intervals, is a useful tool for characterizing the observations of targets with photometry. Using the continuum fluxes at 3 mm and 1.3 mm, we derive the spectral index as

$$\alpha \equiv \log(F_{3\ \mathrm{mm}}/F_{1.3\ \mathrm{mm}})/\log(\nu_{3\ \mathrm{mm}}/\nu_{1.3\ \mathrm{mm}}), \quad (1)$$

where $F_{3\ \mathrm{mm}}$ and $F_{1.3\ \mathrm{mm}}$ are the flux density at 3 mm and 1.3 mm, respectively, and $\nu_{3\ \mathrm{mm}}$ and $\nu_{1.3\ \mathrm{mm}}$ are the central band frequencies, which are the intraband flux-weighted average frequencies assuming the power-law slope (i.e., $F_\nu \propto \nu^\alpha$). For example, the central frequency at 1.3 mm is calculated as

$$\nu_{1.3\ \mathrm{mm}} = \int_{1.3\ \mathrm{mm}} \nu^{\alpha+1} d\nu \Big/ \int_{1.3\ \mathrm{mm}} \nu^{\alpha} d\nu. \quad (2)$$

When we assume a power-law slope $\alpha = 2$, we obtain central frequencies of 92.98 GHz and 226.69 GHz at 1.3 mm and 3 mm, respectively.

[28] `astrodendro` https://dendrograms.readthedocs.io/en/stable/ and `dendrocat` https://dendrocat.readthedocs.io/en/latest/ Python packages.

Table 1
The Number of High-resolution Sources Detected in W51-E and W51-IRS2

	W51-E	W51-IRS2
Crossmatched (a + b + c)	73	23
(a) dust dominated	59	13
(b) optically thick dust or free–free contaminated	10	6
(c) free–free contaminated	4	4
Single detection (d + e)	45	70
(d) 1.3 mm	22	11
(e) 3 mm	23	59
Total (a + b + c + d + e)	118	93

The spectral index can be used to classify our samples to first order. When dust emission is optically thick, the SED follows the Rayleigh–Jeans law, $S_\nu \propto \nu^2$, leading to a spectral index $\alpha \sim 2$ at millimeter wavelengths. On the other hand, when the dust emission is completely optically thin, the dust power-law index ($\propto \nu^\beta$; $\beta \sim 1.75$ for a typical ISM; V. Ossenkopf & T. Henning 1994) modifies the blackbody radiation to the spectral slope $\alpha \sim 3.7$. Recently, N. Budaiev et al. (2024) suggested a model in which an optically thick part plus an optically thin envelope explains the spectral slope $3.7 > \alpha \gtrsim 2$ measured for cores between ALMA 3 mm and 1.3 mm observations. When $T_{\rm dust} \sim 50$ K is assumed, the spectral index ranges from 1.93 to 3.7 depending on the radius of an optically thick sphere and the gas surface number density. Indices $\alpha \sim 0$ are most likely to originate from optically thin H II regions since the spectrum of free–free emission is almost flat over the turnover frequency (e.g., P. Ghavamian & P. Hartigan 1998; T. L. Wilson et al. 2013).

We measured a spectral index using Equation (1) with the peak flux, which is the brightest pixel value, rather than the integrated flux. In most cases, the intensity from the brightest pixel includes information along the line of sight of the densest part of the sources. For this reason, the peak intensity of each source was chosen and converted to the peak flux density for the spectral index measurement. Given that the beam size is not identical between the two bands, we conducted convolution of the continuum images to the common beam of the two bands for fair comparison. Note that the beam of the 3 mm high-res image is always larger than that of 1.3 mm and therefore the common beam is identical to the 3 mm beam. This means that only the 1.3 mm continuum image needs to be convolved with the common beam. The convolution of the image was conducted with the `astropy` Python package and the common beam size is calculated by `radio_beam`.[29] After the convolution, the image array is multiplied by the beam area ratio of Band 3 and 1.3 mm to conserve the peak flux values of the unresolved sources.

The left panel of Figure 3 displays the peak fluxes extracted from the 3 mm and convolved 1.3 mm continuum images. We used 73 and 23 crossmatched sources in W51-E and W51-IRS2, respectively, for this analysis. The flux errors are estimated from the background noise estimated over the area without any compact sources in each continuum image. The upper right and lower right panels of Figure 3 show the distributions of the spectral indices of the fragments. Using the spectral indices, we categorize our samples into three groups. The first is dust-dominated sources with a spectral index greater than two, considered to be dusty sources with $T \gtrsim 20$ K without free–free emission. Optically thick H II regions also can have $\alpha \sim 2$ (E. Keto et al. 2008), and we will discuss this possibility in a later part of this section. However, a spectral index $\alpha < 2$ can be produced even when the dust emission is optically thick. This occurs when free–free emission is mixed with dust emission, or optically thick dust emission has a temperature gradient along the line of sight (e.g., J. I.-H. Li et al. 2017; R. Galván-Madrid et al. 2018). In particular, R. Galván-Madrid et al. (2018) showed that the submillimeter spectral index at the Rayleigh–Jeans tail can be as low as 1.5 without changing the dust opacity power-law exponent from the YSO models. Motivated by these studies, we created a second category with a spectral index $1.5 < \alpha < 2$, where the source can be optically thick or free–free contamination possibly exists. The third group consists of sources with spectral indices lower than 1.5, indicating significant contamination from free–free emission. We summarize the number of each group in Table 1. We remind the reader that the spectral index measurements were carried out for the crossmatched samples only.

In both regions, more than half of the crossmatched samples (69 out of 73 in W51-E and 19 out of 23 in W51-IRS2) are either dust-dominated sources or possible free–free-contaminated sources while fewer sources are free–free-contaminated sources, indicating that we observe predominantly dusty sources. When the flux measurement uncertainties are expanded to include the absolute calibration errors—assumed to be 10% at 1.3 mm and 5% at 3 mm—the number of dust-dominated sources could vary between 54 and 62 in W51-E and between 10 and 15 in W51-IRS2. Similarly, the number of sources in the second group could range from 7 to 15 in W51-E and from 4 to 10 in W51-IRS2. The peak of the spectral index distribution around $\alpha \sim 2$ in our samples indicates that most of our sources have optically thick centers and are surrounded by optically thin dust parts as suggested in the study of the Sgr B2 cloud by N. Budaiev et al. (2024).

On the other hand, we have only a few (four in each region) matched sources in the free–free-contaminated group in each region. The number of free–free-contaminated sources does not change even though we consider the calibration errors via error propagation: no change in W51-E and possibly $N = 4$ to $N = 3$ in W51-IRS2. Some of the sources are already known H II regions, including d2 (#4; e.g., A. Ginsburg et al. 2016) in W51-IRS2. A recent Very Large Array observation of W51-IRS2 revealed two HCH II regions with sizes of 33 au and 170 au (D. Deal et al. 2025, in preparation), and they are also classified as free–free-contaminated sources in our catalog ($\alpha = 1.44$ and 0.22). Note that, we do not have any sources with $\alpha \lesssim -2$, which would indicate gyrosynchrotron emission from a magnetic field.

The second group includes 10 and 6 sources in W51-E and W51-IRS2, respectively. The three massive YSOs, W51e2e (#39 in W51-E), W51e8 (#32 in W51-E), and W51-North (#11 in W51-IRS2) studied in C. Goddi et al. (2020), are all include in this group. They all exhibit no sign of free–free emission at longer wavelengths (A. Ginsburg et al. 2016). Therefore, these objects may be so optically thick at 1.3 mm that the index is inverted because of the temperature structure, i.e., the optically thick layer is colder at 1.3 mm than at 3 mm (R. Galván-Madrid et al. 2018).

[29] https://radio-beam.readthedocs.io/en/latest/

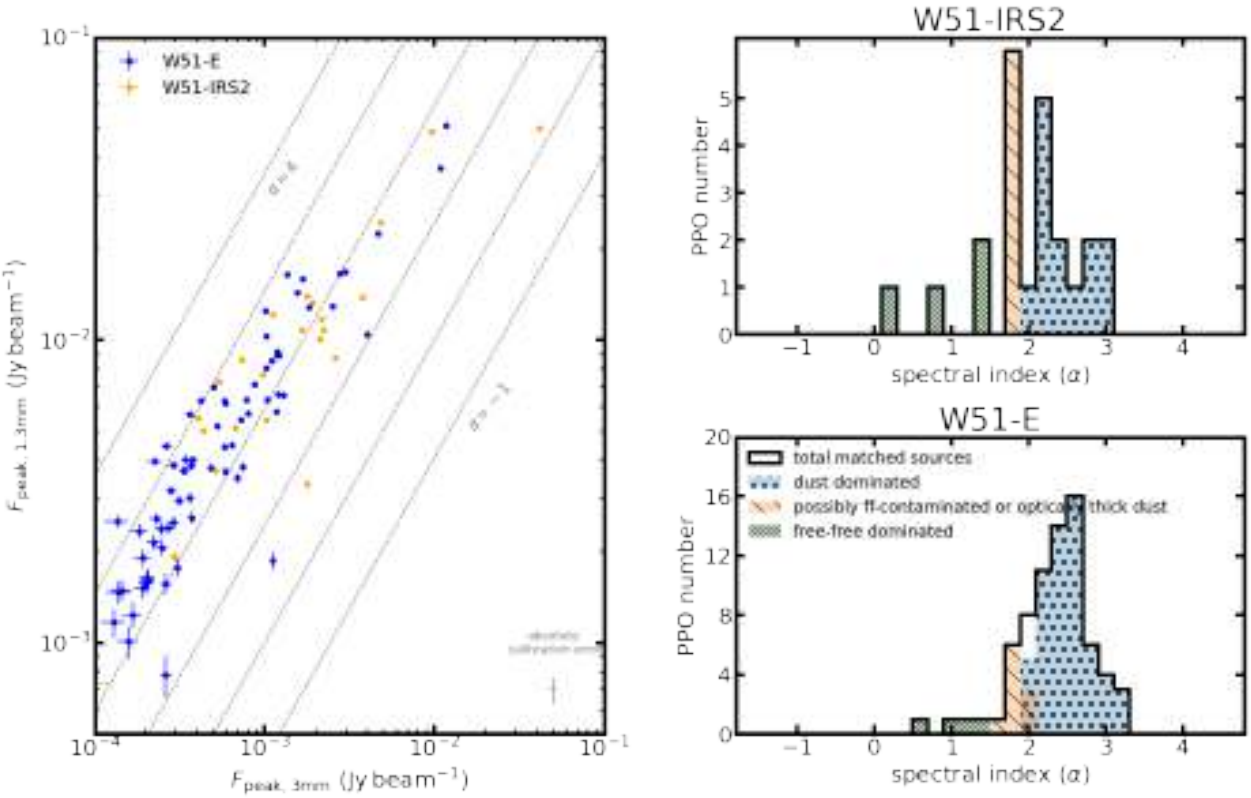

Figure 3. The spectral index distribution of high-res sources detected in both bands. Left: 3 mm peak flux vs. 1.3 mm peak flux diagram. Here, the 1.3 mm peak fluxes are measured from the convolved continuum images with the common beam. The error bars denote the background noise level measured in each continuum image. Typical calibration errors, 5% in Band 3 and 10% in Band 6, are marked as gray crosses at the lower right corner. The gray dashed lines indicate a spectral index = [−1, 0, 1, 2, 3, 4] from bottom to top. Right column: histograms of the spectral indices in W51-E and W51-IRS2. High-res sources in each region are grouped depending on whether the spectral index indicates a certain dusty source or certain H II regions, or possibly free–free emission contamination.

Finally, we discuss the possibility of optically thick H II regions. Optically thick free–free emission follows the Rayleigh–Jeans law as explained in Equation (7) of E. Keto et al. (2008):

$$S_\nu \approx 2kT_e(\nu^2/c^2). \quad (3)$$

In this case, the optically thick H II regions can produce a spectral index $\alpha = 2$. Given a large fraction of unresolved high-res sources (∼60%–80%; Section 3.3), it is possible to have a brightness temperature T_B such that $T_B\eta = T_e$, where $\eta < 1$ is the beam-filling factor. Assuming an upper limit radius of possible unresolved HCH II region of $R \sim 100$ au and a Lyman continuum luminosity of OB stars of $L_{\rm LyC} \gtrsim 5 \times 10^{47}$ s^{-1}, we obtain an electron density $n_e \gtrsim 10^7$ cm^{-3} inside the Strömgen radius. At such high density, the confined HCH II regions are mostly likely to be surrounded by dust; we should still observe dust emission rather than free–free emission even though high-res sources with $\alpha \sim 2$ are HCH II regions.

3.3. Sizes

For the sizes of our sources, we utilize the definition of a recent ALMA survey of protoplanetary disks (M. Ansdell et al. 2018) that the radius includes 95% of the total flux. When it is adopted in a Gaussian model, the disk radius is equivalent to $1/(\sqrt{2\ln(2)}) \times$ FWHM of the Gaussian model (J. J. Tobin et al. 2020). We use the FWHM of the major axis of the Gaussian model produced by our fitting method, `TGIF` (Appendix A). To estimate the physical sizes, we deconvolve the image beam ellipse from the FWHM ellipse of our 2D Gaussian model. We regarded failure of the deconvolution due to the observed size being smaller than the beam as indicative of the object being unresolved.

Figure 4 shows the cumulative distribution of radii measured from the 1.3 mm and 3 mm high-res images. We perform a survival analysis with the Kaplan–Meier estimator implemented in the Python package `lifelines` (C. Davidson-Pilon 2019). Sources that are unresolved or undetected are censored on the left side of the cumulative function. Only ∼70% and ∼20%–30% of sources in the 1.3 mm and 3 mm images, respectively, are identified as resolved. The smaller fraction of resolved sources in the 3 mm images is mainly due to the larger beam size. The resolved sources have a range of size distributions, ∼200–1000 au at 3 mm and ∼100–500 au at 1.3 mm. This tells us the upper limits of the sizes for unresolved sources: 100 and 200 au for 1.3 mm and 3 mm, respectively.

We present the aspect ratios of the high-res sources in Figure 5. The distribution of axis ratios, defined as the ratio of the deconvolved major-axis size to the deconvolved mino r-axis size, ranges from 1.0 to 2.8.

3.4. Classification of High-resolution Sources: Pre-/protostellar Objects

A large number of sources are unresolved with an upper limit of size ∼ 100–200 au, while the maximum sizes of our sources were estimated to be ∼1000 au in the previous section. Since our sources are smaller than the typical size of cores (∼0.05–0.1 pc; J. di Francesco et al. 2007; F. Motte et al. 2022), it is not

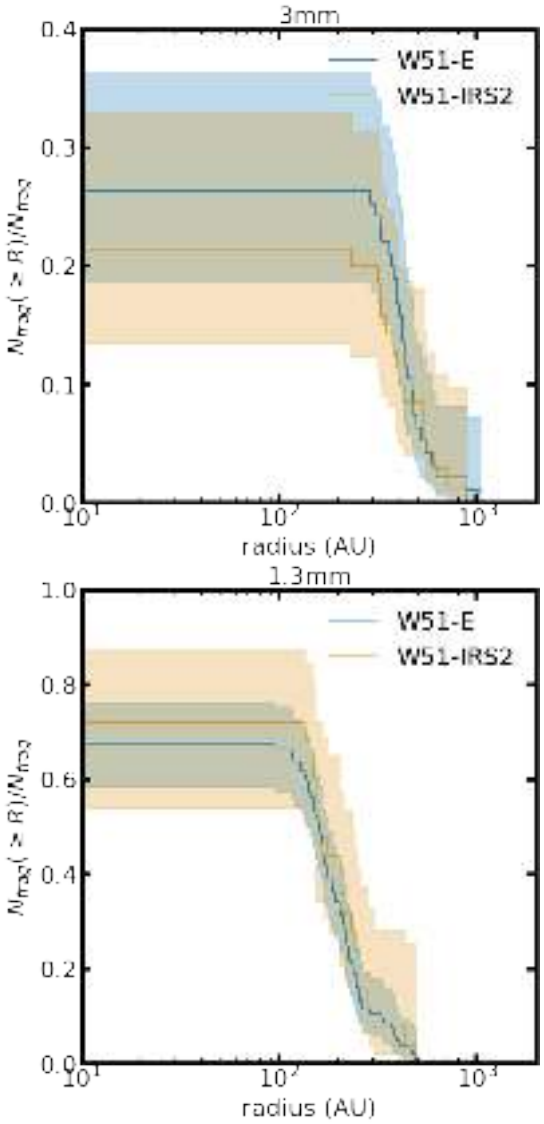

Figure 4. Cumulative distribution of the radii of the high-res sources. The cumulative function is generated by a survival analysis with the Kaplan–Meier estimator provided by the `lifelines` package. The function is censored on the left side by excluding unresolved or undetected sources in the analysis.

appropriate to call these compact objects "cores." In addition, the size range of our targets covers that of "envelopes" (∼300–3000 au) and "protostellar objects" (∼10–200 au) in R. Pokhrel et al. (2018).

From the spectral index analysis (Section 3.2), we determined that most of our sources are dusty, though a few are HCH II regions exhibiting free–free emission. Some of our sources have signs of high-mass star formation such as compact H II regions (e.g., #4 in W51-IRS2, also known as d2; Appendix E) or hot cores. In particular, we confirmed that nine hot cores in the catalog of M. Bonfand et al. (2024) are found in the field of view of both protoclusters. Some of them have a prominent molecular outflow, e.g., #39 in W51-E, also known as W51e2e (Appendix E; C. Goddi et al. 2020). However, the presence of protostars cannot be definitively confirmed for the rest of the sources.

Combining these facts together, the high-res sources are mostly dust emission from prestellar or protostellar objects smaller than ∼100–1000 au—they are probably either prestellar

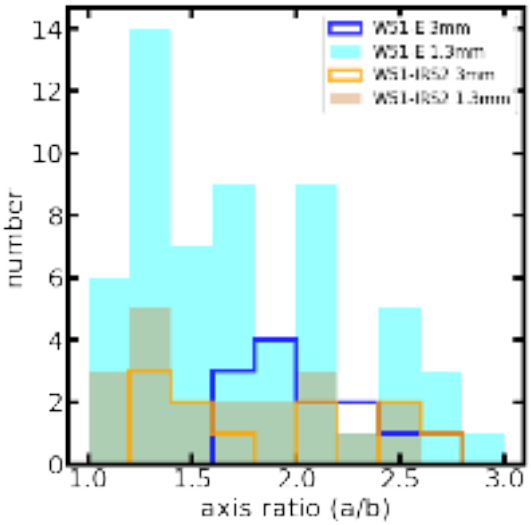

Figure 5. The axis ratio between the major and the minor axes of the high-res sources.

dust without central protostars or dust disks/envelopes around a protostar. In the latter case, the high-res sources are likely to be Stage 0/I sources with a nonnegligible envelope mass $M_{\rm env} > 0.1\,M_\odot$ (A. Crapsi et al. 2008; T. Richardson et al. 2024). We will use the term "pre-/protostellar objects" (PPOs) to refer to the high-res sources.

3.5. Temperature Constraints through a Modified Blackbody Model

We used the integrated flux rather than the peak flux to account for the flux emitted by the whole surface of each PPO. The integrated flux is measured by using Gaussian fitting, `TGIF` (T. Yoo & A. Ginsburg 2024), as illustrated in Appendix A.

Dust temperature is an essential quantity for estimating dust masses from dust emission. Due to the incomplete sampling of the dust SED in IR observations at subarcsecond resolution, it is challenging to estimate the dust temperatures of the PPOs. One approach is to adopt a simple PPO model using modified blackbody radiation (MBB). Following N. Budaiev et al. (2024), who analyzed similar-resolution data of the Sgr B2 region in the same ALMA bands, we reproduce the ALMA Band 3 and Band 6 fluxes using a PPO model consisting of an optically thick core and an optically thin envelope. The model produces MBB intensity following the equation

$$B_\nu = \frac{2h\nu^3}{c^2}\frac{1}{e^{h\nu/k_BT}-1}(1-e^{-\kappa_\nu\Sigma}), \quad (4)$$

where ν is the frequency, h is the Planck constant, c is the speed of light, k_B is the Boltzmann constant, T is the dust temperature of the optically thick part, e.g., protostars or disk, κ_ν is the dust opacity, and Σ is the column density of the optical thin part of the PPO. Here, we adopt dust opacities $\kappa_{1.3\ \rm mm} = 0.0083\ {\rm cm^2\ g^{-1}}$ and $\kappa_{3\ \rm mm} = 0.0017\ {\rm cm^2\ g^{-1}}$ from models of dust grains with thin ice mantles with an age of 10^5 yr and a gas density of $10^6\ {\rm cm^{-3}}$ (V. Ossenkopf & T. Henning 1994). We allow for Σ and T to vary across grids ranging $\Sigma = 10^{21}$–$10^{27}\ {\rm g\ cm^{-2}}$ and $T = 5$–400 K to account for various conditions of PPOs.

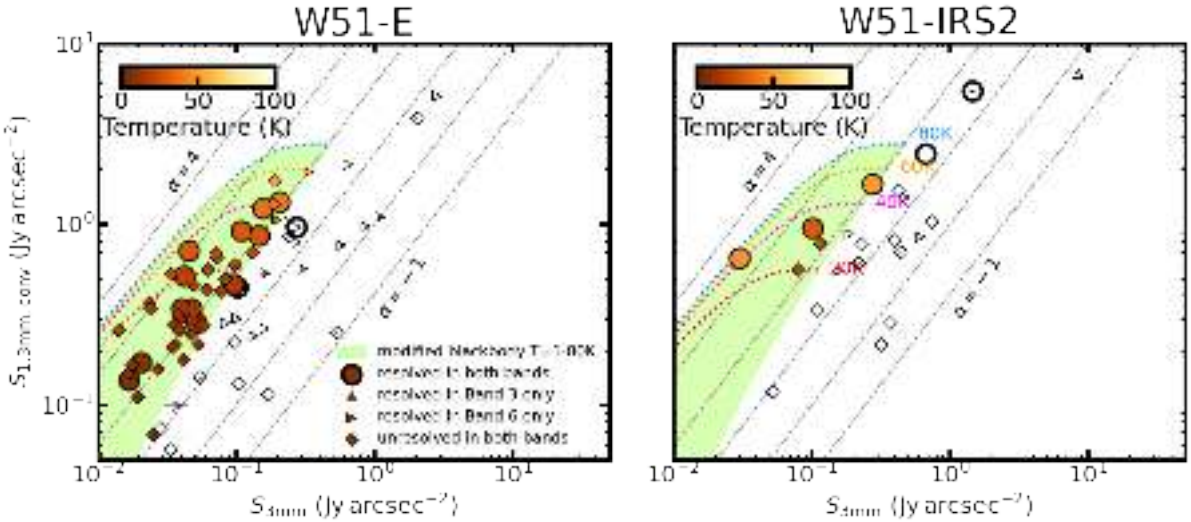

Figure 6. The surface brightnesses of the PPOs from the 1.3 mm and 3 mm observations in W51-E (left) and W51-IRS2 (middle). For 1.3 mm, the surface brightnesses are measured from the 1.3 mm images convolved to the 3 mm image beam. Models of MBB surface brightness with surface density $\Sigma = 10^{21}$–10^{27} cm^{-2} are presented as dashed curves with colors denoting MBB temperature, $T = 20$, 40, 60, and 80 K, following Equation (4). The surface brightness parameter space that MBBs with $T = 5$–400 K can occupy is shaded with green colors. We can derive the MBB temperatures of the PPOs lying within the green area, and they are color coded based on the derived MBB temperatures. The PPOs outside the green area have empty symbols. Depending on which band the PPOs are resolved, they are represented as different shapes: circles (resolved in both 1.3 mm and 3 mm), triangles pointing up (resolved only in 3 mm) and pointing right (resolved only in 1.3 mm), and diamonds (unresolved in both bands). Since the upper limits of the size are imposed uniformly for unresolved sources, the derived temperatures are lower limits. The dashed diagonal lines are spectral index $\alpha = -1$, 0, 1, 2, 3, and 4 measured from the integrated fluxes. The brightness temperature corresponding to a surface brightness of 1 Jy arcsec^{-2} is 27 K at 1.3 mm and 153 K at 3 mm.

Figure 6 shows the dust temperatures estimated from the MBB surface brightnesses. We converted the observed flux densities into surface brightnesses in order to match those with the predicted MBB surface brightnesses regardless of their size. Here, the 1.3 mm surface brightnesses are estimated from the 1.3 mm images convolved to the common beam, that is, the 3 mm image beam, to take into account the different angular resolutions. For unresolved sources (Section 3.3), we assign their sizes as the minimum size of the resolved PPOs and convert their flux densities to surface brightnesses. In this case, the derived temperature should be a lower limit as the size is an upper limit. A significant number of crossmatched PPOs (26 out of 73 in W51-E and 17 out of 23 in W51-IRS2) do not have a viable temperature estimate as they lie outside of the range of surface brightnesses at both wavelengths spanned by the model. Even though the sources are resolved in both bands, there are still some sources for which the spectral index is too low to estimate the MBB temperature in Figure 6. These are the cases where the dust emission is contaminated by free–free emission or the optically thick dust emission at each band is derived from different temperature as explained in Section 3.2. We display the spectral indices measured from the integrated fluxes in Figure 6. These reflect the averaged optical depth in the whole area of the PPOs whereas the spectral index using the peak flux in Section 3.2 more accurately describes the optical depths of the central regions of the PPOs.

The inferred dust temperatures from the MBB model are distributed over 5–60 K (Figure 7). Note that these include a number of dust temperature lower limits from unresolved sources.

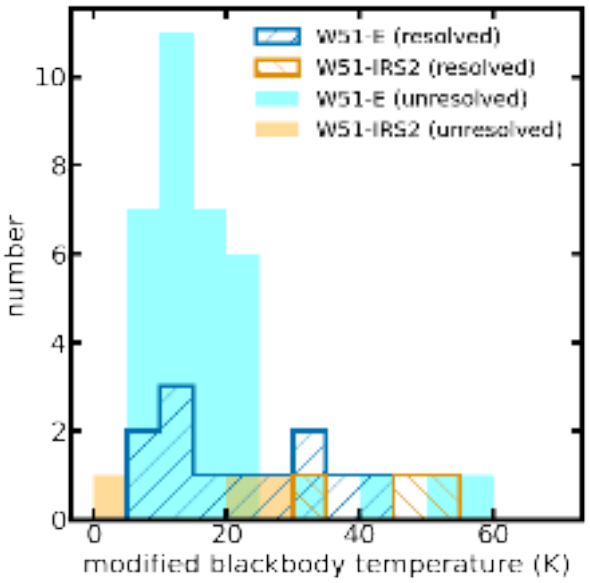

Figure 7. The dust temperatures estimated by the MBB model in Figure 6. The MBB temperatures for unresolved sources are the lower limits.

3.6. Constraints on Pre-/protostellar Object Masses

In the previous section, we found that a large portion of our sample is dominated by optically thick dust emission, so the column densities (or masses) are lower limits. Uncertainties in $T_{\rm dust}$ also affect mass estimates (e.g., T. Richardson et al. 2024).

From the dust continuum flux, the dust mass can be inferred by assuming optically thin dust emission (R. H. Hildebrand 1983):

$$M = \frac{S_\nu D^2}{\kappa_\nu B_\nu(T)}, \quad (5)$$

where S_ν is the flux density, D is the distance, κ_ν is the dust opacity, and $B_\nu(T)$ is the Planck function at a specific temperature. For optically thin sources, this is a good estimate of the total mass if we have a measurement of the temperature.

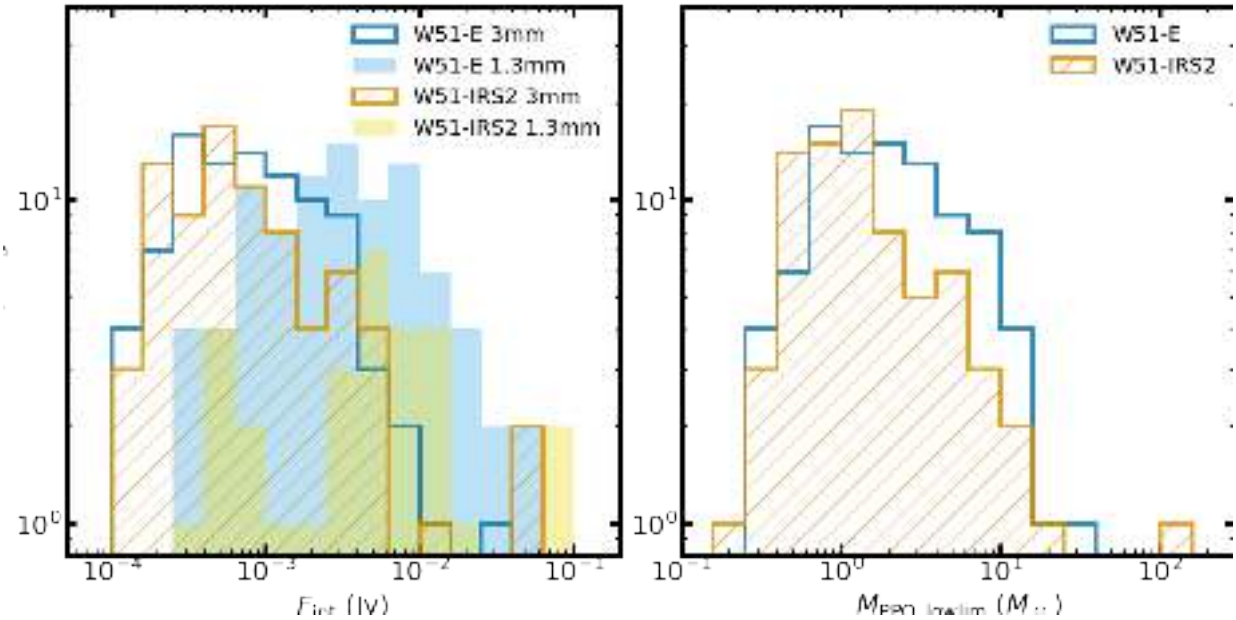

Figure 8. Left: histogram of the integrated fluxes of the PPOs excluding sources contaminated by free–free emission at 1.3 mm and 3 mm. Right: lower limits of PPO masses using the 3 mm integrated fluxes by assuming a constant dust temperature of 40 K ($M_{\rm PPO,lowlim}$).

For optically thick sources, this mass estimate is a lower limit since we do not detect light from all of the mass. We expect that most of the objects in our sample are Stage 0/I, in which a substantial dust envelope surrounds a central protostar. Under this assumption, the mass we measure is that of the dust envelope, not the star.

To constrain the PPO masses, we adopt a 40 K dust temperature. This is motivated by a recent YSO model study that demonstrated that the choice of dust temperature, $T = 40$ K, which is warmer than the commonly adopted temperature $T = 20$ K, is more accurate in inferring the true mass with the optically thin dust emission assumption (T. Richardson et al. 2024). Although the average MBB temperature in W51-E and W51-IRS2 is slightly lower than 40 K, this is a reasonable choice considering that a large fraction of the MBB temperature estimates are lower limits for unresolved PPOs. When PPOs are associated with hot cores, we assign the same temperature as the hot cores (100 K or 300 K; Section 4.2) instead of 40 K, considering their heating effects. In W51-E, four PPOs (#30, #31, #32, and #33) are associated with a 100 K hot core and two (#39 and #40) with a 300 K hot core, while in W51-IRS2, 16 PPOs (#0, #5, #7, #10, #14, #17, #20, #21, #27, #39, #46, #47, #48, #55, #56, and #74) correspond spatially to 100 K hot cores and six (#11, #13, #25, #26, #36, and #38) to a 300 K hot core.

In Figure 8, we display the integrated fluxes at 1.3 mm and 3 mm. The fluxes of the free–free-contaminated sources are excluded because the mass estimations could be significantly different from their true masses when the dust emission is contaminated by free–free emission. Figure 8 includes a larger sample than Figure 6 as Figure 8 displays even sources detected in only one band. In the middle and right panels of Figure 8, we display the lower limits of the masses with constant temperature. We use the 3 mm flux densities to derive the masses because the lower opacity at 3 mm relative to 1.3 mm allows us to obtain information from the inner part of the PPOs. The mass lower limits from the constant temperature model span ∼0.1–200 $M_\odot$.

We would like to caution readers against the interpretation that the distribution of the mass lower limits mimics the PPO mass function or the IMF. Several major uncertain factors—temperature, the central stellar mass, and the mass ratio of optically thin/thick dust in fragments—make the predictions of the total PPO mass almost opaque (e.g., P. Padoan et al. 2023). Therefore, we will not attempt to build a PPO mass function in this paper. For a more accurate mass estimation, alternative ways such as using a Keplerian disk are required in future studies.

4. Core Fragmentation

In this section, we link cores to PPOs. We will use the term "fragment" to refer to PPOs that are spatially associated to cores. We inspect how the characteristics of core fragmentation, such as the number of fragments and fragmentation efficiency, vary with core mass and temperature.

4.1. Overview of Fragmentation

We associate our identified PPOs from Section 3 with cores by noting when a PPO lies within a boundary of cores. The core boundary is defined as the core's FWHM extended slightly further by the size of the ALMA-IMF beam. The core's FWHM is provided by the ALMA-IMF core catalog (F. Louvet et al. 2024) where `getsf` was used (Section 2.1).

Figures 9 and 10 present examples of core fragmentation into PPOs in W51-E and W51-IRS2. In each image, the locations of PPOs and cores are plotted over the continuum image. In W51-E, most of the cores and PPOs are concentrated in a small region (∼0.4 × ∼0.7 pc) at the central dust structure. On the other hand, the cores and PPOs in W51-IRS2 are more widely distributed along the neighboring dust filamentary structure. Matching the positions of cores and fragments reveals that not all the cores harbor fragments inside their boundaries; some cores have single or multiple

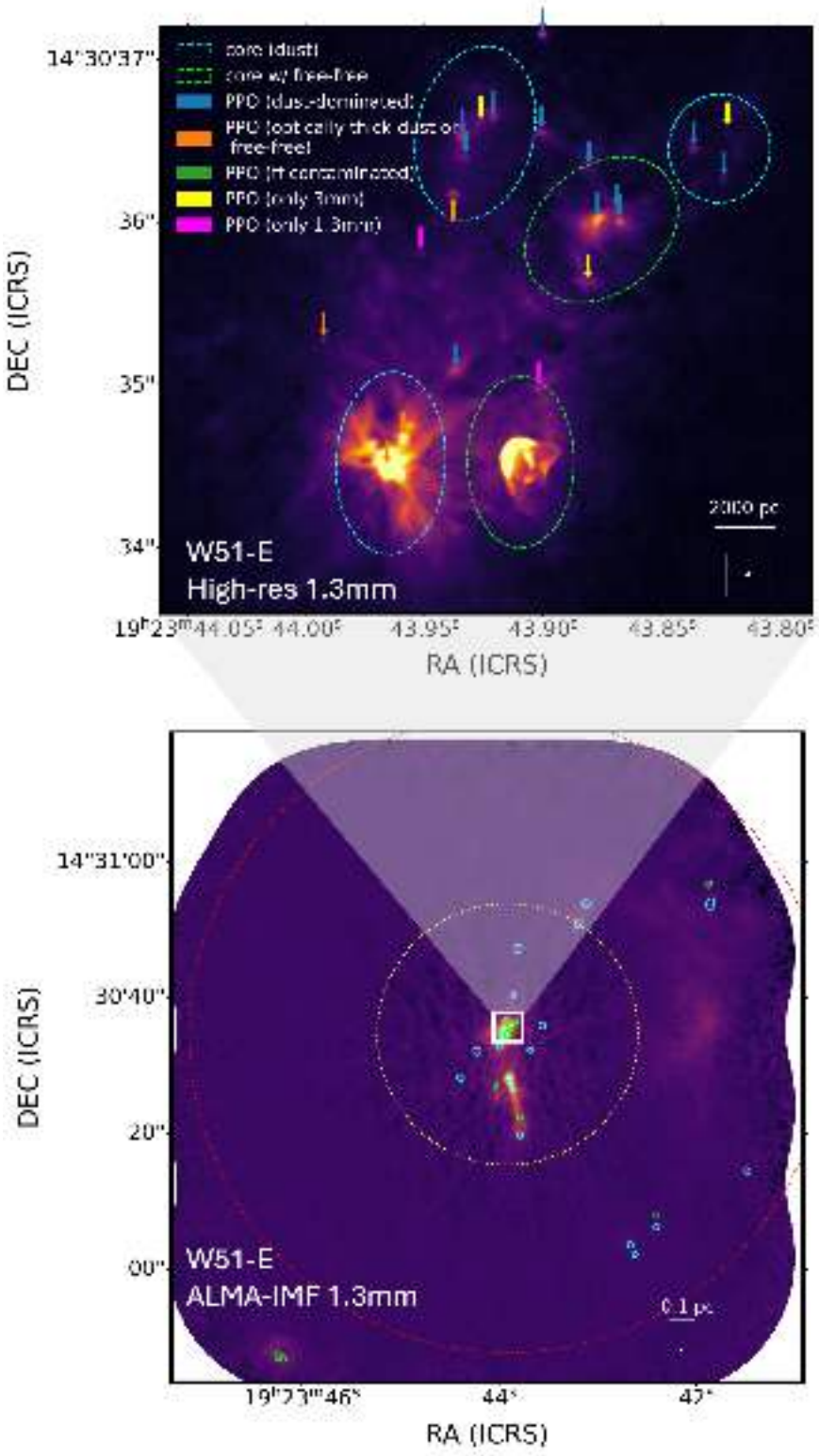

Figure 9. Examples of core fragmentation in W51-E. The cyan ellipses are dust cores and the green ellipses are cores contaminated with free–free emission. The size of the ellipse represents the boundary of the core, defined as the sum of the FWHM of the core and the FWHM of the synthesized beam. The background image of the bottom is an ALMA-IMF 1.3 mm continuum map. The field of view of the high-res image is displayed with yellow (1.3 mm) and red (3 mm) circles at the top of the ALMA-IMF map. The region enclosed by the white square at the bottom of each image is magnified with a background image of a high-res Band 6 continuum at the top. The locations of PPOs are indicated by the arrows. The PPOs detected in both bands have arrows with blue (dust dominated), orange (possibly free–free contaminated), and green (free–free contaminated) colors. The yellow and magenta arrows indicate an object identified only in 3 mm and 1.3 mm, respectively.

fragments, but others do not. In this paper, we categorize cores without fragments as unfragmented and cores containing fragments as fragmented.

The number of core fragments is displayed in Figure 11. We selected only those cores found in the same field of view as the high-res 3 mm image as it has a larger field of view than the

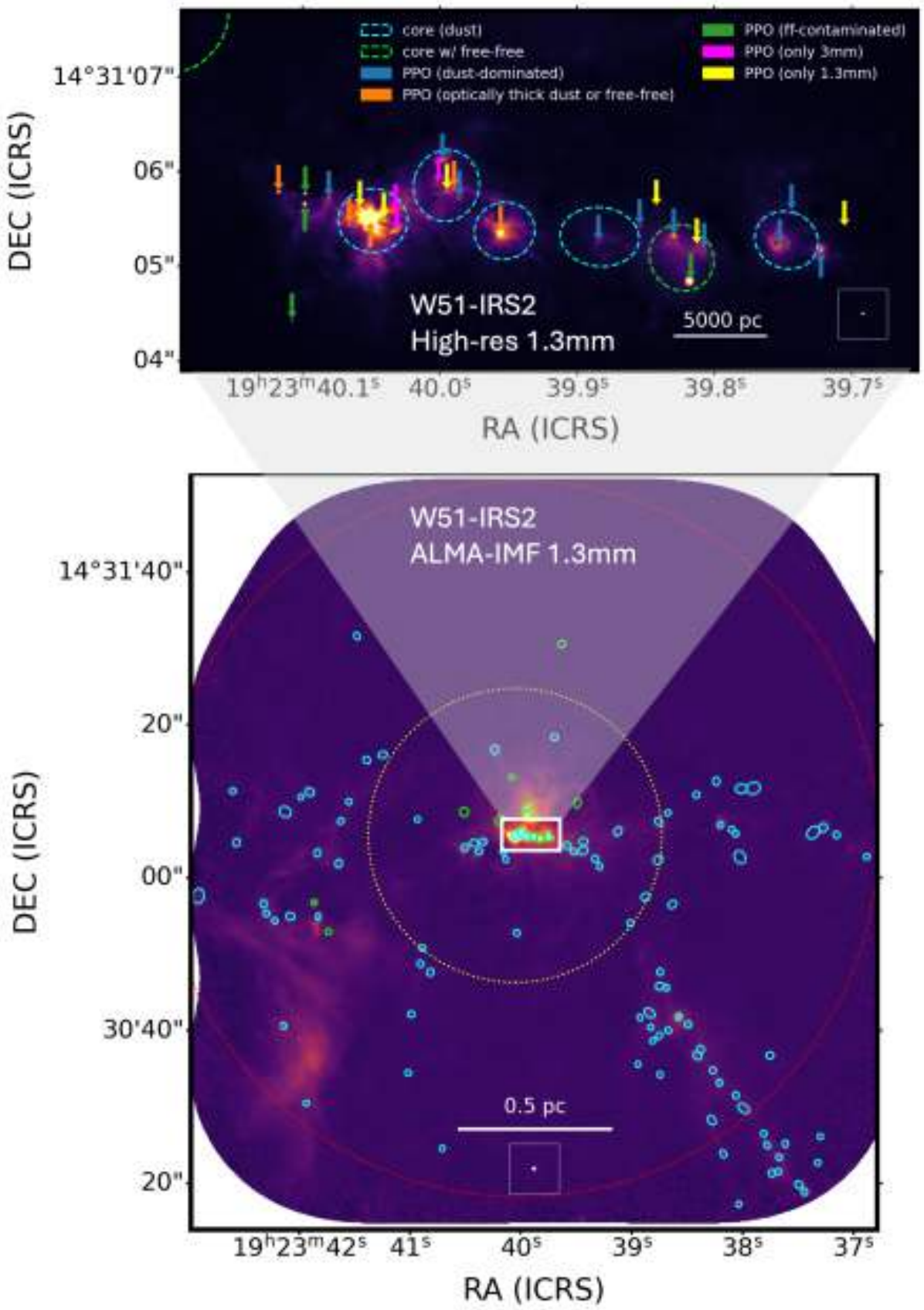

Figure 10. The same as Figure 9 for the W51-IRS2 region.

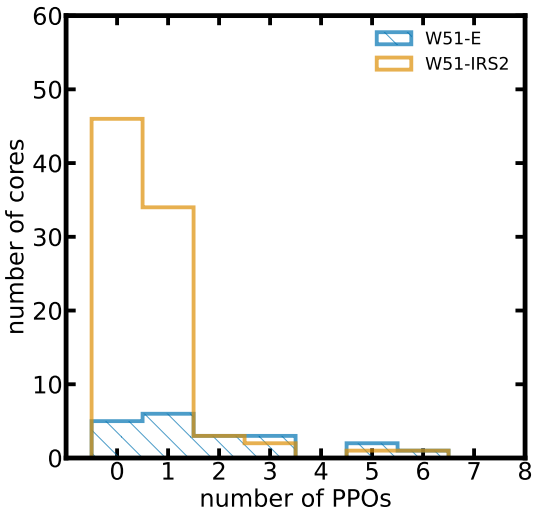

Figure 11. Histogram of the number of core fragments in W51-E (blue) and W51-IRS2 (orange). Cores without free–free emission in the same field of view of the high-res 3 mm images are used in the analysis.

1.3 mm image. This results in the selection of 20 and 87 cores in W51-E and W51-IRS2 (group A in Figure 2), respectively. In W51-E and W51-IRS2, 15/20 and 41/87 cores have fragments, respectively. In particular, W51-E has only five unfragmented cores. This is probably due to the higher completeness limit for the ALMA-IMF maps of W51-E (3.86 $M_{\odot}$) than W51-IRS2 (1.64 $M_{\odot}$; F. Louvet et al. 2024). Another possible reason will be discussed in Section 5.3.

Among the fragmented cores, the number of fragments is not uniform. Within the 15 and 41 fragmented cores in W51-E and W51-IRS2, respectively, 6 and 34 cores exhibit a single fragment, and nine and seven cores have multiple fragments, respectively. The most highly fragmented cores have six fragments in both regions.

It is worth noting that fragments of massive cores are particularly surrounded by dust structures. For example, #10 and #11 in W51-IRS2 and #32 and #39 in W51-E show similar morphology that is connected or surrounded by dust lanes (see Appendix E). They are all the most massive fragments in their parent cores. In fact, three of them (#11 in W51-IRS2, and #32 and #39 in W51-E) were suggested to have accretion flows in an earlier study (C. Goddi et al. 2020). They are probably the progenitors of high-mass stars that are actively accreting material from cores. The temperatures of the parent cores for #11 in W51-IRS2 and #39 in W51-E are assigned as 300 K (Section 4.2).

4.2. Mass Dependence of Fragmentation

How each core fragments into individual stars is one of the keys to understanding the evolution of the CMF into the IMF. In this section, we analyze the number of PPOs in each core as a function of core mass.

The core masses were computed by F. Louvet et al. (2024) who considered the optical thickness of 1.3 mm dust emission (Equation (6) of Y. Pouteau et al. 2022):

$$M = -\frac{\Omega_{1.3\ \mathrm{mm,beam}}}{\kappa_{1.3\ \mathrm{mm}}}\frac{d^2}{}\frac{S^{\mathrm{int}}_{1.3\ \mathrm{mm}}}{S^{\mathrm{peak}}_{1.3\ \mathrm{mm}}} \times \ln\left(1 - \frac{S^{\mathrm{peak}}_{1.3\ \mathrm{mm}}}{\Omega_{\mathrm{beam}} B_{1.3\ \mathrm{mm}}(T_{\mathrm{dust}})}\right), \quad (6)$$

where $\Omega_{1.3\ \mathrm{mm,beam}}$ is the solid angle of the 1.3 mm ALMA-IMF image beam, $d = 5.4$ kpc is the distance to W51, $\kappa_{1.3\ \mathrm{mm}}$ is the dust opacity at 1.3 mm, $S^{\mathrm{int}}_{1.3\ \mathrm{mm}}$ is the 1.3 mm integrated flux density, $S^{\mathrm{peak}}_{1.3\ \mathrm{mm}}$ is the 1.3 mm peak flux, and $B_{1.3\ \mathrm{mm}}(T_{\mathrm{dust}})$ is the blackbody radiation intensity at 1.3 mm. For the core temperature in W51-E and W51-IRS2, F. Louvet et al. (2024) used the Bayesian PPMAP (K. A. Marsh et al. 2015; P. Dell'Ova et al. 2024) method to infer core dust temperatures from SED fitting except for hot core candidates. For one W51-E and five W51-IRS2 cores associated with the hot core candidates found by M. Bonfand et al. (2024), where a CH_{3OCHO} map was used, a 100 K dust temperature is adopted. In addition, 300 K dust temperature is specifically assigned for cores #2 in W51-E and #1 in W51-IRS2, motivated by the molecular gas temperature models of A. Ginsburg et al. (2017) and C. Goddi et al. (2020). Note that we used the same dust opacity as the one used in the PPO mass lower limits for consistency. This results in by a factor of ~1.3 larger core masses compared with those estimated by F. Louvet et al. (2024), where the dust opacity is computed as $\kappa = 0.1(\nu/1000\ \mathrm{GHz})^{1.5}\ \mathrm{cm^2\ g^{-1}}$.

4.2.1. Cores with High Fragment Numbers Are Preferentially Massive

We find that cores with high fragment numbers are preferentially massive. Figure 12 shows the number of PPOs as a function of core fluxes and masses measured at 1.3 and 3 mm. Since the flux of a core implicitly includes the contributions from its fragments, we also present the core flux with the summed fluxes of its fragments subtracted. This residual flux indicates the emission from the core envelope, independent of the fluxes from the embedded fragments. We use core group A for the plots using 1.3 mm flux and core mass, and group C for the plots using 3 mm flux.

The number of fragments shows a positive correlation with the core fluxes at 1.3 mm and 3 mm in general. The Spearman correlation coefficients between the logarithmic flux and the number of fragments of W51-E and W51-IRS2 are 0.733 (p-value $= 2.37 \times 10^{-4}$) and 0.466 (p-value $= 5.42 \times 10^{-6}$) at 1.3 mm, and 0.669 (p-value $= 3.32 \times 10^{-3}$) and 0.312 (p-value $= 9.94 \times 10^{-3}$) at 3 mm. This relation persists even when the sum of the fragment flux is removed from the core flux. The Spearman coefficients of W51-E and W51-IRS2 are 0.663 (p-value $= 1.42 \times 10^{-3}$) and 0.483 (p-value $= 2.37 \times 10^{-6}$) at 1.3 mm, and 0.618 (p-value $= 1.41 \times 10^{-2}$) and 0.277 (p-value $= 3.86 \times 10^{-2}$) at 3 mm. Even though the residual fluxes have a weaker correlation with the number of fragments, the p-values are still low (<0.05), indicating that the trend is not the result of the interdependence of cores and fragment fluxes. At 3 mm, the core residual fluxes sometimes become negative as the sum of the PPO flux can exceed the core flux within the uncertainties, which is not physical (Section 4.3). This mainly reduces the degree of the correlation between the core residual flux and the number of fragments.

Overall, the Spearman test gives lower coefficients and p-values at the same time for W51-IRS2 than W51-E. The lower coefficient can be explained by the substantial number of unfragmented cores (58%) in W51-IRS2 compared with those in W51-E (25%), which contributes to the large scatter at the bottom along the horizontal direction. On the other hand, the lower p-values are simply attributed to the larger size of the total core sample ($N = 99$ for 1.3 mm) than that of W51-E ($N = 20$ for 1.3 mm).

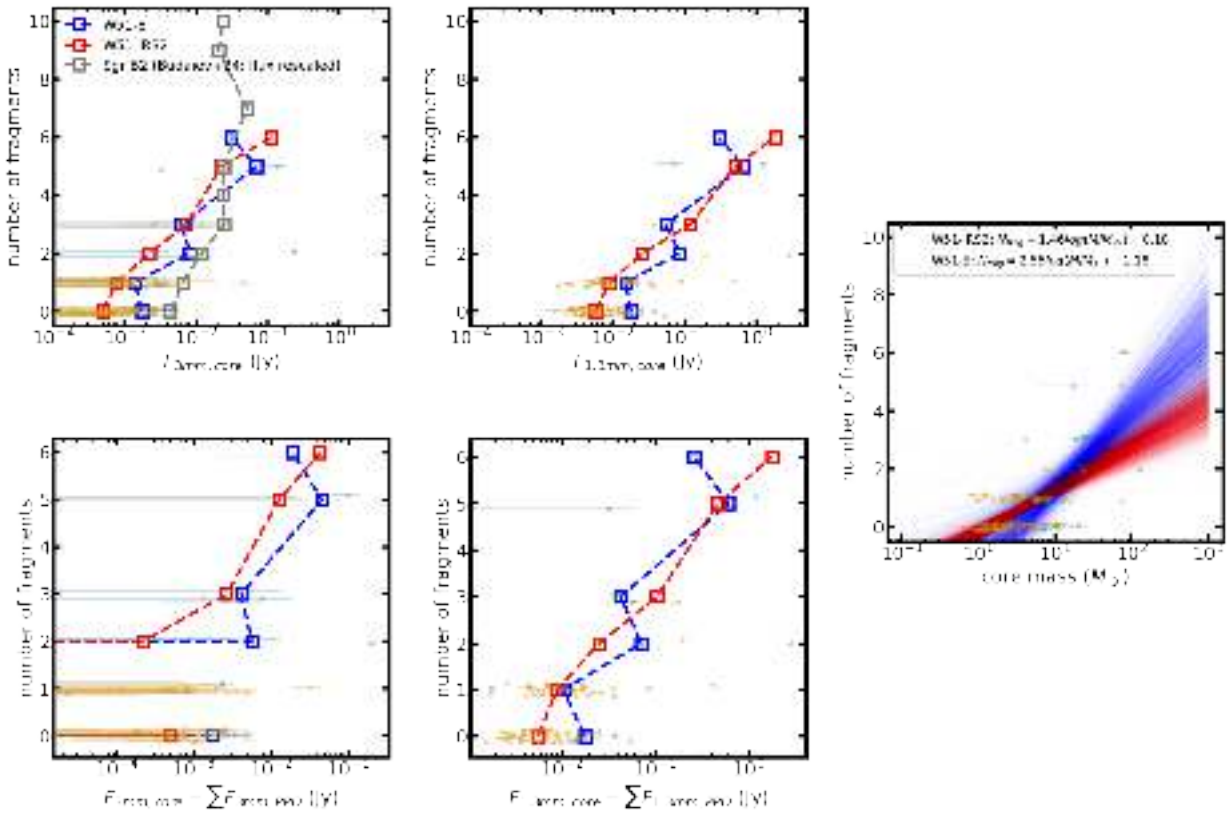

Figure 12. Number of core fragments as a function of their core fluxes (upper row), core fluxes subtracted by their fragment fluxes (lower row), and masses (right). Each cyan (W51-E) and orange (W51-IRS2) data point with error bars represents the flux or the mass of the core vs. the number of fragments. For the core fluxes, we use the integrated flux measured from the ALMA-IMF 1.3 and 3 mm continuum data. The fluxes measured from another high-mass star-forming region, Sgr B2 (N. Budaiev et al. 2024), are rescaled to the distance of W51, 5.4 kpc, and the rescaled fluxes and the number of fragments are displayed for comparison. For the number of PPOs, a small random deviation on the *y*-axis is given to differentiate each other visually. The medians of the fluxes and masses for each PPO number bin on the *y*-axis are plotted with square marks and connected with dashed lines. The horizontal dashed lines and some absence of squares in the lower left panel are due to the negative medians of core residual flux at 3 mm within the range of uncertainties. Each solid line represents 100 Markov Chain Monte Carlo (MCMC) runs of the linear fits to $\log M_{\rm core}$–$N_{\rm frag}$. The legend displays the median of the slope and the *y*-intercept of these MCMC runs.

All the cores with multiple fragments ($N_{\rm frag} \geqslant 2$) are more massive than $\sim 4\ M_\odot$. However, massive cores do not all have a high number of fragments. Instead, massive cores with $M_{\rm core} \gtrsim 10\ M_\odot$ have a wide range of the number of fragments from $N_{\rm frag} = 0$ to 6. The general trend in W51 is also observed in another high-mass star-forming region, Sgr B2 (N. Budaiev et al. 2024). This trend is therefore likely to be a common characteristic of core fragmentation in high-mass star-forming regions.

We provide a fit model of the relationship between core mass and the number of fragments. We estimated the linear fit to $\log M_{\rm core}$–$N_{\rm frag}$ by using MCMC runs. We utilized the Python package `linmix` (B. C. Kelly 2007) to run 100 MCMC runs for the W51-E and W51-IRS2 data, respectively. We obtain the medians of the slopes and intercepts, 1.46 and −0.18 for W51-IRS2, and 2.55 and −1.18 for W51-E, respectively. The shaded regions in the right panel of Figure 8 display the 1σ ranges of the slopes (1.85 to 3.16 in W51-E, and 1.23 to 1.68 in W51-IRS2) and intercepts (−0.33 to −0.02 in W51-E, and −1.98 to −0.28 in W51-IRS2) of the linear fits produced by MCMC.

4.2.2. Bright Pre-/protostellar Objects Reside in Bright Cores at 1.3 and 3 mm

We also found that the bright PPOs, or possible massive stars, preferentially form in bright (massive) cores. When we relate the fluxes of the brightest PPO in each core to the core fluxes (Figure 13), there is a clear correlation between the two quantities in both regions and at both wavelengths. This holds when the fluxes of the brightest PPOs are compared with the residual fluxes of the cores ($F_{\rm core} - {\rm sum}(F_{\rm PPO})$). In Equation (4), a large amount of flux is produced when the temperature and/or column density are high. Both conditions are usually found in massive PPOs where massive dust disks or envelopes and significant heating from massive protostars are expected. Therefore, it is reasonable to assume that the brightest PPOs are the most massive ones. This trend was also found at a larger scale, e.g., clump-to-core fragmentation (∼0.3–1 pc to ∼0.06–0.1 pc; e.g., T. Csengeri et al. 2017; Y. Lin et al. 2019; see K. Morii et al. 2023).

4.2.3. Fragments within a Given Core Have a Range of Fluxes

Another finding from the PPO fluxes is that the flux distributions between fragments are not uniform (Figure 14). The top and middle panels of Figure 14 show a wide range of flux distributions of all the fragments as a function of core flux or core residual flux. The lower panels of Figure 14 provide more details about the flux distributions by showing the flux ratios of the PPOs normalized to the flux of the brightest PPO. We only select cores with $N_{\rm frag} \geqslant 2$. The cores in both regions show a broad range of fluxes between zero and one. This result suggests that the masses of core fragments cannot be simply

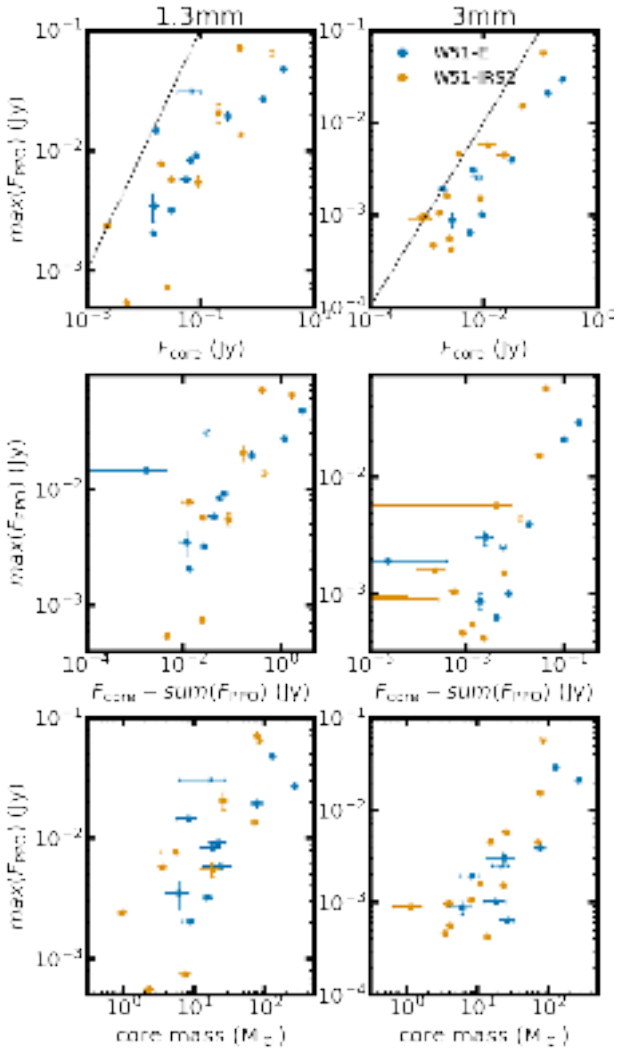

Figure 13. The fluxes of the brightest PPO associated with each core as a function of 1.3 and 3 mm core fluxes (top), core fluxes subtracted by the sum of their fragment fluxes (middle), and core masses (bottom). The error bars denote the errors of the core fluxes and those of the integrated PPO fluxes. If the integrated flux of more than one PPO is missing in the plotted band, the PPO fluxes are represented as empty circles; otherwise, they are shown as filled circles. The dashed lines in the top row indicate the one-to-one line.

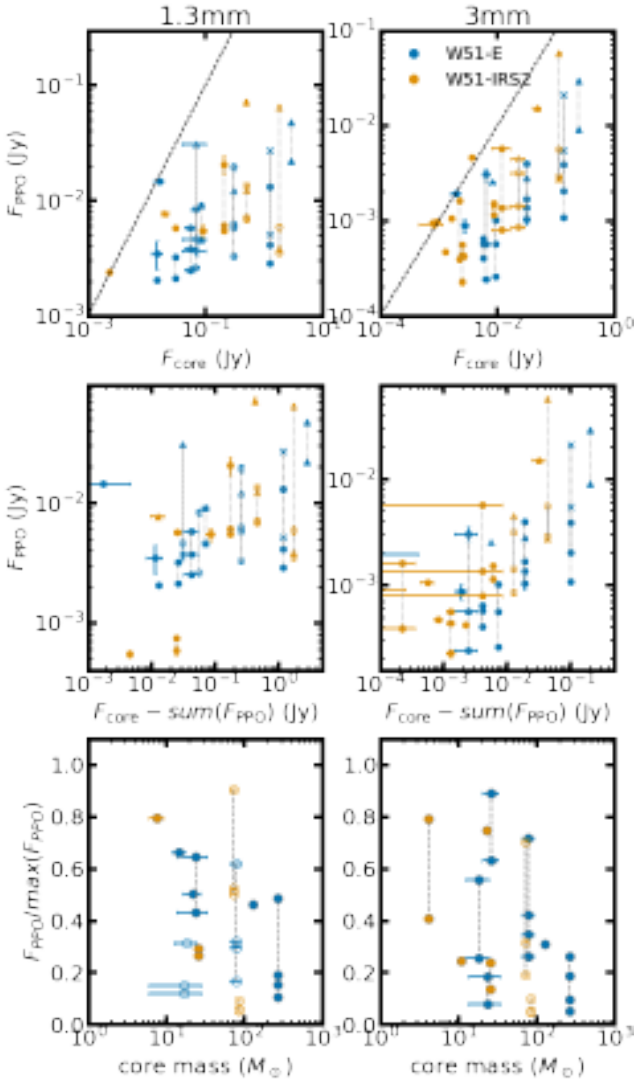

Figure 14. Top and middle: the 1.3 and 3 mm fluxes of all PPOs as a function of their parent core fluxes (top) and core envelope fluxes (middle). Bottom: the PPO flux ratios normalized to the brightest PPO flux. For clarity, the flux of the brightest PPO in each core is omitted. Only cores in which there are at least two fragments are displayed in this plot. In all panels, the fluxes of the PPOs associated with the same parent core are connected with vertical dashed lines.

predicted by a single characteristic mass, e.g., the Jeans mass. A possible explanation is the mass growth after the initial fragmentation in each fragment is different, which will be discussed in Section 5.1.2.

4.3. Fragmentation Efficiency and Thermal Suppression of Fragmentation

During core fragmentation, not all of the core mass is transferred to the fragments. The fraction of core mass contained in fragments has been usually referred to as the core formation efficiency (CFE; e.g., S. Bontemps et al. 2010; F. Louvet et al. 2014; A. Palau et al. 2015; D. J. Díaz-González et al. 2023). By analogy, but using flux instead of mass, we define the fragmentation efficiency ($\epsilon_{\rm frag}$) by comparing the flux of fragments and the parent core.

We compare the sum of PPO fluxes (sum($F_{\rm PPO}$)) within a core with the flux of the parent core ($F_{\rm core}$) in the upper panels of Figure 15. The ratio between the two quantities indicates the fragmentation efficiency as denoted by the dashed lines. A few sources have $\epsilon_{\rm frag} > 1$, which is unphysical, and it is mainly a result of the measurement errors. In the lower panels of Figure 15, we compare $\epsilon_{\rm frag}$ with the core masses. The data points are absent in the right upper (high $\epsilon_{\rm frag}$, high core mass) and lower left (low $\epsilon_{\rm frag}$, low core mass) corners. The absence in the lower left corner can be attributed to either the detection limits in our images or the intrinsic anticorrelation between core mass and $\epsilon_{\rm frag}$. On the other hand, the upper right corner cannot be explained by observational effects, suggesting that massive cores may have a low fragmentation efficiency.

We find a suggestive trend that the cores hosting faint PPOs are more likely to exhibit a high fragmentation efficiency, although the sample is not statistically large enough. In Figure 16, $\epsilon_{\rm frag}$ (left panel) and $N_{\rm frag}$ (middle panel) as a function of the brightest PPO flux at 3 mm are shown. The color of each data point represents the core temperature. Overall, cores forming brighter PPOs have higher temperatures, suggesting that a

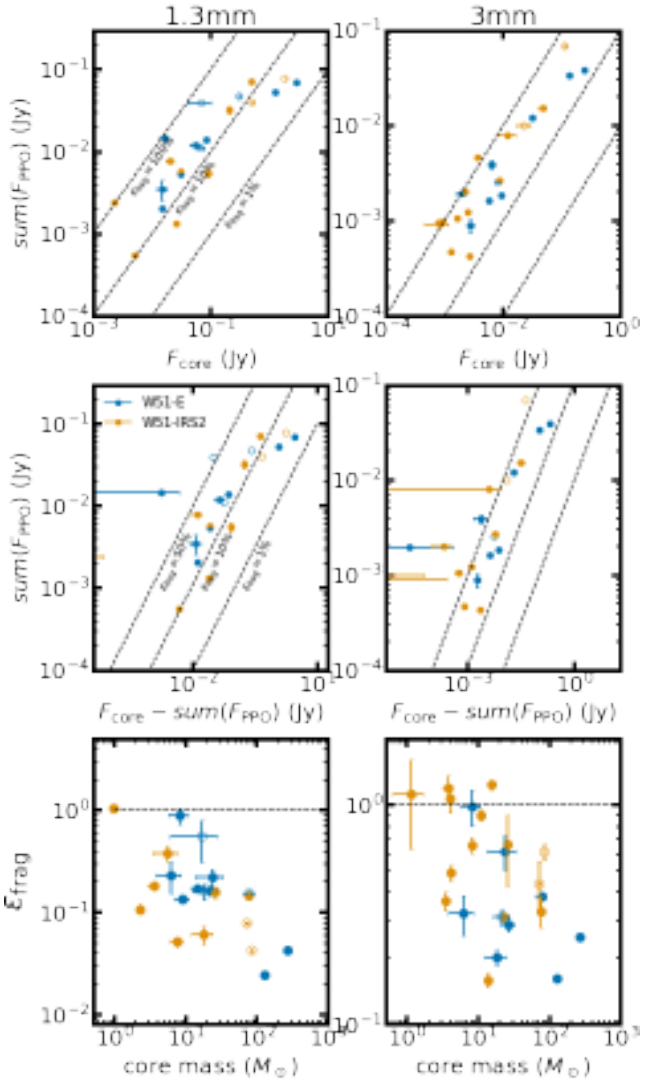

Figure 15. Top and middle: the sum of fragment fluxes as a function of core fluxes (top) and core envelope fluxes (middle) at 1.3 mm and 3 mm. If the integrated flux of more than one PPO is missing in the plotted band, the PPO fluxes are represented as empty circles; otherwise, they are shown as filled circles. The diagonal dashed lines mark the fragmentation efficiency $\epsilon_{\rm frag} = 1$, 0.1, and 0.01 in the top row and $\epsilon_{\rm frag} = 0.5$, 0.1, and 0.01 in the middle row. Bottom: fragmentation efficiencies ($\epsilon_{\rm frag}$) as a function of core masses. The fragmentation efficiency is defined as the ratio between the sum of all the PPO fluxes and core fluxes in each band. The horizontal dashed line marks $\epsilon_{\rm frag} = 1$. Some cores with $\epsilon > 1$ are not physically plausible and are instead attributed to measurement uncertainties.

massive protostar might be the main heating source. In qparticular, there are four cores hosting bright PPO, with $\max(F_{\rm PPO,3\ mm}) \gtrsim 10^{-2}$ Jy, which have a fragmentation efficiency limited to $\epsilon_{\rm frag} \lesssim 0.7$, while cores with faint PPOs span a broader range. Furthermore, these four cores showing possible signatures of strong thermal feedback are all massive ($\sim$100–300 $M_\odot$) and associated with hot core candidates identified by M. Bonfand et al. (2024). The broad range of $\epsilon_{\rm frag}$ for other cores is probably because some of these cores still have ongoing mass accretion from the core gas reservoir without feedback from a massive protostar. However, we cannot rule out that this trend is due to the small number of samples ($N = 4$) hosting the brightest PPOs with $\max(F_{\rm PPO,3\ mm}) \gtrsim 10^{-2}$ Jy. To test if the trend is statistically meaningful, we conduct a Fisher's exact test with a 2×2 contingency table of four core groups based on a fragmentation efficiency threshold of $\epsilon_{\rm frag} > 0.7$ and the flux of the brightest PPO is $\max(F_{\rm PPO,3\ mm}) \gtrsim 10^{-2}$ Jy. The test for a possible trend that cores hosting bright PPOs exhibit a lower fragmentation efficiency yields a p-value of 1.0, indicating no statistical significance. Conversely, the inverse test—whether cores with less bright PPOs have a higher fragmentation efficiency—gives a p-value of 0.27, suggesting that the observed trend can be made from random sampling with a 27% chance. Therefore, more samples are required to examine our hypothesis.

The number of fragments ($N_{\rm frag}$) does not have a clear correlation with $\max(F_{\rm PPO})$. Rather, $N_{\rm frag}$ is more closely correlated with the core masses as in Figure 12. This may simply reflect the fact that protostellar heating is not strong enough to regulate fragmentation in the whole core.

Lastly, we inspect the impact of the suppression of fragmentation on the growth of massive stars. In the right panel of Figure 16, we compare the 3 mm fluxes of the brightest PPOs and the second brightest PPOs. We found that there is a more drastic difference in fluxes between the brightest PPOs and the second brightest PPOs when a core hosts a massive protostar. In particular, the cores with $\max(F_{\rm PPO,3\ mm}) \gtrsim 10^{-2}$ Jy show a high mass ratio between the most massive and the second massive fragment ($\rm second(F_{PPO,3\ mm})/max(F_{PPO,3\ mm}) \lesssim 0.4$). This can be interpreted as the process by which massive protostars grow: radiative feedback from massive protostars effectively regulates the accretion flow from fragmentation (M. R. Krumholz et al. 2007) and hinders the growth of other neighboring protostars. This idea was previously suggested as "enforced isolation" by A. Ginsburg et al. (2017) where massive stars grow in isolation without fragmentation in the vicinity. However, again, the number of samples is too small ($N = 3$) to rule out the null hypothesis.

5. Discussion

In this section, we compare the number of fragments predicted from the Jeans masses with the observed number of fragments to assess the impact of thermal pressure in supporting cores. We also classify our core catalog into unfragmented and fragmented sources and compare the physical properties of these populations (Section 5.2). Finally, we attempt to characterize the PPOs found outside of core boundaries.

5.1. Jeans Analysis

The number of potential fragments can be simply predicted by assuming thermal/nonthermal Jeans fragmentation of the cores. For instance, R. Pokhrel et al. (2018) utilized the Jeans number defined as the object mass divided by the Jeans mass ($N_J \equiv M_{\rm core}/M_J$) to infer the expected number of fragments. We also measure the Jeans efficiency, representing the ratio of actual fragments to the Jeans number ($\epsilon_J \equiv N_{\rm frag}/N_J$). This ratio therefore tells us how effectively thermal fragmentation, if present, operates on each core.

Following the description in R. Pokhrel et al. (2018), we measured the Jeans masses of cores the using the equation (J. Binney & S. Tremaine 1987)

$$M_J = \frac{\pi^{5/2}}{6G^{3/2}} c_s^3 \rho^{-1/2}, \quad (7)$$

where G is the gravitational constant, ρ is the density, and c_s is the sound speed. The density of the core is derived from the

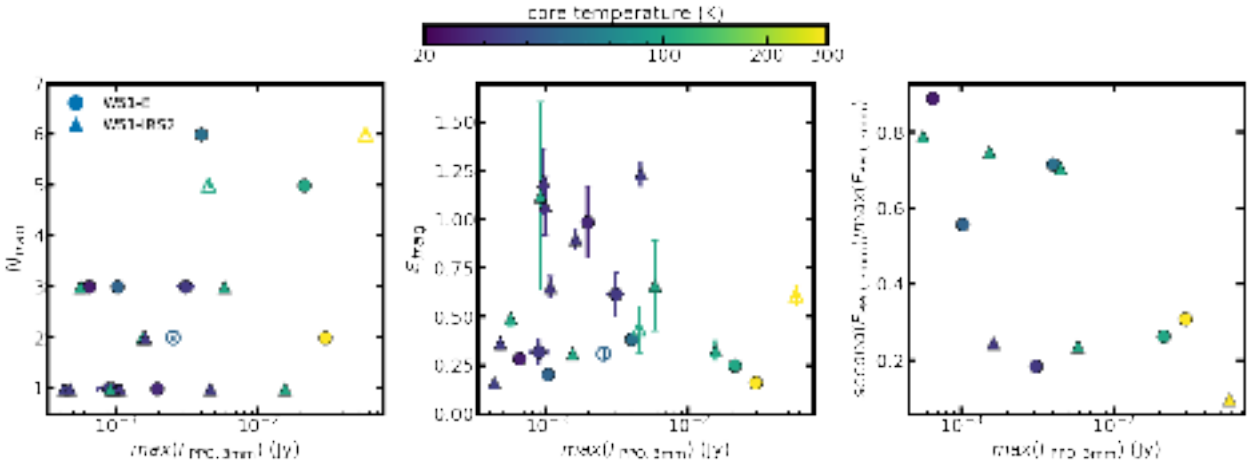

Figure 16. The fragmentation efficiency ($\epsilon_{\rm frag}$; left), the number of fragments ($N_{\rm frag}$; middle), and the ratio between the brightest and the second brightest PPOs (second($F_{\rm PPO}$)/max($F_{\rm PPO}$); right) as a function of the brightest PPO flux (max($F_{\rm PPO}$)) at 3 mm in W51-E and W51-IRS2. The color of each data point denotes core temperature. The filled and empty circles denote the complete and incomplete samples, respectively, the as same as Figure 14.

FWHM size of cores estimated by `getsf` and the mass estimated by Equation (6). The sound speed is computed based on the PPMAP temperatures of the cores. We note that only thermal pressure is considered in the analysis. Thermal Jeans masses of the cores measured from Equation (7) have a range of ∼0.2–6 $M_\odot$ (Figure 17). Interestingly, the Jeans masses of the cores in W51-IRS2 (on average 1.03 $M_\odot$) are systematically higher than those in W51-E (on average 0.69 $M_\odot$) because of their relatively low density ($\rho_{\rm avg} = 2.9 \times 10^{-17}$ g cm^{-3}) compared with those in W51-E ($\rho_{\rm avg} = 1.0 \times 10^{-17}$ g cm^{-3}).

Based on the Jeans masses, the Jeans number and the number of fragments in W51-E and W51-IRS2 are estimated and shown in the upper right panel of Figure 17. Note that, in the log-scale plot, unfragmented cores (with $N_{\rm frag} = 0$) are not displayed. Most of the Jeans numbers are below unity, meaning that fewer fragments are observed than what is expected from the thermal Jeans masses.

The lower left panel of Figure 17 shows the Jeans efficiencies of both regions. The average Jeans efficiency is estimated to be 0.05 and 0.20 in W51-E and W51-IRS2, respectively, which are far below unity. The Jeans efficiency tends to be lower in high-mass cores (lower right panel of Figure 17). This explains the relatively lower ϵ_J in W51-E compared with W51-IRS2 since the average mass of cores used in this analysis is higher in W51-E (34 $M_\odot$) than in W51-IRS2 (7 $M_\odot$).

In fact, a substantial amount of fragments are more massive than the thermal Jeans mass (Figure 18). We derived the (lower limits of) PPO mass based on the constant temperature $T = 40$ K in Section 3.6. A majority of fragment masses are up to ∼20 times higher than the Jeans masses of their parent cores, indicating again that the thermal Jeans masses are not sufficient to explain the masses of the core fragments.

5.1.1. Comparison with Other Studies

Since we followed the Jeans analysis in R. Pokhrel et al. (2018), we can directly compare our results with the Perseus region (Figure 17). We compare core-to-PPO fragmentation in W51 with the two different spatial scales of fragmentation, core-to-envelope and envelope-to-protostellar object fragmentation in R. Pokhrel et al. (2018). The spatial scales of the cores and PPOs in this study are ∼2000–6000 au and $\lesssim$100–500 au (Section 3.3), respectively. On the other hand, the core samples in R. Pokhrel et al. (2018) have sizes of 0.05–0.1 pc, which is a factor of 2 larger than our core samples. The envelopes and protostellar objects have ∼300–3000 au and 10–200 au, respectively, and thus our PPOs are in between these two scales.

The average Jeans efficiencies in the Perseus cores and envelopes were reported as 40% and 50%, respectively, which are larger than the average Jeans efficiencies in W51-E (5%) and W51-IRS2 (20%). R. Pokhrel et al. (2018) discussed that there might be a mass dependency in the Jeans efficiency; this trend is confirmed in the lower right panel of Figure 17 where Perseus and the two W51 protoclusters both display massive cores with low Jeans efficiency.

Prior to this study, a Jeans analysis of W51-IRS2 at the core-to-PPO scale was carried out by M. Tang et al. (2022) where the same long-baseline ALMA visibility data of W51-IRS2 were used but short-baseline data were not included. In M. Tang et al. (2022), the "small-scale ensembles" were defined as a group of fragments at a scale of ∼4000 au, which is almost the same with the size of cores in this study. For each small-scale ensemble, the Jeans numbers were not high enough to explain the observed number of fragments, but they reached a different conclusion that thermal fragmentation is dominant in W51-IRS2 by assuming a CFE of 24% from the equation $N_J = M_{\rm core}{\rm CFE}/M_J$. In other words, thermal pressure would explain the observed number of fragments if 76% of the core ("small-scale ensemble" in their study) mass is not fragmenting. However, a uniform CFE is not applicable to our data given the broad range of fragmentation efficiencies (Figure 15).

Moreover, different fragment identification schemes result in different numbers of fragments. M. Tang et al. (2022) used the 12σ contour where $\sigma = 0.11$ mJy beam^{-1} and the peaks were verified by `dendrogram` with parameters of `min_value` = 1.32 mJy beam^{-1} and `min_delta` = 0.011 mJy beam^{-1}. Notably, `min_delta` is much lower than the value adopted in this study, $1.5\sigma \sim 0.1$ mJy beam^{-1}, resulting in a higher number of fragments identified in their analysis. For the #11 PPO in W51-IRS2, also known as W51-North (SE1 in M. Tang et al. 2022), 20 fragments were identified in M. Tang et al. (2022), whereas six PPOs are found in this study. In particular, there is a

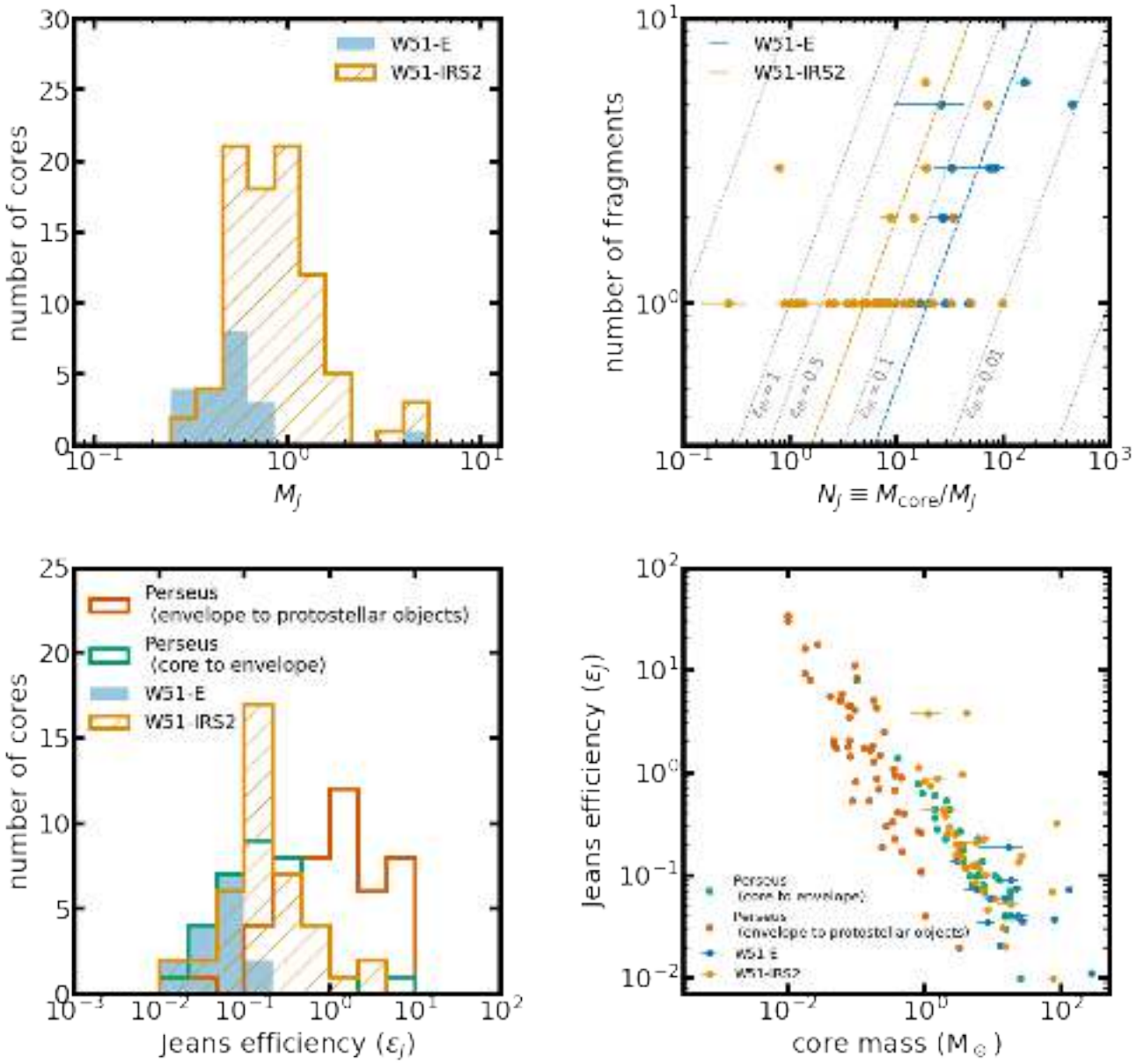

Figure 17. Upper left: the thermal Jeans masses of the cores in W51-E and W51-IRS2. Upper right: the Jeans number and number of core fragments. The ratio of the actual number of fragments to the Jeans number is the Jeans efficiency, indicated as gray dashed lines. The average Jeans efficiency in each region is plotted as colored thin dashed lines. Lower left: histogram of Jeans efficiency. For comparison, the Jeans efficiencies of envelopes in Perseus (R. Pokhrel et al. 2018) are also displayed in green. The average of Jeans efficiency in W51-E and W51-IRS2 is 5% and 20%, respectively, which are lower than the average in Perseus (∼40% for core to envelope and ∼50% for envelope to protostellar object). Lower right: core masses and Jeans efficiencies in W51-E, W51-IRS2, and Perseus (R. Pokhrel et al. 2018).

huge difference in the fragment counts at the central continuous structure around W51-North, where 10 fragments were reported in M. Tang et al. (2022), in contrast to a single PPO recognized in this study. We take a more conservative approach as the peaks in the continuous structure may represent transient substructure rather than embedded fragments. The higher abundance of fragments within the core results in an overestimation of the required CFE. The overestimation can be amplified by the fact that the short-baseline data were not included; the missing flux at large scales would lead to decreasing $M_{\rm core}/M_J \propto \rho^{3/2}$, and thereby raising the required CFE to reconcile with the observed fragment count.

The different fragment counts around W51-North may suggest that the result is dependent on the choice of `dendrogram` parameters. However, the sum of all the fragment masses only accounts for ∼20% of the core mass in M. Tang et al. (2022), indicating that our conclusion regarding the low fragmentation efficiency of massive cores—presented in Figure 15—remains valid despite the differences in the number of identified fragments.

5.1.2. Discussion on Insufficient Jeans Mass

Several possibilities may account for the low efficiency of fragmentation in W51-A: unresolved smaller fragments, underestimated Jeans masses, insufficient thermal pressure, and the growth of PPO mass.

S. S. R. Offner et al. (2023) listed candidates for additional physics halting the cascade of fragmentation, such as angular

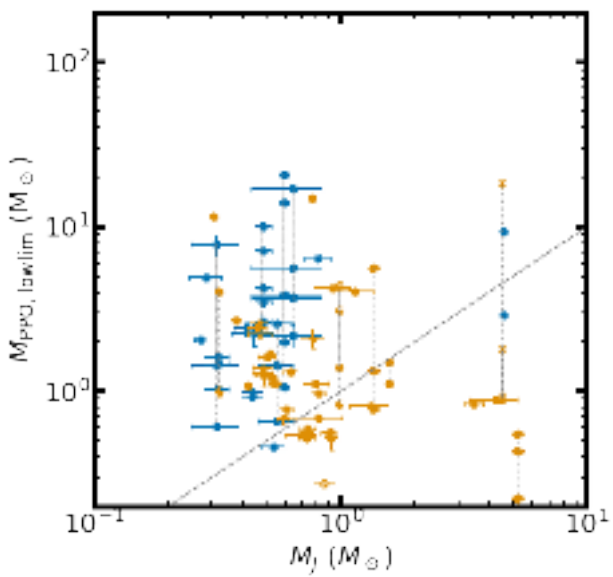

Figure 18. Comparison between the Jeans masses of the cores and the PPO masses associated with each core estimated from the constant temperature model ($T = 40$ K). The PPOs associated with the same core are connected with vertical dashed lines. A majority of the PPOs exhibit a lower mass limit exceeding the Jeans mass of the core.

momentum and magnetic support, and concluded that these limit the minimum scale of core fragmentation to ∼100 au. This scale is comparable to the sizes of most of our PPOs at 1.3 mm (Section 3.3), implying that we are most likely observing the final products of core fragmentation. In other words, each individual object in our sample is not likely to be composed of multiple spatially unresolved fragments that resulted from core fragmentation. We therefore exclude the possibility that we have misidentified a collection of multiple fragments as a single object, which would have resulted in the measured mass exceeding the Jeans mass ($M > M_J$).

Another explanation is that the Jeans masses of the cores evaluated from their current physical properties might be underestimated. Two factors could lead to an underestimated Jeans mass: the core temperature is estimated at low resolution, and the current density may have increased from the initial density (e.g., F. Xu et al. 2024). The core temperature used in our Jeans masses is derived from a PPMAP analysis (K. A. Marsh et al. 2015; P. Dell'Ova et al. 2024) with 2.″5 resolution, which is larger than the typical sizes of cores (∼1″). Thus, the core temperatures in the cores heated by central protostars may be underestimated (F. Motte et al. 2025). However, the cores at the time of the initial fragmentation, before the formation of the central protostar, are less likely influenced by protostellar heating, and thus the core temperature from low resolution may play a minor role. On the other hand, there is a chance that the current density is overestimated if the cores evolved significantly from the initial fragmentation stage. Indeed, several fragmentation models suggested that the parent structures continue to collapse while they form dense fragments within themselves (e.g., D. Guszejnov & P. F. Hopkins 2015, 2016; E. Vázquez-Semadeni et al. 2019). Since the Jeans mass has a negative power of density, evolved cores with a higher density could result in an underestimation of the Jeans mass.

In particular, an increase in mass by gas accretion from the parent core could be another reason for the observed $M_{\rm frag} > M_{\rm J}$. Indeed, C. Goddi et al. (2020) suggested that multidirectional accretion flows exist around hot cores in W51 such as W51e2e (#39 in W51-E), W51e8 (#32 in W51-E), and W51-North (#11 in W51-IRS2), which are all fragments of cores identified in this study. If we assume that the initial fragment masses are solely determined by the Jeans masses, the mass lower limits of fragments $M_{\rm frag} \simeq 0.1$–$200\,M_\odot$ in the constant temperature model (Figure 18) mean that many fragments should accrete most of their masses. The mass infall rates estimated by C. Goddi et al. (2020) for the three hot cores based on the outflow rates are $\sim$1–5 $\times$ 10^{-3} $M_\odot$ yr^{-1}. Assuming constant infall rates and a 50 K dust temperature, the mass lower limits of the three fragments, 57, 42, and 92 $M_\odot$, require gas infall times $t \sim$ 1–5 $\times$ 10^4 yr. Hence, the scenario that almost all the masses of fragments are acquired through accretion cannot be ruled out.

Given that the Jeans masses used in this study only consider thermal pressure, fragments more massive than their Jeans masses in Figure 18 may imply that the thermal pressure is insufficient to support the fragments against gravity. If this is true, we need other types of support, for example, turbulence, magnetic support, and/or rotation to account for the lower Jeans efficiencies, but none of them has been confirmed as a robust agent for nonthermal support at a scale of ∼100 au.

While none of these explanations provide conclusive evidence, our finding remains open to multiple processes, particularly the last two interpretations—nonthermal pressure and mass growth after the initial fragmentation. The suggested explanations might not be exclusive to each other. For example, magnetic stabilization in an accreting flow around massive PPOs can aid further growth of massive PPOs (P. M. Koch et al. 2022).

5.2. Unfragmented and Fragmented Cores

As illustrated in Section 4.1, we classified our core data sets into unfragmented and fragmented cores by the presence of fragments.

We present the temperature, size, and mass distributions of the unfragmented and fragmented cores without free–free emission (Figure 19). For the core temperatures and masses, we illustrated the derivation in Section 4.2. The size of each core is the average of the FWHM of the `getsf` source in the major and minor axis, $\theta_{\rm avg} \equiv (a_{\rm FWHM} \times b^2_{\rm FWHM})^{\frac{1}{3}}$. In W51-E, there are only five unfragmented cores, and thus W51-E is not suitable for unfragmented–fragmented core comparison. For this reason, we limit our comparison with the cores in W51-IRS2.

In W51-IRS2, the difference between core temperatures is small. Although the K-S test between the two populations yields a p-value of 3.86 $\times$ 10^{-2}, the medians of the core temperature are 29 and 31 K for the unfragmented and fragmented cores, respectively. This is probably because either the PPOs associated with the fragmented cores have not yet formed a protostellar system or the protostellar luminosity is not strong enough to heat the dusty region over the 2.″5 PPMAP resolution (equivalent to a physical scale $\sim 10^4$ au).

We find that the median of the size distribution is larger for unfragmented cores than for fragmented cores in W51-IRS2. On the other hand, the median mass of unfragmented cores is lower than that for the fragmented cores. Moreover, systematic differences exist in mass density between the unfragmented and fragmented cores—fragmented cores are denser than unfragmented cores. We evaluate the p-value from the two-

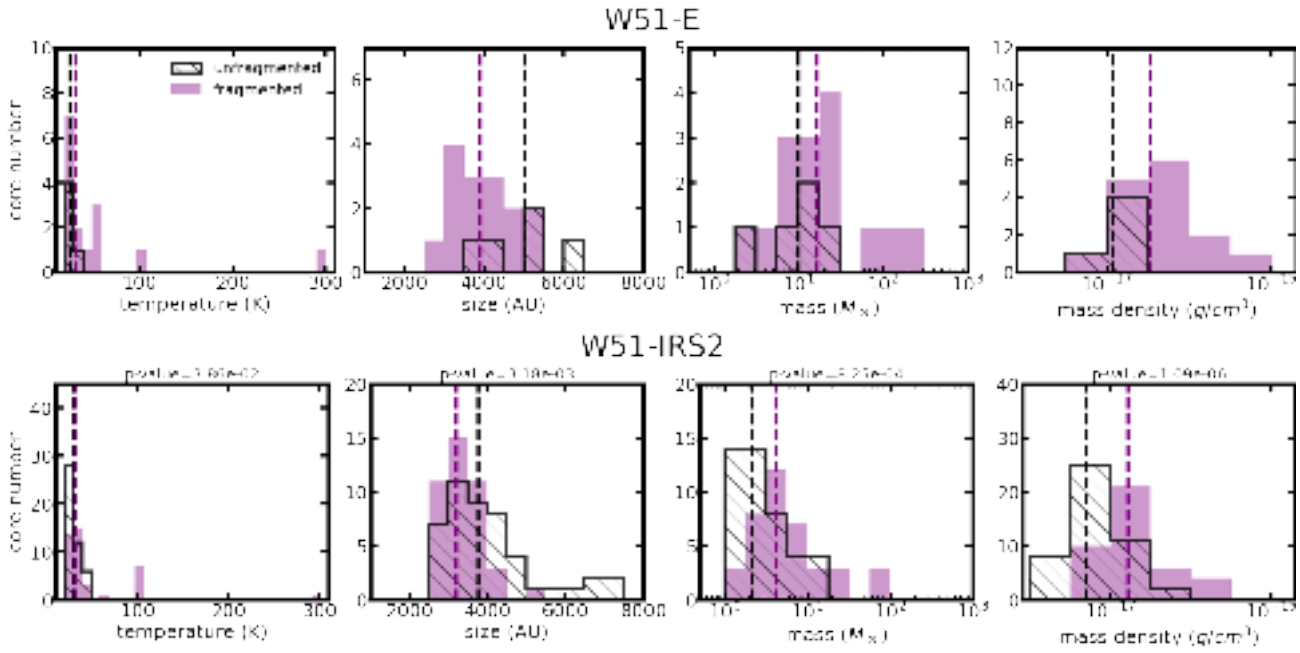

Figure 19. Histograms of temperatures, sizes, masses, and mass densities of the unfragmented and fragmented cores in W51-E (top) and W51-IRS2 (bottom). The median of each quantity is denoted by the vertical dashed line. The *p*-values from the two-sample Kolmogorov–Smirnov (K-S) test for the W51-IRS2 cores are displayed on the bottom row.

population K-S test, finding 3.18×10^{-3}, 8.25×10^{-4}, and 1.09×10^{-6} for sizes, masses, and mass densities, respectively. Therefore, those three physical quantities of the two populations are statistically distinct from each other.

Multiple interpretations of smaller, more massive, and denser fragmented cores are possible. Assuming that the cores are independent self-gravitating objects generated from the density structure by turbulence (e.g., C. F. McKee & J. C. Tan 2002, 2003) and that all the cores are formed at the same time, this trend can be simply a result of the faster collapse of initial denser cores due to their shorter freefall time ($t_{ff} \propto \rho^{-1/2}$). Another view is that cores grow in mass—more massive fragmented cores are the result of a net increase in mass as they evolve (e.g., T. Nony et al. 2023; M. Armante et al. 2024). In fact, gas infall onto dense cores has been found using dense gas kinematics from molecular line emission such as DCN, N_{2H}^+, and $H^{13}CO^+$ (e.g., P. Sanhueza et al. 2021; D. Yang et al. 2023; R. H. Álvarez-Gutiérrez et al. 2024; N. A. Sandoval-Garrido et al. 2025; S. Pan et al. 2024). If this is true, more massive fragmented cores are evidence of the clump-fed model where mass accreting onto protostars originates from spatial scales larger than cores. This clump-fed model was earlier supported by more massive protostellar cores than prestellar cores in other star-forming regions (T. Nony et al. 2023; M. Armante et al. 2024; K. Morii et al. 2024). While two different scenarios are possible, detailed studies of the lifetime and gas infall at each phase of cores are needed to differentiate the core evolution models.

5.3. Pre-/protostellar Objects outside Core Boundaries

5.3.1. Different Core-independent Pre-/protostellar Object Fractions between the Two Regions

The spatial correspondence between the PPOs and cores in Figures 9 and 10 shows that some PPOs are not associated with cores. A fraction of these PPOs were spatially related to free–free-contaminated cores that were removed from the core catalog, and thus they need to be treated separately from other PPOs that are associated with/independent of cores without free–free contamination. We classify our PPOs into three groups: core-associated PPOs (caPPOs), core-independent PPOs (ciPPOs), and free–free-contaminated core-associated PPOs (ffcaPPOs). In W51-E and W51-IRS2, we found 37 and 57 caPPOs, 69 and 27 ciPPOs, and 12 and 9 ffcaPPOs, respectively. A much higher fraction of PPOs (58%) in W51-E is unrelated to cores than those in W51-IRS2 (29%).

One explanation for the different number fractions of ciPPOs is the poorer completeness limit of the ALMA-IMF image of W51-E as explained in Section 4.1. Even if a PPO exists without any common envelope at the core scale, we would detect a point source at the same position in the ALMA-IMF image only if the noise level is sufficiently low. When we consider the core masses that are above the completeness limit of the W51-E ALMA-IMF image, 3.86 $M_\odot$, the number of caPPOs decreases from 37 to 36 in W51-E, while that of W51-IRS2 declines from 57 to 37. Also, the number of ffcaPPOs changes from 12 to 11 in W51-E and from nine to five in W51-IRS2. This results in a change of the fraction of caPPOs in W51-IRS2 from 61% to 54% while that of W51-E remains almost the same at 31%. Simply assuming Poisson errors, the difference is almost comparable to the uncertainty range (9% for W51-E and 10% for W51-IRS2). Thus, the different caPPO fractions between the two regions are mainly attributed to their different completeness limits. We will discuss whether other possible causes, e.g., an intrinsically different population, can explain the nondetection of cores in the next section.

5.3.2. Attempts to Characterize Core-independent Pre-/protostellar Objects

We further investigate the three different PPO groups, ciPPOs, caPPOs, and ffcaPPOs, by comparing several physical properties between them (Figure 20). In this analysis, we used

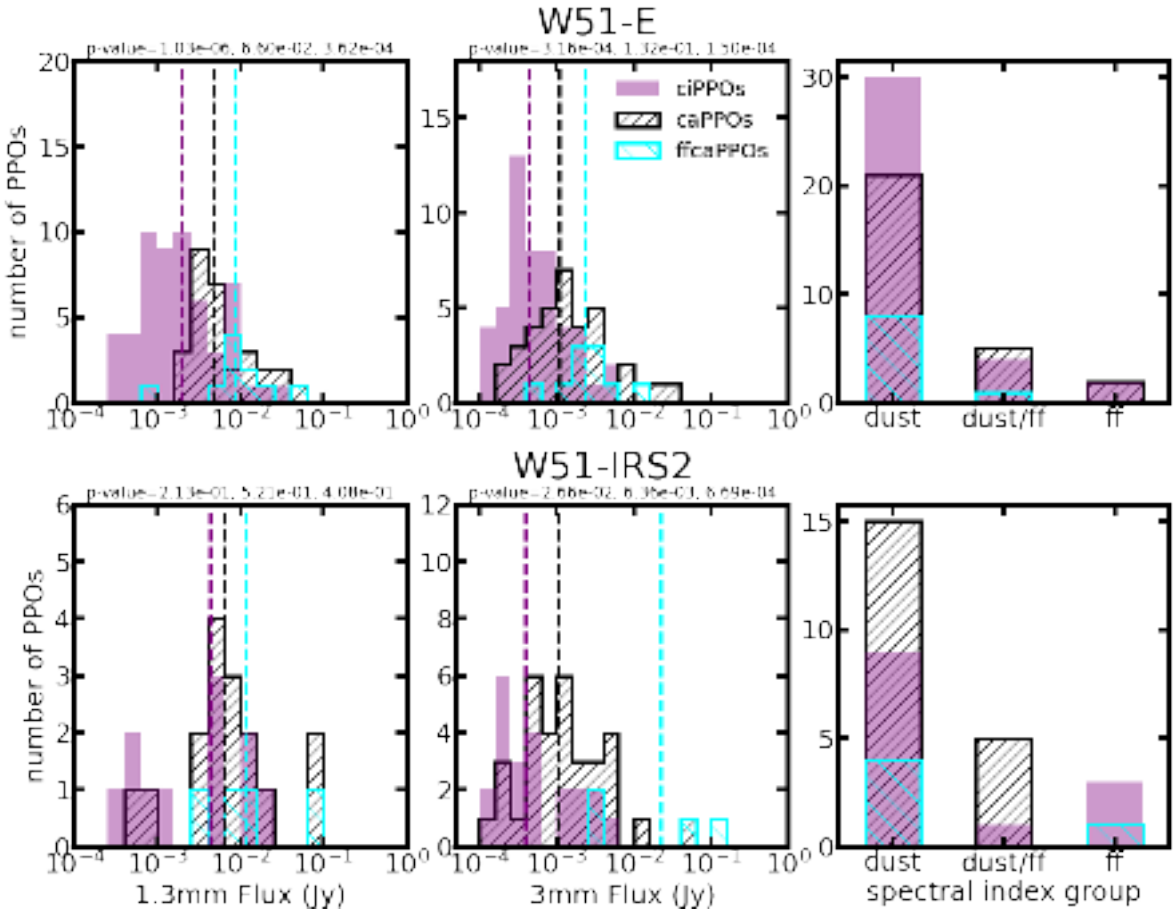

Figure 20. Comparison of 1.3 and 3 mm fluxes and spectral index groups (optically thick dust emission or possibly free–free contaminated and free–free contaminated), defined in Section 3.2, of ciPPOs, caPPOs, and ffcaPPOs in W51-E (top row) and W51-IRS2 (bottom). The core samples used in this plot have masses higher than the completeness limit of W51-E, 3.86 $M_{\odot}$. The median of each quantity is denoted by a vertical dashed line. The *p*-values of the two-sample K-S test for ciPPOs and caPPOs, caPPOs and ffcaPPOs, and ciPPOs and ffcaPPOs are displayed at the top of each panel.

mass-limited core samples with masses higher than the W51-E completeness limit ($M > 3.86\,M_{\odot}$) to eliminate possible observational effects. In W51-E, ciPPOs are distinctly fainter than other populations at both 1.3 and 3 mm. In W51-E, the *p*-values for the two-sample K-S tests are lower than 0.05 for the comparison between caPPOs/ffcaPPOs and ciPPOs at both bands, but the comparison between caPPOs and ffcaPPOs is not. This could be due to the insufficient number of ffcaPPOs. For the same reason, the *p*-values of the two-sample K-S test for W51-IRS2 are generally higher than 0.05 for all comparisons at 1.3 mm.

The higher fluxes of caPPOs relative to ciPPOs in W51-E can be explained by the previous argument that the faint PPOs are less likely to be identified in low-resolution images. In other words, caPPOs can be faint sources that are just not detected in the ALMA-IMF image.

Another possible factor for the nondetections in the ALMA-IMF image is a lack of gas in the reservoir at the core scale. Besides observational effects, there are several possibilities that make some PPOs appear independent of cores: PPOs rapidly escaped from their birthplace through, e.g., dynamical interaction (e.g., B. Reipurth & C. Clarke 2001), or PPOs formed earlier in an accreting flow that has subsequently dispersed (e.g., P. Girichidis et al. 2012), or PPOs at the end phase of mass accretion from cores, where most of the mass in these cores has already been transferred to PPOs (e.g., M. Fernández-López et al. 2011). In the last case, we expect that some of those PPOs that finished accreting could already contain massive stars creating HCH II regions. The higher fluxes of ciPPOs relative to caPPOs in both 1.3 and 3 mm fluxes might indicate that ciPPOs have smaller cold dust envelope masses because they are at a later stage where the envelope has been disrupted.

We attempt to characterize ciPPOs by investigating the spectral index groups (Section 3.2) of the two PPO populations (Figure 20), but we do not find any common trend between the two regions. In the W51-E and W51-IRS2 regions, the fractions of ciPPOs exhibiting free–free contamination are 5.6% and 23.1%, respectively. In contrast, the corresponding fractions for caPPOs are 7.2% in W51-E and 0.0% in W51-IRS2. Therefore, it is still uncertain whether the ciPPOs and caPPOs are intrinsically different populations.

6. Summary and Conclusions

6.1. Summary

In the first half of this paper, we characterize compact sources observed in long-baseline ALMA images (called PPOs) of the W51 high-mass star-forming region. The following is a summary of the characterization of PPOs.

1. After crossmatching candidate sources at 1.3 mm and 3 mm, we identified 118 compact sources in W51-E and 93 in W51-IRS2.
2. We measure the spectral indices of the PPOs between 1.3 mm and 3 mm. Based on the spectral indices, we classified our PPOs into three groups: dusty sources, sources with optically thick dust emission or free–free contamination, and sources dominated by free–free emission. In W51-E, 59 out of 70 sources, and in W51-IRS2, 13 out of 23 sources, are dominated by dust emission, exhibiting spectral indices $\alpha > 2$. The second group consists of 10 sources in W51-E and six in W51-IRS2, with spectral indices in the range $1.5 < \alpha < 2$; these are likely to be either optically thick dust emitters or sources with possible free–free contamination. The remaining four sources in W51-E and four in W51-IRS2 are certainly contaminated by free–free emission. In particular, the spectral index distribution peaks around two, indicating that many PPOs are optically thick at millimeter wavelengths (Section 3.2).
3. We measure the integrated flux of PPOs at 1.3 mm and 3 mm using a 2D Gaussian model. The measured fluxes are distributed over 10^{-4}–10^{-1} Jy. Assuming an MBB model, we infer the dust temperatures of PPOs for which fluxes at both 1.3 and 3 mm are available (47 in W51-E and six in W51-IRS2), ranging $T = 5$–60 K. We also estimate the mass lower limits of PPOs from the flux density of dust emission and a constant temperature $T = 40$ K. The estimated mass lower limits range from 0.1 to 200 $M_\odot$ for the constant temperature model.
4. We estimate the source sizes by deconvolving the 2D Gaussian fit from the image beam. The sources that are too small to be deconvolved are regarded as unresolved sources, and approximately 70% at 3 mm and 20%–30% at 1.3 mm are unresolved. The sizes of the resolved sources are distributed over 200–1000 au at 3 mm and 100–500 au at 1.3 mm.

The PPO catalogs made using the long-baseline images are linked to the cores extracted from ALMA-IMF short-baseline images by spatial correspondence. When we eliminated free–free-contaminated cores, we found that 15 out of 20 cores in W51-E and 41 out of 87 cores in W51-IRS2 have PPOs inside their FWHM boundaries. Here, we briefly review our findings about core fragmentation presented in Sections 4.2, 4.3, and 5.1.

1. We found that some cores fragment while others do not. The number of cores with 0, 1, and >1 fragments are five, six, and nine (25%, 30%, and 45%) in W51-E and 46, 34, and 7 (53%, 39%, and 8%) in W51-IRS2.
2. A high degree of fragmentation (i.e., $N_{\rm frag} \geqslant 3$) is only found in massive cores with $M_{\rm core} \gtrsim 4\,M_\odot$ (Figure 12).
3. Bright PPOs, which likely represent the progenitors of massive stars, are preferentially found in massive cores (Figure 13).
4. The distribution of fragment fluxes within a core is not uniform. The difference between the flux of the brightest source and the others in a given core is larger in more massive cores (Figure 14).
5. We do not find massive cores with a high fragmentation efficiency ($\epsilon_{\rm frag} \gtrsim 0.7$; Figure 15).
6. We find a suggestive trend that massive cores harboring bright (or massive) PPOs are warmer and have a lower fragmentation efficiency, but the number of samples ($N = 4$) is not large enough to draw a statistically significant conclusion.
7. The Jeans efficiency, which is the ratio between the Jeans number and the observed number of core fragments, tends to decrease with core mass (Figure 17).
8. Most PPOs have mass lower limits that exceed the Jeans mass of their parent cores (Figures 17 and 18).

Also, we further discuss the link between the cores and PPOs in Sections 5.2 and 5.3 as follows:

1. We classify our cores into unfragmented and fragmented cores with the presence of PPOs inside their boundaries (Figure 19). We find that the fragmented cores are systematically smaller in size, more massive, and denser than the unfragmented cores.
2. We found a larger fraction of PPOs in W51-E (58%) not spatially associated with cores than in W51-IRS2 (29%). This is mainly due to the observational effect that a higher completeness limit of the W51-E ALMA-IMF image reduces the sensitivity to detecting low-resolution counterparts of PPOs at the same locations.

6.2. Conclusions

Some of our findings provide important constraints on high-mass star formation models. We found that cores hosting bright PPOs, the progenitors of high-mass stars, are more massive, warmer, and contain more fragments compared with the average population. Our results do not necessarily indicate that high-mass stars form in initially massive cores, since the current core mass could be a result of accretion from larger scales (e.g., P. Padoan et al. 2020). Nevertheless, it is obvious that the core should be massive at the time when the core has high-mass PPOs that are actively accreting material.

We find evidence for suppressed fragmentation by protostellar heating in more massive cores. This evidence includes warmer core temperature and the presence of bright PPOs at higher masses. Heated gas is more prone to accrete onto a central high-mass protostar rather than making new fragments. In this way, the high-mass protostar is able to gain more mass. However, the number of core fragments is more likely to be controlled by the core mass (Figures 12 and 16) since protostellar heating is limited to the local area around the protostar. Furthermore, this result supports the idea that the higher degree of the multiplicity of massive stars in part comes from fragmentation on core scales (see the recent review of S. S. R. Offner et al. 2023).

Core fragmentation influences the mapping between the CMF and the IMF (see S. S. R. Offner et al. 2014). The trend that massive cores possess more PPOs is generally expected to steepen the slope of the CMF unless the initial CMF slope is too flat (e.g., $\alpha < -1$; B. Thomasson et al. 2025, in preparation). Other trends that can possibly change the CMF slope, e.g., different fragmentation efficiencies or mass ratios between fragments as a function of core mass, are not clearly confirmed in this study. The CMF slope change we expect from the $N_{\rm frag}$–$M_{\rm core}$ relation is limited to the evolution of the CMF to the PPO mass function, and thus the emerging IMF slope still can be affected by other processes, e.g., protostellar

jets (e.g., P. Hennebelle & M. Y. Grudić 2024) and dynamical ejection in cluster environments (e.g., S. Oh et al. 2015; S. Oh & P. Kroupa 2016).

Acknowledgments

We thank the anonymous reviewers for their feedback. This paper makes use of the following ALMA data: ADS/JAO. ALMA#2017.1.01355.L, ADS/JAO.ALMA#2015.1.01596.S, and ADS/JAO.ALMA# 2017.1.00293.S. ALMA is a partnership of ESO (representing its member states), NSF (USA), and NINS (Japan), together with NRC (Canada), MOST and ASIAA (Taiwan), and KASI (Republic of Korea), in cooperation with the Republic of Chile. The Joint ALMA Observatory is operated by ESO, AUI/NRAO, and NAOJ. The National Radio Astronomy Observatory is a facility of the National Science Foundation operated under cooperative agreement by Associated Universities, Inc. This research made use of `astrodendro`, a Python package to compute `dendrograms` of Astronomical data (http://www.dendrograms.org/). The figures in this paper make use of the Python visualization tools, `Matplotlib` (J. D. Hunter 2007) and `Seaborn` (M. L. Waskom 2021). The authors acknowledge University of Florida Research Computing for providing computational resources and support that have contributed to the research results reported in this publication; see http://www.rc.ufl.edu.

A.G. acknowledges support from the NSF under grants AAG 2008101 and 2206511 and CAREER 2142300. R.G.M. acknowledges support from UNAM-PAPIIT project IN105 225. A.G. and F.L. acknowledge the support of the program national "Physique et Chimie du Milieu Interstellaire" (PCMI) and program national "Physique Stellaire" (PNPS) of the CNRS/INSU with INC/INP cofunded by CEA and CNES. A.S. gratefully acknowledges support by the Fondecyt Regular (project code 1220610), and ANID BASAL project FB210003. L.B. gratefully acknowledges support by the ANID BASAL project FB210003. P.S. was partially supported by a Grant-in-Aid for Scientific Research (KAKENHI Numbers JP22H 01271 and JP23H01221) of JSPS. P.S. was supported by the Yoshinori Ohsumi Fund (Yoshinori Ohsumi Award for Fundamental Research). F.M., F.L., B.T., M.V.M., and A.G. have received funding from the European Research Council (ERC) via the ERC Synergy Grant ECOGAL (grant 855130) and from the French Agence Nationale de la Recherche (ANR) through the project COSMHIC (ANR-20-CE31-0009). G.B. acknowledges support from the PID2023-146675NB-I00 (MCI-AEI-FEDER, UE) program.

Facilities: ALMA.

Software: CASA (version 5.7.0; J. P. McMullin et al. 2007), CARTA (C. R. Harris et al. 2020; A. Comrie et al. 2024), `numpy` (A. Comrie et al. 2021), `scipy` (P. Virtanen et al. 2020), `astropy` (Astropy Collaboration et al. 2013, 2018), `astrodendro` (E. W. Rosolowsky et al. 2008), `dendrocat`, `radio_beam`, `lifeline` (C. Davidson-Pilon 2019), `TGIF` (T. Yoo & A. Ginsburg 2024).

Appendix A
Pre-/protostellar Object Flux Measurement with a Two-dimensional Gaussian Model

In this appendix, we illustrate the procedure of measuring the fluxes of fragments from the continuum images. The modeling process consists of three steps: subpixel offset adjustment, local background noise estimation, and flux measurement with the 2D Gaussian model. The whole process of measuring the flux and size of sources is available in the Python package `TGIF`. The source code of `TGIF` can be found at the GitHub page[30] and Zenodo (T. Yoo & A. Ginsburg 2024).

To model each source with a 2D Gaussian, we first need to find the peak position. By default, the peak of the `dendrogram` source is the center of the brightest image pixel. However, the discrete representation of a continuous light profile with pixels has a limitation in marking the precise peak position. For this reason, we adjusted the subpixel offset of the real peak position in the image. The adjustment process is achieved by fitting a 1D Gaussian model to the image profile near the peak. We extracted the 1D image profile along the major and minor axes of the image beam. For modeling the 1D Gaussian curve, we utilized `curve_fit` of the `scipy` (P. Virtanen et al. 2020) Python package. When we fit the 1D Gaussian model, we measure the offset between the previous peak and the peak of the model and adjust the peak position by the offset. We repeat this process until the offset is measured to be smaller than 1% of the pixel size.

After adjusting the subpixel offset of the peak position, we conduct an initial 2D Gaussian fitting before the local background subtraction. We use the linear chi-square method to minimize the residual function defined as the difference between the image and the 2D Gaussian model. We use a small cutout of the image centered on the peak of the source to compute the residual function to minimize the effect of the surrounding structure. In addition, we give more weight to the pixels producing the negative residual (image − model < 0) in the residual function in order to prevent the case where the fitting function overestimates the size of the source due to any neighboring structure. For pixels with a negative residual, the weight in each pixel is computed by the median absolute deviation of the local background σ multiplied by the exponential of the offset in each pixel such that $\sigma_{\rm weighted} = \sigma \exp(\lambda|x_{\rm image} - x_{\rm model}|)$ where $x_{\rm model}$ and $x_{\rm image}$ are the pixel values of the image and the model, respectively, and $\lambda = 100$ is a penalty factor. Then σ is used to evaluate the chi-square residual function to be minimized, $\chi^2 = \sum[(x_{\rm image} - x_{\rm model})^2/\sigma^2]$. This is one of the main philosophies of this method to accurately measure the flux and size of the source, which are often surrounded by the diffuse emission as seen in Figures 9 and 10. We utilize the minimizer tool `LMFIT` (M. Newville et al. 2015) to optimize the 2D Gaussian model. The 2D Gaussian model has four free parameters: standard deviations along the major axis ($\sigma_{\rm major}$) and minor axis ($\sigma_{\rm minor}$), the position angle (θ), and the base flux density ($F_{\rm base}$), which is the flux density that the 2D Gaussian converges to as the offset from the center goes to infinity. Other parameters, i.e., the positions and the height of the peak, are fixed to those of the image.

The local background value is then evaluated from an elliptical annulus around the peak of each source (lower panels in Figure 21). The annulus is enclosed by two ellipses, each representing the FWHM of the two Gaussian models obtained from the initial fitting extended by factors of 2 and 3, respectively. The local background value is then determined by the median of the pixel values in the annulus. To minimize

[30] https://github.com/tyoo37/TGIF

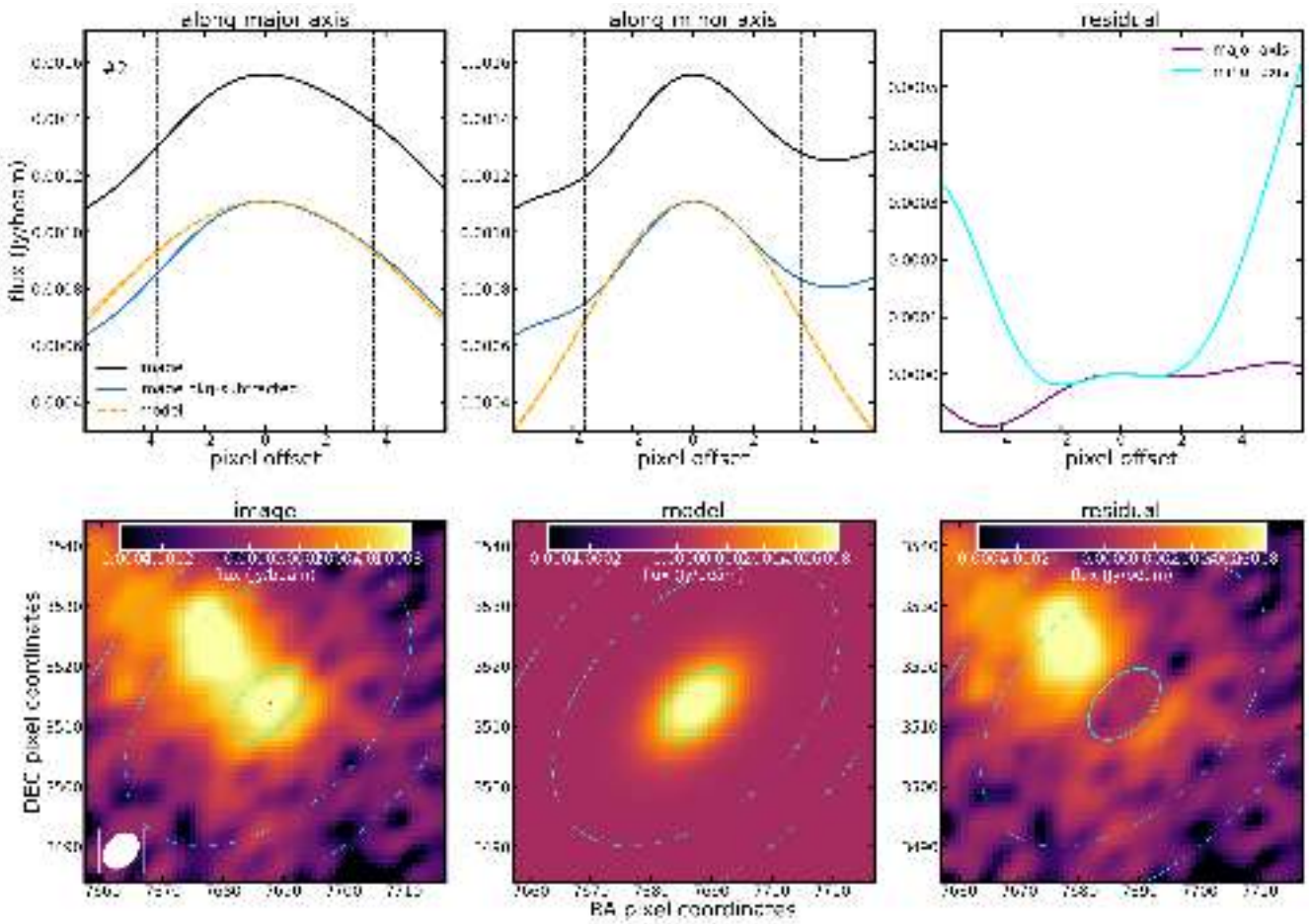

Figure 21. An example of 2D Gaussian modeling for the ALMA 1.3 mm flux measurement of PPOs (#2) in W51-E. Upper row: the 1D profile of the continuum image and the model along the major axis (left) and minor axis (center). The solid lines indicate the image profile before (black) and after background subtraction (blue). The orange dashed lines represent the model profile fitted to the background-subtracted image profile. The residual, the image profile subtracted by the model, is presented on the upper right panel. Bottom row: cutouts of the original image (lower left), the model (lower center), and the residual image (lower right). The cyan solid ellipse at the center indicates the FWHM of the 2D Gaussian model whereas the cyan dashed ellipses are the annulus where the local background value is evaluated. The size of the synthesized beam of the image is displayed in the left lower corner.

contamination from known sources, we masked out the regions with 2× the beam size centered on each cataloged peak.

Next, we carry out the 2D Gaussian fitting again from the local background-subtracted image. Once the 2D Gaussian model was obtained, we computed the integrated flux from the volume of the model $V = 2\pi A\sigma_{\rm major}\sigma_{\rm minor}$, where A is the peak flux density. We also measured the physical size of the source by deconvolving the FWHM along both axes with the beam with the aid of `radio_beam` Python package.

Appendix B
The Completeness Test

The completeness limit of the PPO detection is determined by injecting synthetic sources into regular grids of the image, as was done previously in the ALMA-IMF project (e.g., Y. Pouteau et al. 2022). Given that the 3 mm flux is used for mass estimation, we only test the 3 mm continuum images. The synthetic sources are created by a 2D Gaussian with the median size of our samples (∼100 au). We injected synthetic sources with 11 different fluxes corresponding to mass values ranging from 0.05 $M_\odot$ to 1 $M_\odot$ at a 50 K temperature using optically thin dust emission (Equation (5)). To take into account the different probabilities of detection for different background levels, we placed synthetic sources on the grids with sizes of 100 pixels (∼0.″7). In total, we created 2210 and 2086 sources on the images of W51-E and W51-IRS2, respectively.

The completeness level of the synthetic sources is displayed in Figure 22. The completeness level is defined as the fraction of synthetic sources identified by `dendrogram` with the same parameters used in finding our PPO samples. We define the mass reaching a 0.9 completeness level as the completeness limit. By interpolating the result produced at discrete masses using the PCHIP interpolator, we obtain the completeness limits of W51-E and W51-IRS2, 0.25 mJy and 0.20 mJy, respectively, in Band 3 and 1.2 and 1.3 mJy, in Band 6. Assuming a 40 K dust temperature, inserting the Band 3 fluxes into Equation (5) produces to 0.631 $M_\odot$ and 0.505 $M_\odot$ in W51-E and W51-IRS2, respectively.

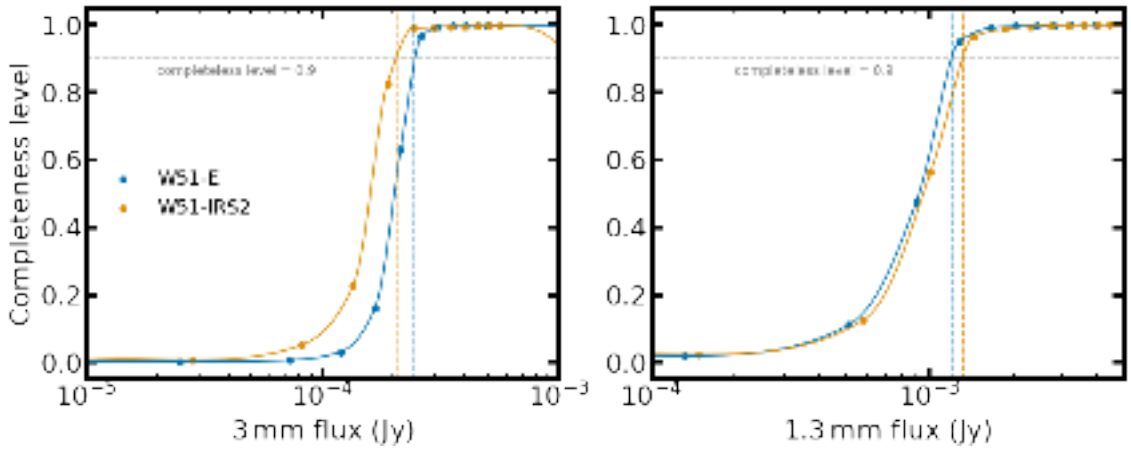

Figure 22. The completeness test result. We define the completeness limit mass as the mass reaching the completeness level = 0.9. Each point is generated by testing if the synthetic sources are detected by `dendrogram` or not. The interpolation between points is done with PCHIP interpolator.

Appendix C
Pre-/protostellar Object Catalogs

We present PPO catalogs containing the sky coordinates and their photometric fluxes (Tables 2–5). The full machine-readable form of the catalogs is available at DOI:10.5281/zenodo.16235156.

Table 2
Basic Properties of the Pre-/protostellar Object Catalog of W51-E: the First 30 Entries

ID	R.A. (deg)	Decl. (deg)	$F_{\rm peak,1.3\ mm}$ (Jy beam^{-1})	$F_{\rm peak,3\ mm}$ (Jy beam^{-1})	Spectral Index	Spectral Index Group
0	290.93232	14.50541	1.31×10^{-3}	2.62×10^{-4}	2.9 ± 0.1	dust dominated
1	290.93237	14.50546	1.41×10^{-3}	3.01×10^{-4}	2.4 ± 0.1	dust dominated
2	290.93246	14.50546	1.11×10^{-3}	6.54×10^{-4}	2.3 ± 0.0	dust dominated
3	290.93246	14.50551	1.44×10^{-3}	1.55×10^{-4}	3.2 ± 0.1	dust dominated
4	290.93225	14.50594	3.8×10^{-3}	9.09×10^{-4}	2.8 ± 0.0	dust dominated
5	290.93258	14.50593	7.24×10^{-4}	2.28×10^{-4}	2.4 ± 0.1	dust dominated
6	290.93261	14.50596	7.97×10^{-4}	2.12×10^{-4}	2.4 ± 0.1	dust dominated
7	290.93128	14.50607	1.31×10^{-3}	1.17×10^{-3}	0.6 ± 0.1	free–free dominated
8	290.93236	14.50621	3.81×10^{-3}	1.75×10^{-3}	2.2 ± 0.0	dust dominated
9	290.93248	14.50622	2.02×10^{-3}	1.07×10^{-3}	2.3 ± 0.0	dust dominated
10	290.93243	14.50624	2.32×10^{-3}	1.03×10^{-3}	2.2 ± 0.0	dust dominated
11	290.93258	14.5065	1.64×10^{-3}	4.14×10^{-4}	2.6 ± 0.0	dust dominated
12	290.93261	14.5065	5.75×10^{-4}	5.29×10^{-4}	1.8 ± 0.1	optically thick or possibly ff
13	290.93263	14.50699	7.69×10^{-4}	4.89×10^{-4}	2.2 ± 0.0	dust dominated
14	290.93079	14.507	7.32×10^{-4}	2.02×10^{-4}	2.3 ± 0.1	dust dominated
15	290.93341	14.50702	6.24×10^{-4}	1.65×10^{-4}	2.7 ± 0.1	dust dominated
16	290.93372	14.50703	1.31×10^{-3}	4.32×10^{-4}	2.3 ± 0.1	dust dominated
17	290.93343	14.50704	6.4×10^{-4}	1.48×10^{-4}	2.5 ± 0.1	dust dominated
18	290.9333	14.50714	6.9×10^{-4}	2.34×10^{-4}	2.5 ± 0.1	dust dominated
19	290.93325	14.50726	1.51×10^{-3}	1.82×10^{-4}	3.2 ± 0.1	dust dominated
20	290.93272	14.50736	9.12×10^{-4}	3.07×10^{-4}	2.7 ± 0.0	dust dominated
21	290.93275	14.50738	3.47×10^{-3}	2.54×10^{-3}	1.9 ± 0.0	optically thick or possibly ff
22	290.93281	14.50742	9.0×10^{-4}	5.03×10^{-4}	2.4 ± 0.0	dust dominated
23	290.93347	14.50755	1.53×10^{-3}	1.22×10^{-3}	1.8 ± 0.0	optically thick or possibly ff
24	290.93315	14.50755	6.81×10^{-4}	1.36×10^{-4}	2.6 ± 0.2	dust dominated
25	290.93274	14.50757	2.14×10^{-3}	4.27×10^{-4}	3.0 ± 0.0	dust dominated
26	290.93289	14.50758	3.03×10^{-3}	1.29×10^{-3}	2.5 ± 0.0	dust dominated
27	290.93497	14.50759	4.57×10^{-4}	8.6×10^{-5}	2.5 ± 0.3	dust dominated
28	290.93291	14.50764	1.63×10^{-3}	2.01×10^{-3}	1.8 ± 0.0	optically thick or possibly ff
29	290.93294	14.50771	3.05×10^{-3}	3.62×10^{-3}	1.1 ± 0.0	free–free dominated

Table 3
Basic Properties of the Pre-/protostellar Object Catalog in W51-IRS2: the First 30 Entries

ID	R.A. (deg)	Decl. (deg)	$F_{\rm peak,1.3\ mm}$ (Jy beam^{-1})	$F_{\rm peak,3\ mm}$ (Jy beam^{-1})	Spectral Index	Spectral Index Group
0	290.91465	14.5176	1.9×10^{-3}	3.68×10^{-4}	2.9 ± 0.1	dust dominated
1	290.91496	14.51782	2.29×10^{-3}	9.51×10^{-4}	1.9 ± 0.0	optically thick or possibly ff
2	290.91711	14.5179	2.71×10^{-3}	1.68×10^{-3}	0.7 ± 0.0	free–free dominated
3	290.9182	14.51792	4.13×10^{-4}	8.46×10^{-5}	2.3 ± 0.3	dust dominated
4	290.91591	14.51801	2.1×10^{-2}	4.21×10^{-2}	0.2 ± 0.0	free–free dominated
5	290.91551	14.5181	2.8×10^{-3}	1.71×10^{-3}	2.2 ± 0.0	dust dominated
6	290.91586	14.5181	1.15×10^{-3}	6.06×10^{-4}	2.3 ± 0.0	dust dominated
7	290.91564	14.51811	2.01×10^{-3}	7.79×10^{-4}	2.7 ± 0.0	dust dominated
8	290.91619	14.51813	9.91×10^{-4}	5.11×10^{-4}	2.3 ± 0.0	dust dominated
9	290.91596	14.51815	3.2×10^{-3}	1.38×10^{-3}	2.3 ± 0.0	dust dominated
10	290.91648	14.51815	4.17×10^{-3}	3.89×10^{-3}	1.8 ± 0.0	optically thick or possibly ff
11	290.91688	14.51819	6.24×10^{-3}	8.41×10^{-3}	1.8 ± 0.0	optically thick or possibly ff
12	290.91606	14.51817	1.36×10^{-3}	2.41×10^{-4}	2.7 ± 0.1	dust dominated
13	290.91694	14.51818	2.37×10^{-3}	1.78×10^{-3}	1.8 ± 0.0	optically thick or possibly ff
14	290.9156	14.51822	7.86×10^{-4}	3.92×10^{-4}	2.2 ± 0.1	dust dominated
15	290.917	14.51826	1.86×10^{-3}	4.72×10^{-4}	2.8 ± 0.0	dust dominated
16	290.91708	14.51824	8.9×10^{-3}	3.62×10^{-3}	1.5 ± 0.0	free–free dominated
17	290.91661	14.51826	1.16×10^{-3}	2.48×10^{-4}	2.9 ± 0.0	dust dominated
18	290.91707	14.51827	6.68×10^{-3}	2.32×10^{-3}	1.4 ± 0.0	free–free dominated
19	290.91716	14.51827	6.31×10^{-3}	1.91×10^{-3}	1.8 ± 0.0	optically thick or possibly ff
20	290.91662	14.51828	1.8×10^{-3}	1.69×10^{-3}	1.9 ± 0.0	optically thick or possibly ff
21	290.91666	14.51837	2.96×10^{-3}	1.42×10^{-3}	2.1 ± 0.0	dust dominated
22	290.92055	14.51877	1.39×10^{-3}	2.87×10^{-4}	2.1 ± 0.1	dust dominated
23	290.92035	14.51407	⋯	1.29×10^{-4}	⋯	⋯
24	290.91722	14.5173	⋯	1.12×10^{-4}	⋯	⋯
25	290.9168	14.51816	⋯	1.87×10^{-3}	⋯	⋯
26	290.9168	14.51822	⋯	7.9×10^{-4}	⋯	⋯
27	290.91667	14.5183	⋯	3.15×10^{-4}	⋯	⋯
28	290.9115	14.51868	⋯	1.92×10^{-4}	⋯	⋯
29	290.91916	14.51875	⋯	1.93×10^{-4}	⋯	⋯

Table 4
Photometric Properties of the Pre-/protostellar Object Catalog of W51-E: the First 30 Entries

ID	$F_{\rm int,1.3\ mm}$ (Jy)	$F_{\rm int,3\ mm}$ (Jy)	$T_{\rm MBB}$ (K)	$M_{\rm lowlim}$ ($M_\odot$)	$a_{1.3\ \rm mm} \times b_{1.3\ \rm mm}$ (au × au)	$a_{3\ \rm mm} \times b_{3\ \rm mm}$ (au × au)
0	$3.8 \times 10^{-3} \pm 1.2 \times 10^{-4}$	$6.4 \times 10^{-4} \pm 2.3 \times 10^{-5}$	16	$1.6 \times 10^{0} \pm 5.8 \times 10^{-2}$	160 × 75	⋯
1	$2.5 \times 10^{-3} \pm 4.7 \times 10^{-5}$	$5.7 \times 10^{-4} \pm 5.7 \times 10^{-6}$	⋯	$1.4 \times 10^{0} \pm 1.4 \times 10^{-2}$	⋯	⋯
2	$5.8 \times 10^{-3} \pm 1.9 \times 10^{-4}$	$3.1 \times 10^{-3} \pm 4.6 \times 10^{-4}$	⋯	$7.8 \times 10^{0} \pm 1.2 \times 10^{0}$	290 × 115	546 × 292
3	$3.8 \times 10^{-3} \pm 1.3 \times 10^{-4}$	$2.4 \times 10^{-4} \pm 3.3 \times 10^{-6}$	18	$6.1 \times 10^{-1} \pm 8.3 \times 10^{-3}$	⋯	⋯
4	$1.5 \times 10^{-2} \pm 1.8 \times 10^{-4}$	$2.0 \times 10^{-3} \pm 2.7 \times 10^{-5}$	53	$5.0 \times 10^{0} \pm 6.8 \times 10^{-2}$	215 × 98	⋯
5	$1.3 \times 10^{-3} \pm 7.9 \times 10^{-5}$	$4.0 \times 10^{-4} \pm 2.7 \times 10^{-5}$	11	$1.0 \times 10^{0} \pm 6.7 \times 10^{-2}$	⋯	⋯
6	$1.2 \times 10^{-3} \pm 1.2 \times 10^{-5}$	$3.0 \times 10^{-4} \pm 1.6 \times 10^{-5}$	⋯	$7.6 \times 10^{-1} \pm 4.1 \times 10^{-2}$	⋯	⋯
7	$2.3 \times 10^{-3} \pm 8.2 \times 10^{-5}$	$1.8 \times 10^{-3} \pm 6.8 \times 10^{-6}$	⋯	$4.5 \times 10^{0} \pm 1.7 \times 10^{-2}$	⋯	⋯
8	$2.3 \times 10^{-2} \pm 5.0 \times 10^{-4}$	$3.5 \times 10^{-3} \pm 4.9 \times 10^{-5}$	58	$8.7 \times 10^{0} \pm 1.2 \times 10^{-1}$	242 × 200	⋯
9	$1.2 \times 10^{-2} \pm 4.5 \times 10^{-4}$	$2.9 \times 10^{-3} \pm 1.9 \times 10^{-5}$	⋯	$7.2 \times 10^{0} \pm 4.9 \times 10^{-2}$	276 × 158	⋯
10	$1.4 \times 10^{-2} \pm 5.3 \times 10^{-4}$	$2.5 \times 10^{-3} \pm 1.1 \times 10^{-4}$	⋯	$6.4 \times 10^{0} \pm 2.7 \times 10^{-1}$	294 × 144	⋯
11	$6.5 \times 10^{-3} \pm 2.2 \times 10^{-4}$	$7.6 \times 10^{-4} \pm 5.2 \times 10^{-6}$	23	$1.9 \times 10^{0} \pm 1.3 \times 10^{-2}$	184 × 142	⋯
12	$2.1 \times 10^{-3} \pm 1.3 \times 10^{-5}$	$1.4 \times 10^{-3} \pm 1.7 \times 10^{-5}$	⋯	$3.5 \times 10^{0} \pm 4.2 \times 10^{-2}$	202 × 94	⋯
13	$3.4 \times 10^{-3} \pm 2.4 \times 10^{-4}$	$1.7 \times 10^{-3} \pm 1.2 \times 10^{-5}$	⋯	$4.2 \times 10^{0} \pm 3.1 \times 10^{-2}$	241 × 119	⋯
14	$2.5 \times 10^{-3} \pm 4.9 \times 10^{-5}$	$3.7 \times 10^{-4} \pm 8.5 \times 10^{-6}$	10	$9.5 \times 10^{-1} \pm 2.1 \times 10^{-2}$	182 × 104	⋯
15	$1.4 \times 10^{-3} \pm 4.4 \times 10^{-5}$	$4.1 \times 10^{-4} \pm 3.7 \times 10^{-6}$	12	$1.0 \times 10^{0} \pm 9.4 \times 10^{-3}$	⋯	⋯
16	$6.1 \times 10^{-3} \pm 8.3 \times 10^{-5}$	$8.7 \times 10^{-4} \pm 9.9 \times 10^{-6}$	18	$2.2 \times 10^{0} \pm 2.5 \times 10^{-2}$	298 × 67	⋯
17	$1.4 \times 10^{-3} \pm 6.7 \times 10^{-5}$	$2.8 \times 10^{-4} \pm 3.6 \times 10^{-6}$	8	$7.2 \times 10^{-1} \pm 9.1 \times 10^{-3}$	⋯	⋯
18	$1.9 \times 10^{-3} \pm 1.3 \times 10^{-4}$	$1.7 \times 10^{-3} \pm 1.3 \times 10^{-4}$	9	$4.2 \times 10^{0} \pm 3.3 \times 10^{-1}$	153 × 78	899 × 255
19	$5.2 \times 10^{-3} \pm 1.5 \times 10^{-4}$	$3.5 \times 10^{-4} \pm 3.7 \times 10^{-6}$	24	$8.9 \times 10^{-1} \pm 9.3 \times 10^{-3}$	198 × 85	⋯
20	$3.7 \times 10^{-3} \pm 3.0 \times 10^{-4}$	$8.7 \times 10^{-4} \pm 1.3 \times 10^{-4}$	⋯	$2.2 \times 10^{0} \pm 3.3 \times 10^{-1}$	205 × 127	⋯
21	$3.1 \times 10^{-2} \pm 9.3 \times 10^{-4}$	$6.7 \times 10^{-3} \pm 3.7 \times 10^{-5}$	⋯	$1.7 \times 10^{1} \pm 9.3 \times 10^{-2}$	298 × 270	⋯
22	$4.6 \times 10^{-3} \pm 3.2 \times 10^{-4}$	$1.5 \times 10^{-3} \pm 4.9 \times 10^{-5}$	17	$3.7 \times 10^{0} \pm 1.2 \times 10^{-1}$	251 × 148	391 × 126
23	$8.9 \times 10^{-3} \pm 2.4 \times 10^{-4}$	$4.3 \times 10^{-3} \pm 1.1 \times 10^{-4}$	⋯	$1.1 \times 10^{1} \pm 2.8 \times 10^{-1}$	249 × 185	394 × 244

Table 4
(Continued)

ID	$F_{\rm int,1.3\ mm}$ (Jy)	$F_{\rm int,3\ mm}$ (Jy)	$T_{\rm MBB}$ (K)	$M_{\rm lowlim}$ ($M_\odot$)	$a_{1.3\ \rm mm} \times b_{1.3\ \rm mm}$ (au × au)	$a_{3\ \rm mm} \times b_{3\ \rm mm}$ (au × au)
24	$1.4 \times 10^{-3} \pm 3.6 \times 10^{-5}$	$2.6 \times 10^{-4} \pm 2.7 \times 10^{-6}$	5	$6.6 \times 10^{-1} \pm 6.8 \times 10^{-3}$	⋯	⋯
25	$6.7 \times 10^{-3} \pm 1.7 \times 10^{-4}$	$7.5 \times 10^{-4} \pm 4.4 \times 10^{-6}$	24	$1.9 \times 10^{0} \pm 1.1 \times 10^{-2}$	185×67	⋯
26	$2.7 \times 10^{-2} \pm 1.4 \times 10^{-3}$	$4.1 \times 10^{-3} \pm 7.3 \times 10^{-5}$	40	$1.0 \times 10^{1} \pm 1.8 \times 10^{-1}$	376×212	448×97
27	$7.7 \times 10^{-4} \pm 3.0 \times 10^{-5}$	$1.0 \times 10^{-4} \pm 1.9 \times 10^{-6}$	5	$2.6 \times 10^{-1} \pm 4.8 \times 10^{-3}$	⋯	⋯
28	$9.1 \times 10^{-3} \pm 2.1 \times 10^{-4}$	$6.0 \times 10^{-3} \pm 1.5 \times 10^{-4}$	⋯	$1.5 \times 10^{1} \pm 3.7 \times 10^{-1}$	264×156	⋯
29	$5.2 \times 10^{-3} \pm 5.3 \times 10^{-5}$	$5.5 \times 10^{-3} \pm 3.2 \times 10^{-5}$	⋯	$1.4 \times 10^{1} \pm 8.1 \times 10^{-2}$	⋯	⋯

Table 5
Photometric Properties of the Pre-/protostellar Object Catalog of W51-IRS2: the First 30 Entries

ID	$F_{\rm int,1.3\ mm}$	$F_{\rm int,3\ mm}$	$T_{\rm MBB}$	$M_{\rm lowlim}$	$a_{1.3\ \rm mm} \times b_{1.3\ \rm mm}$	$a_{3\ \rm mm} \times b_{3\ \rm mm}$
0	$5.8 \times 10^{-3} \pm 1.0 \times 10^{-4}$	$8.5 \times 10^{-4} \pm 2.6 \times 10^{-5}$	26	$8.3 \times 10^{-1} \pm 2.6 \times 10^{-2}$	174×71	⋯
1	$7.8 \times 10^{-3} \pm 1.7 \times 10^{-4}$	$1.6 \times 10^{-3} \pm 9.2 \times 10^{-6}$	⋯	$4.1 \times 10^{0} \pm 2.3 \times 10^{-2}$	176×106	⋯
2	$4.3 \times 10^{-3} \pm 4.0 \times 10^{-5}$	$2.3 \times 10^{-3} \pm 6.2 \times 10^{-6}$	⋯	$5.9 \times 10^{0} \pm 1.6 \times 10^{-2}$	⋯	⋯
3	$7.4 \times 10^{-4} \pm 2.7 \times 10^{-5}$	$1.1 \times 10^{-4} \pm 1.4 \times 10^{-6}$	4	$2.7 \times 10^{-1} \pm 3.5 \times 10^{-3}$	⋯	⋯
4	$7.7 \times 10^{-2} \pm 2.2 \times 10^{-3}$	$1.2 \times 10^{-1} \pm 1.4 \times 10^{-3}$	⋯	$3.1 \times 10^{2} \pm 3.5 \times 10^{0}$	165×144	378×88
5	$2.1 \times 10^{-2} \pm 3.6 \times 10^{-3}$	$5.8 \times 10^{-3} \pm 5.5 \times 10^{-5}$	50	$5.6 \times 10^{0} \pm 5.4 \times 10^{-2}$	276×235	456×95
6	$8.6 \times 10^{-3} \pm 1.7 \times 10^{-4}$	$3.4 \times 10^{-3} \pm 9.6 \times 10^{-5}$	31	$8.5 \times 10^{0} \pm 2.4 \times 10^{-1}$	293×221	573×387
7	$5.5 \times 10^{-3} \pm 1.5 \times 10^{-4}$	$1.4 \times 10^{-3} \pm 4.8 \times 10^{-6}$	⋯	$1.3 \times 10^{0} \pm 4.7 \times 10^{-3}$	⋯	⋯
8	$5.5 \times 10^{-3} \pm 7.0 \times 10^{-4}$	$1.7 \times 10^{-3} \pm 1.2 \times 10^{-5}$	⋯	$4.2 \times 10^{0} \pm 2.9 \times 10^{-2}$	280×142	⋯
9	$1.5 \times 10^{-2} \pm 2.6 \times 10^{-4}$	$3.5 \times 10^{-3} \pm 5.1 \times 10^{-5}$	⋯	$8.8 \times 10^{0} \pm 1.3 \times 10^{-1}$	203×167	⋯
10	$7.2 \times 10^{-2} \pm 4.5 \times 10^{-3}$	$1.5 \times 10^{-2} \pm 5.7 \times 10^{-4}$	⋯	$1.5 \times 10^{1} \pm 5.6 \times 10^{-1}$	542×315	478×221
11	$6.4 \times 10^{-2} \pm 3.9 \times 10^{-3}$	$5.7 \times 10^{-2} \pm 2.3 \times 10^{-3}$	⋯	$1.8 \times 10^{1} \pm 7.4 \times 10^{-1}$	346×278	625×449
12	$6.1 \times 10^{-3} \pm 9.0 \times 10^{-5}$	$5.8 \times 10^{-4} \pm 1.5 \times 10^{-5}$	20	$1.5 \times 10^{0} \pm 3.7 \times 10^{-2}$	239×118	⋯
13	$3.8 \times 10^{-3} \pm 1.4 \times 10^{-4}$	$2.7 \times 10^{-3} \pm 7.1 \times 10^{-5}$	⋯	$8.8 \times 10^{-1} \pm 2.3 \times 10^{-2}$	⋯	⋯
14	$6.1 \times 10^{-3} \pm 3.4 \times 10^{-4}$	$8.0 \times 10^{-4} \pm 8.9 \times 10^{-6}$	⋯	$7.8 \times 10^{-1} \pm 8.7 \times 10^{-3}$	369×167	⋯
15	$5.4 \times 10^{-3} \pm 5.0 \times 10^{-5}$	$1.2 \times 10^{-3} \pm 1.8 \times 10^{-5}$	⋯	$2.9 \times 10^{0} \pm 4.5 \times 10^{-2}$	159×78	⋯
16	$1.8 \times 10^{-2} \pm 4.7 \times 10^{-4}$	$5.4 \times 10^{-3} \pm 2.7 \times 10^{-5}$	⋯	$1.4 \times 10^{1} \pm 6.9 \times 10^{-2}$	⋯	⋯
17	$7.1 \times 10^{-3} \pm 4.9 \times 10^{-4}$	$8.5 \times 10^{-4} \pm 5.0 \times 10^{-5}$	47	$8.3 \times 10^{-1} \pm 4.8 \times 10^{-2}$	237×214	531×7
18	$1.2 \times 10^{-2} \pm 2.9 \times 10^{-4}$	$3.2 \times 10^{-3} \pm 5.8 \times 10^{-6}$	⋯	$8.1 \times 10^{0} \pm 1.5 \times 10^{-2}$	⋯	⋯
19	$1.3 \times 10^{-2} \pm 2.6 \times 10^{-4}$	$2.9 \times 10^{-3} \pm 9.6 \times 10^{-6}$	⋯	$7.3 \times 10^{0} \pm 2.4 \times 10^{-2}$	⋯	⋯
20	$1.2 \times 10^{-2} \pm 3.9 \times 10^{-4}$	$4.5 \times 10^{-3} \pm 6.9 \times 10^{-5}$	⋯	$4.4 \times 10^{0} \pm 6.8 \times 10^{-2}$	297×185	⋯
21	$1.4 \times 10^{-2} \pm 5.1 \times 10^{-4}$	$3.2 \times 10^{-3} \pm 6.1 \times 10^{-5}$	⋯	$3.1 \times 10^{0} \pm 6.0 \times 10^{-2}$	257×105	⋯
22	$2.4 \times 10^{-3} \pm 5.7 \times 10^{-5}$	$3.9 \times 10^{-4} \pm 1.9 \times 10^{-6}$	⋯	$9.8 \times 10^{-1} \pm 4.7 \times 10^{-3}$	⋯	⋯
23	⋯	$2.2 \times 10^{-4} \pm 1.3 \times 10^{-5}$	⋯	$5.6 \times 10^{-1} \pm 3.2 \times 10^{-2}$	⋯	⋯
24	⋯	$3.2 \times 10^{-4} \pm 1.3 \times 10^{-5}$	⋯	$8.1 \times 10^{-1} \pm 3.3 \times 10^{-2}$	⋯	⋯
25	⋯	$5.6 \times 10^{-3} \pm 2.1 \times 10^{-5}$	⋯	$1.8 \times 10^{0} \pm 6.7 \times 10^{-3}$	⋯	⋯
26	⋯	$2.9 \times 10^{-3} \pm 7.7 \times 10^{-5}$	⋯	$9.3 \times 10^{-1} \pm 2.5 \times 10^{-2}$	⋯	540×19
27	⋯	$1.4 \times 10^{-3} \pm 4.7 \times 10^{-5}$	⋯	$1.4 \times 10^{0} \pm 4.6 \times 10^{-2}$	⋯	466×349
28	⋯	$6.7 \times 10^{-4} \pm 3.3 \times 10^{-5}$	⋯	$1.7 \times 10^{0} \pm 8.3 \times 10^{-2}$	⋯	⋯
29	⋯	$2.1 \times 10^{-4} \pm 2.7 \times 10^{-6}$	⋯	$5.3 \times 10^{-1} \pm 6.8 \times 10^{-3}$	⋯	⋯

Appendix D
Pre-/protostellar Object Maps

We present the location of PPO catalogs at the continuum map of W51-E (Figure 23 and 24) and W51-IRS2 (Figures 25, 26, and 27).

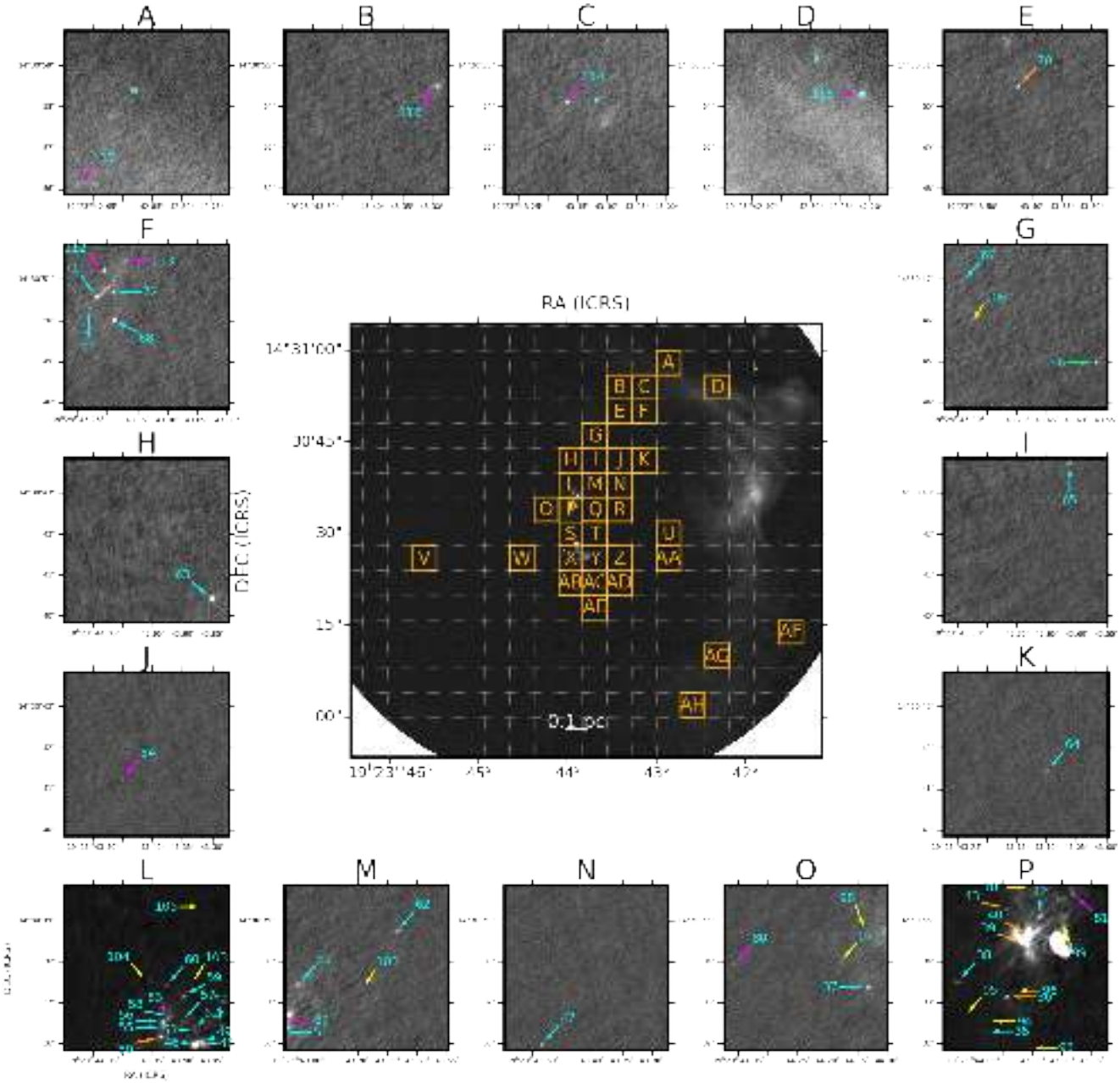

Figure 23. A map of PPOs in W51-E. In the central panel, subfields containing PPOs are labeled. Cutout images of each labeled grid are displayed in the side panels. The positions of the PPOs are annotated by a arrow with their ID and color representing their classification (cyan: dust dominated, orange: dust + free–free, green: free–free contaminated, magenta: only found at 1.3 mm, and yellow: only found at 3 mm). The cyan crosses mark PPOs included in the W51-IRS2 catalog. The background image is a 3 mm long-baseline continuum image. The color scaling in each inset is individually adjusted for better visual clarity.

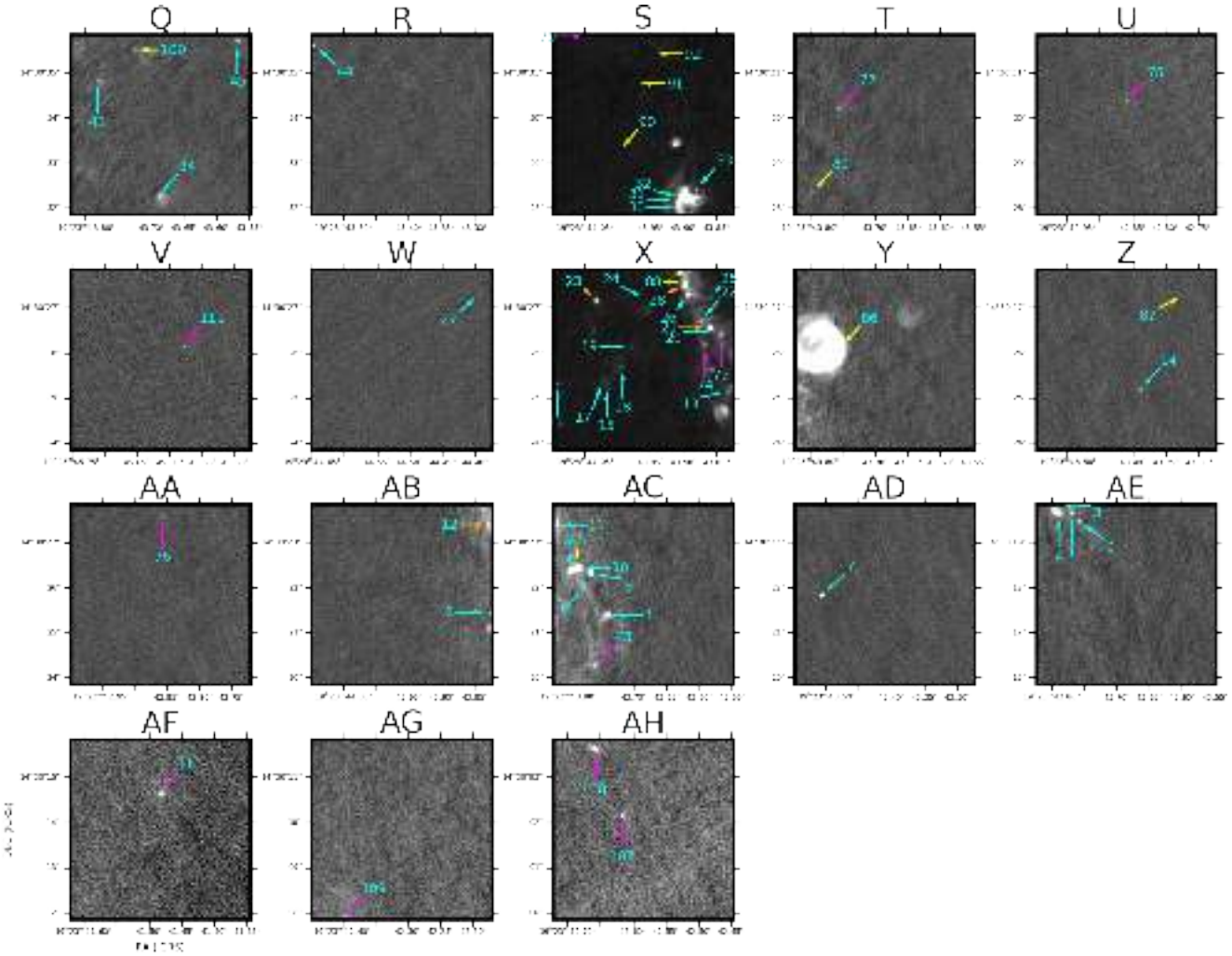

Figure 24. Figure 23 continued.

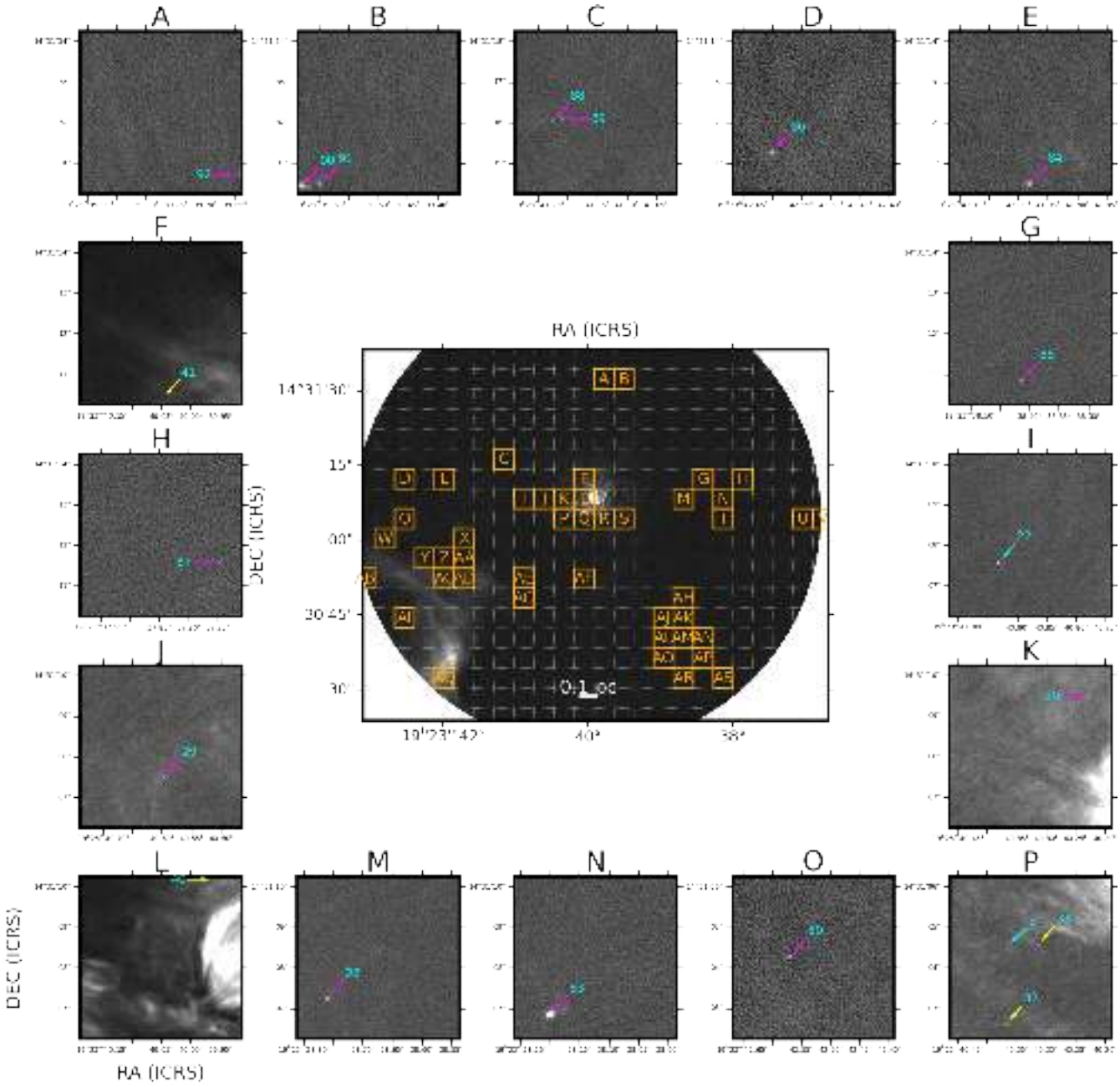

Figure 25. Same as Figure 23 but for W51-IRS2. The cyan crosses mark the PPOs in the W51-E catalog.

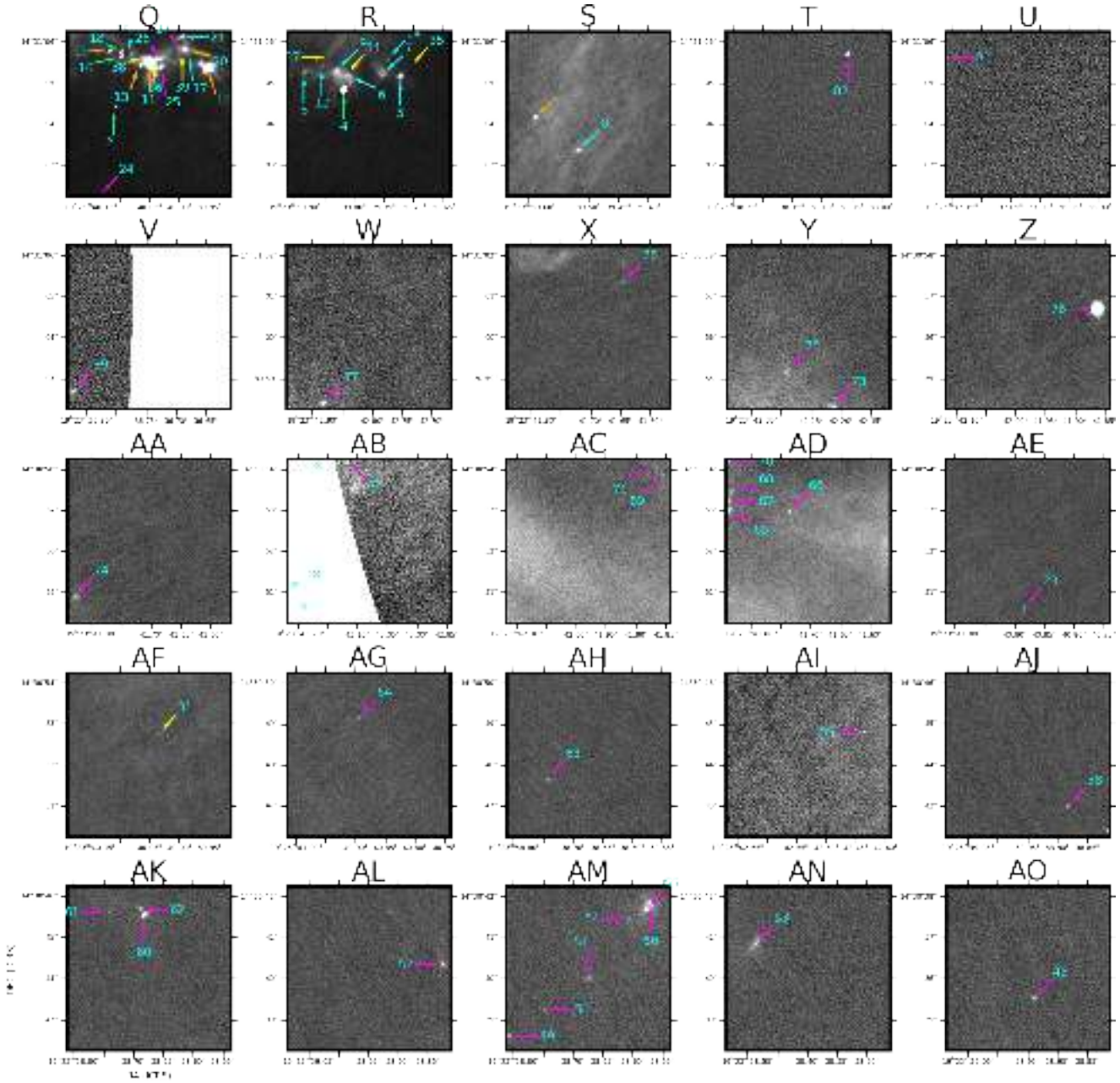

Figure 26. Figure 25 continued.

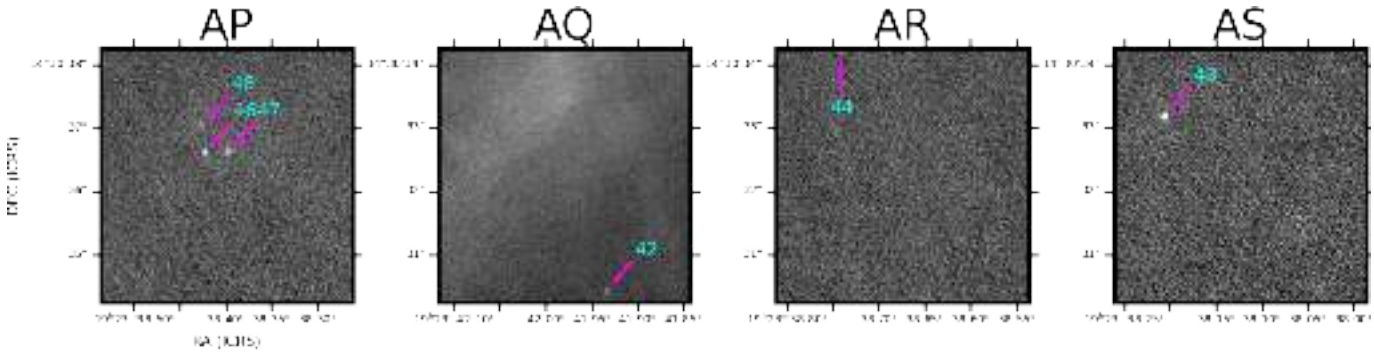

Figure 27. Figure 25 continued.

Appendix E
Pre-/protostellar Object Snapshots

We present the snapshot of 1.3 mm and 3 mm continuum image of PPOs in W51-E (Figures 28–31) and W51-IRS2 (Figures 32 and 33).

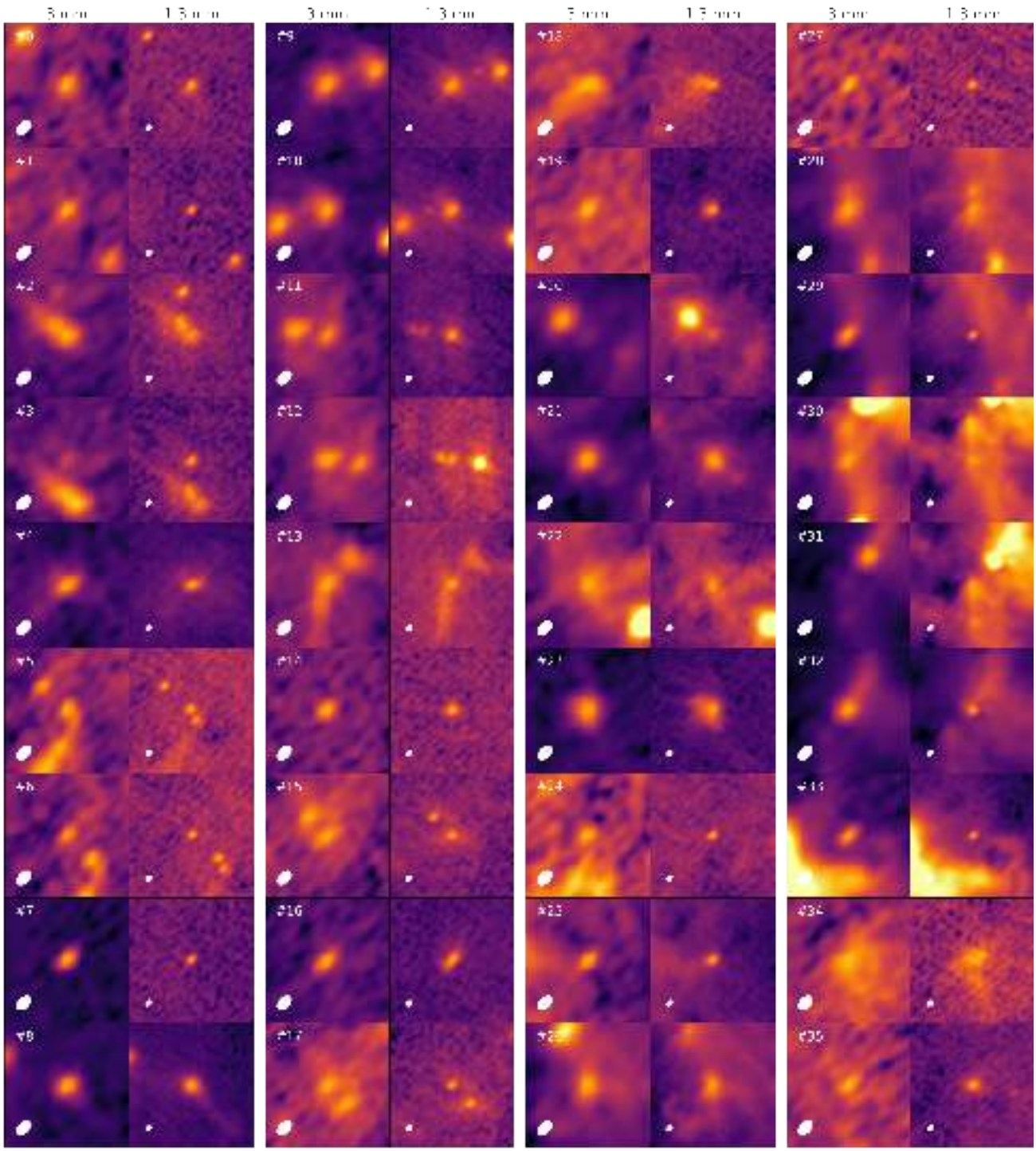

Figure 28. Snapshots of PPOs identified in the W51-E 1.3 mm and 3 mm continuum images. The color scale is normalized to the flux of the central object for clear visualization. The size of the image beam is represented as a filled ellipse at the left lower corner.

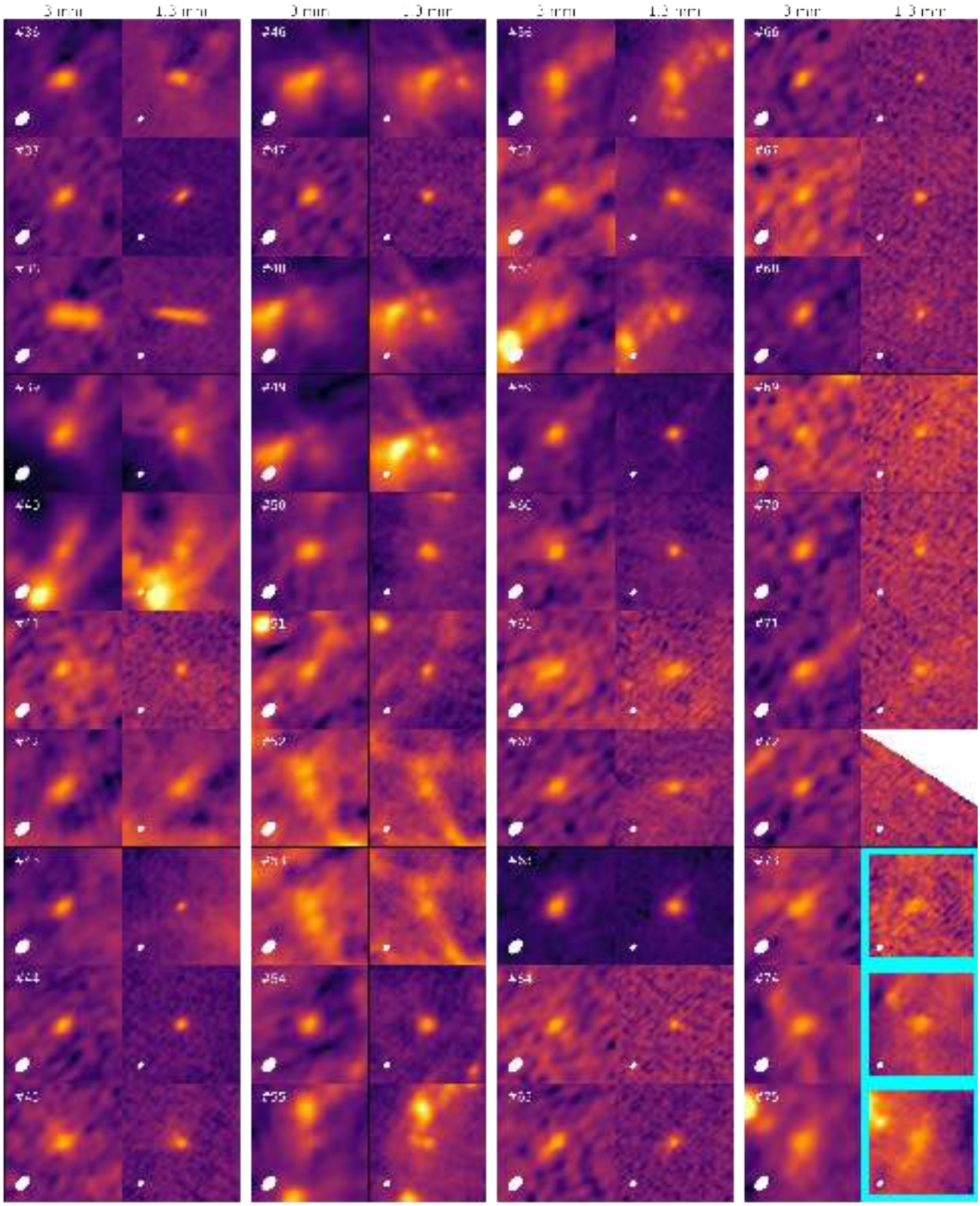

Figure 29. Figure 28 continued. The images of undetected sources in the `dendrogram` are surrounded by cyan squares.

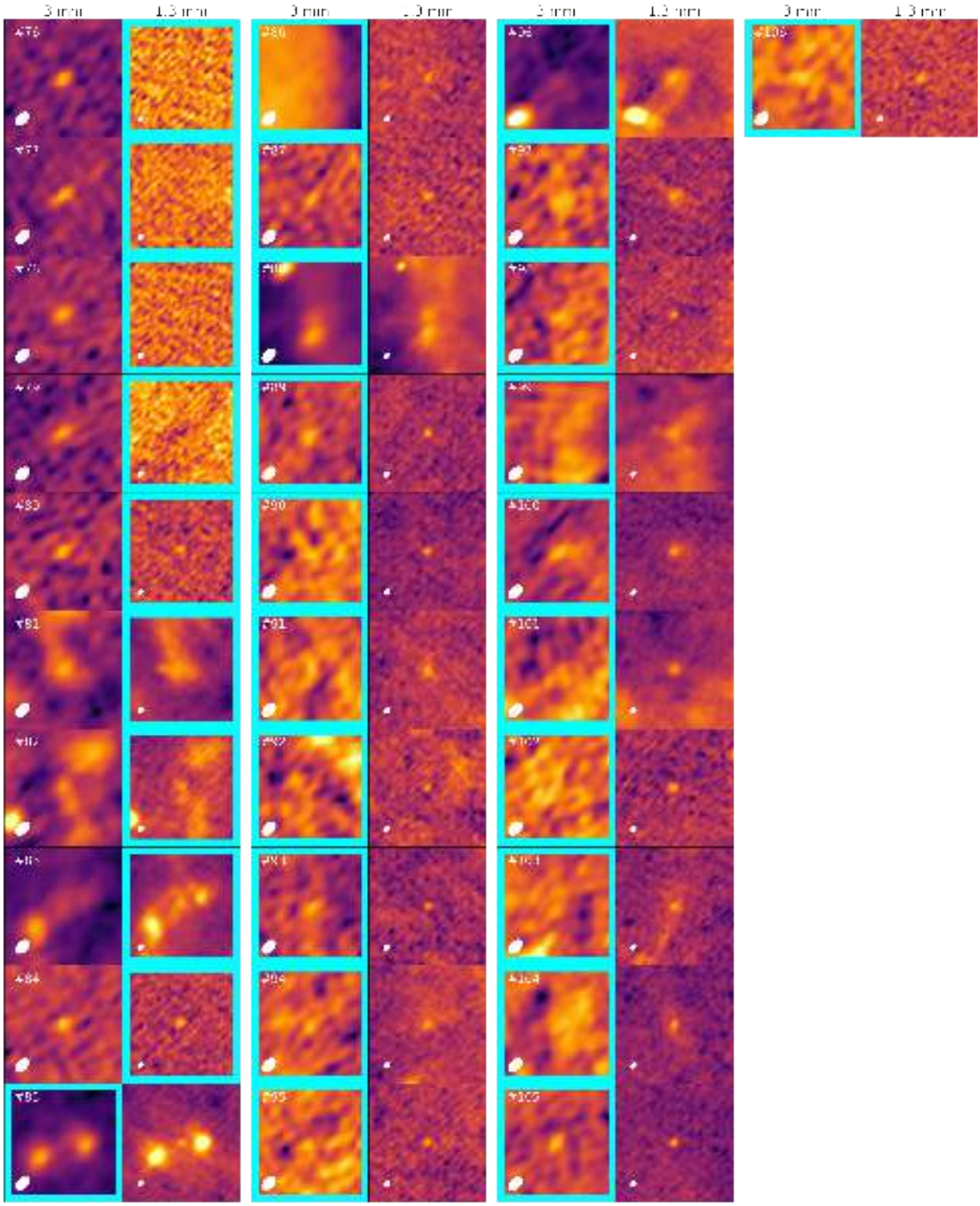

Figure 30. Figure 28 continued.

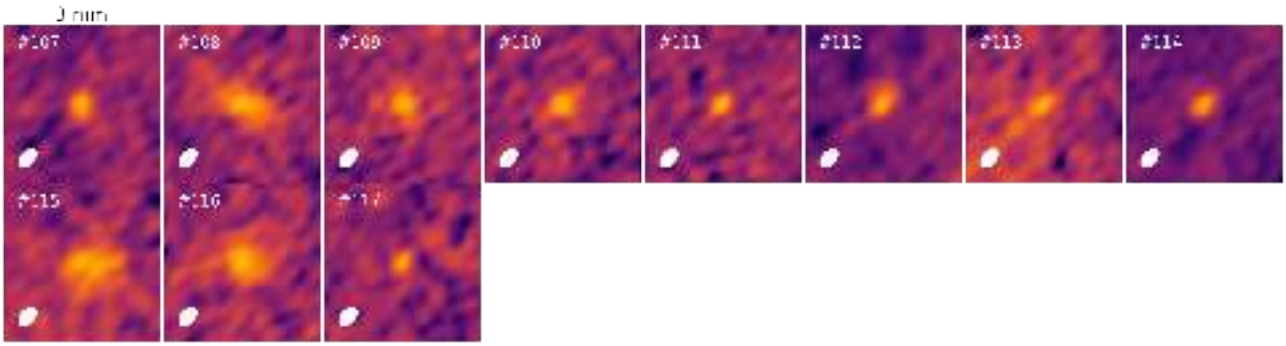

Figure 31. Figure 28 continued. For #107–117, the sky position of the 1.3 mm counterpart is out of the field of view.

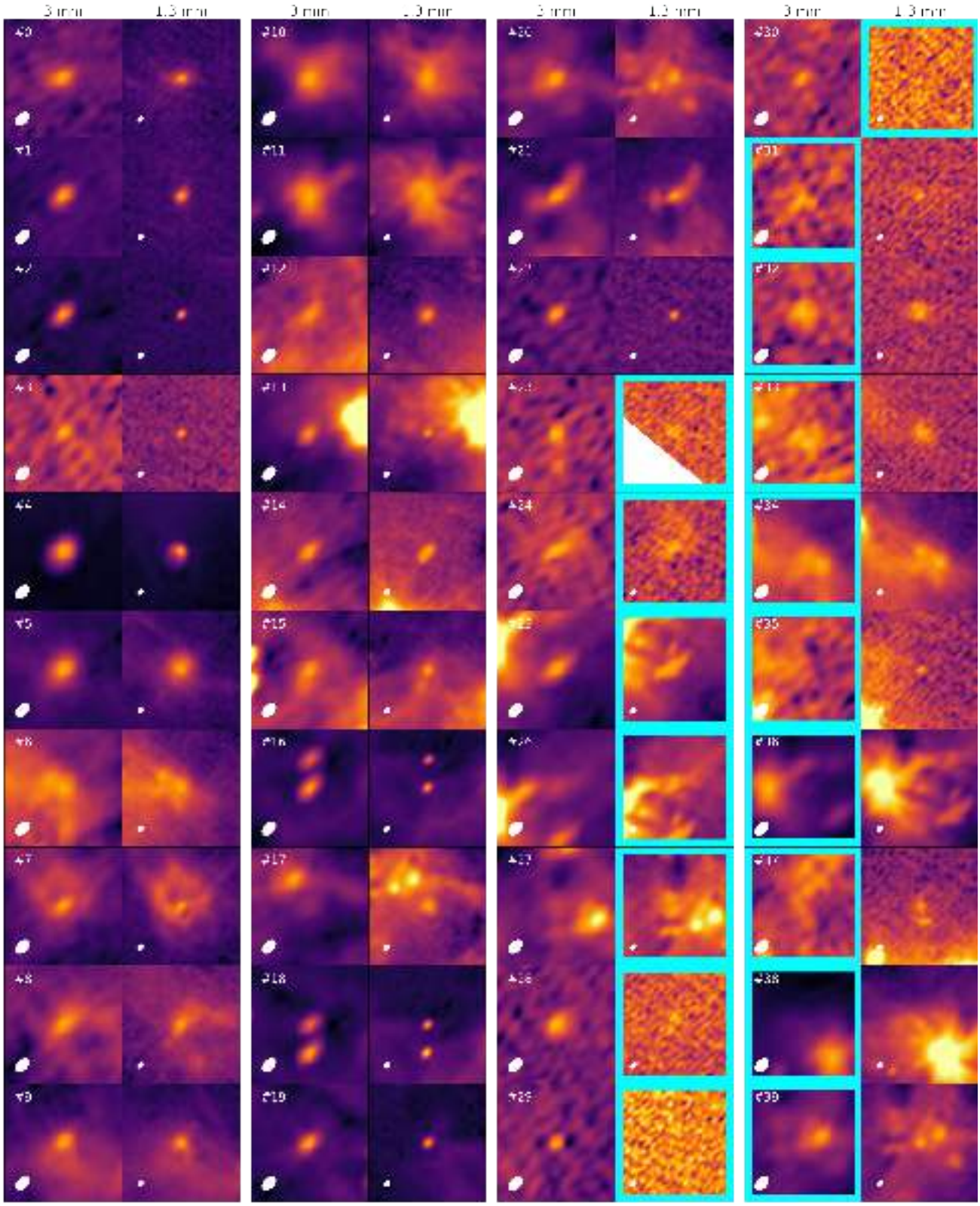

Figure 32. Snapshots of PPOs identified in W51-IRS2 1.3 mm and 3 mm continuum images. Sources #32–39 do not have a counterpart in the 1.3 mm field of view.

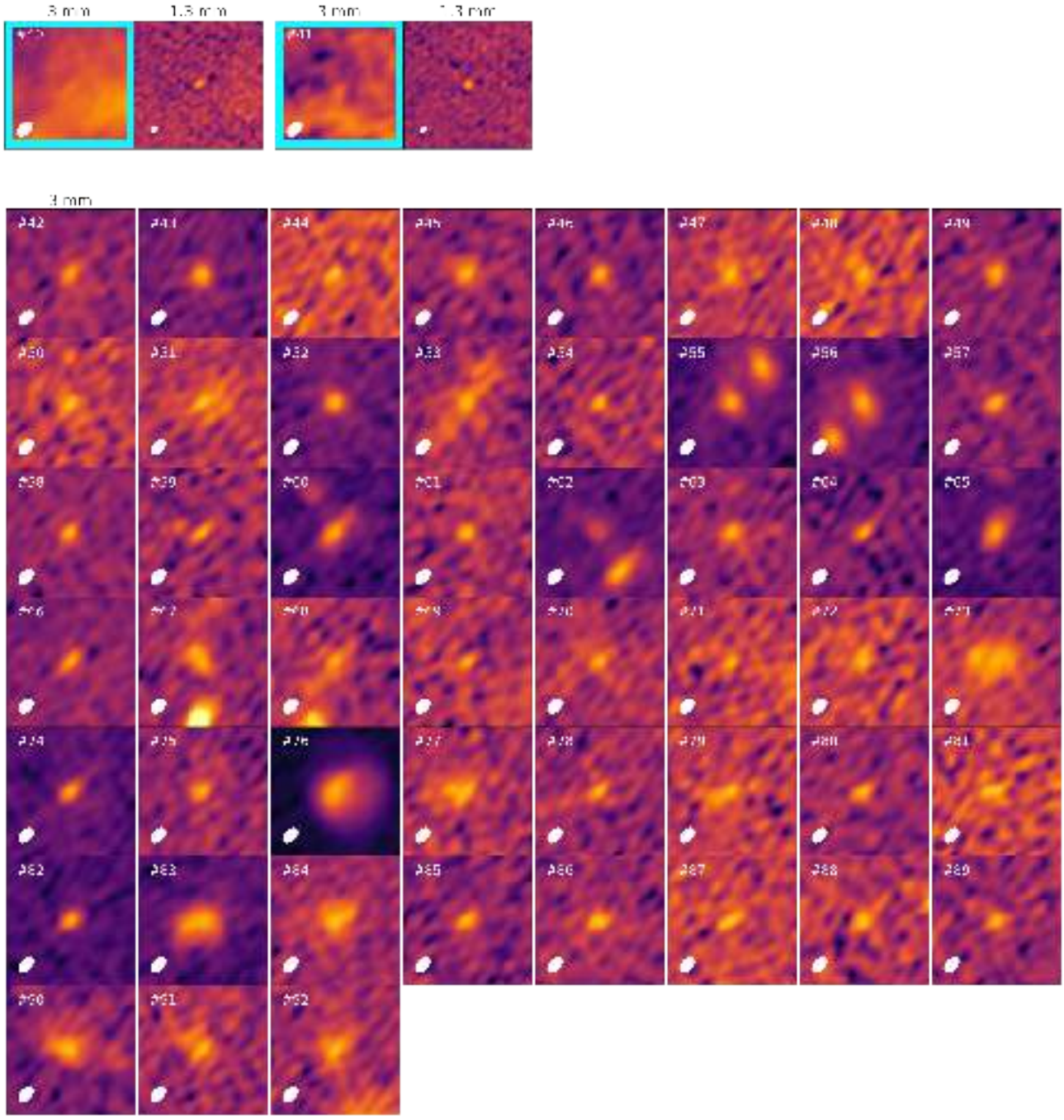

Figure 33. Figure 32 Continued. For #42–92, the sky position of the 1.3 mm counterpart is out of the field of view.

Appendix F
Ambiguous and Low-signal-to-noise-ratio Source Snapshots

We provide snapshots of ambiguous (Figures 34–36) and low-S/N sources (Figures 37 and 38) that were unselected in the final catalog of PPOs in Section 3.1. Sources identified by only one of the three independent observers are classified as ambiguous. In W51-E and W51-IRS2, 45 and 33 ambiguous sources are identified. Among the observers, we found different assessments of compactness, significance, or independence from the background for these sources. These ambiguous sources may particularly include substructures of diffuse dust emission and HCH II regions (e.g., #5 in W51-E, also known as w51e2w; C. Goddi et al. 2016). On the other hand, low-S/N sources are picked by more than two observers but are not identified in `dendrogram` due to their low S/N. In Figures 34–38, some sources have counterparts not classified as ambiguous or low-S/N objects; these counterparts are highlighted with cyan squares in the images. In some cases, these counterparts are real PPOs classified as single detection. For example, PPO #25 in W51-IRS2 has a single detection at 3 mm (Figure 32). Its 1.3 mm counterpart is classified as the #17 ambiguous source in Figure 36 as it is less centrally peaked. The sky positions of these sources are provided by electronic form at DOI:10.5281/zenodo.16235156.

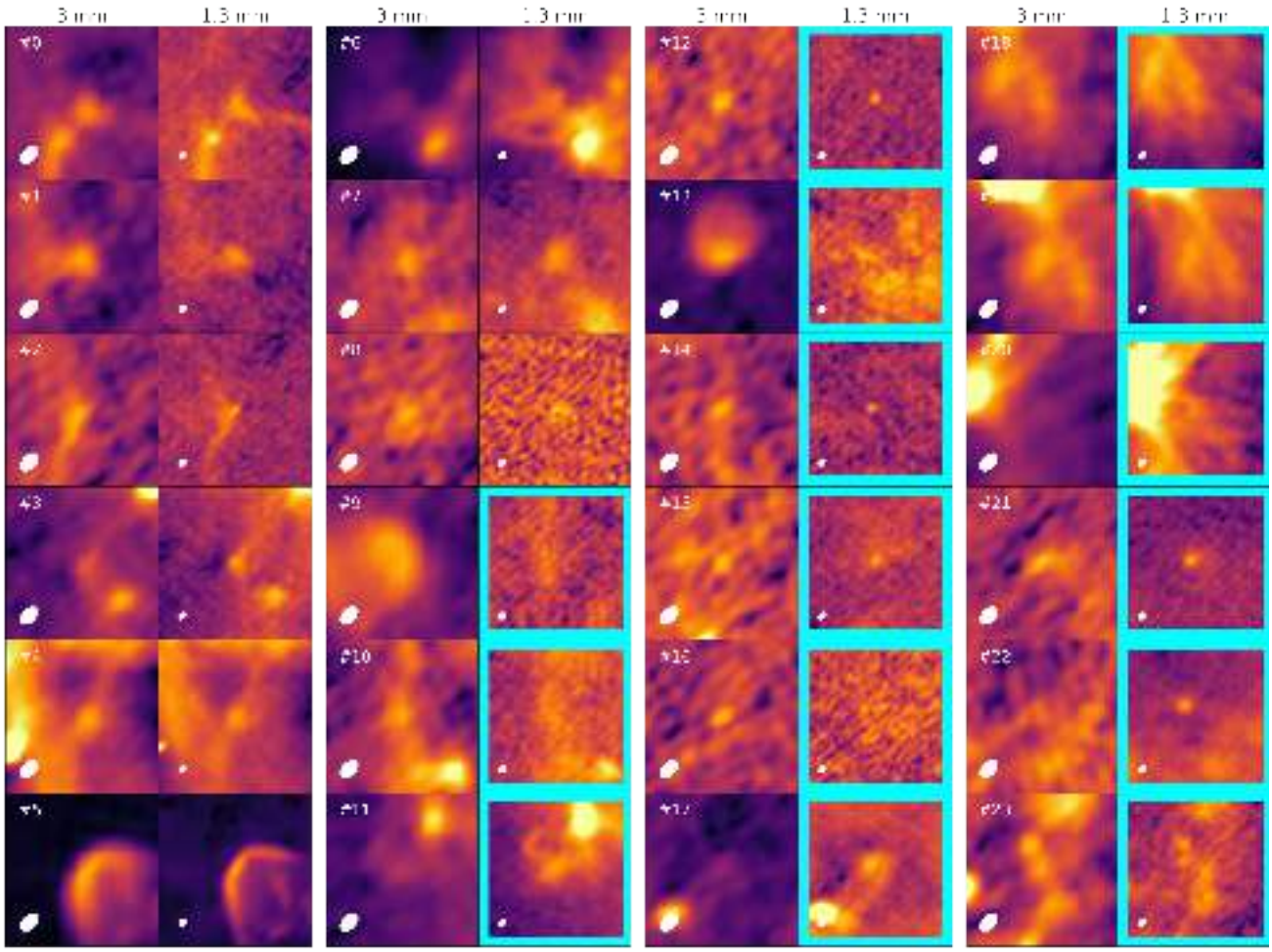

Figure 34. Snapshots of ambiguous sources that were not selected in the final catalog of PPOs in W51-E. The cyan square indicates the absence of the sources in the ambiguous object catalog.

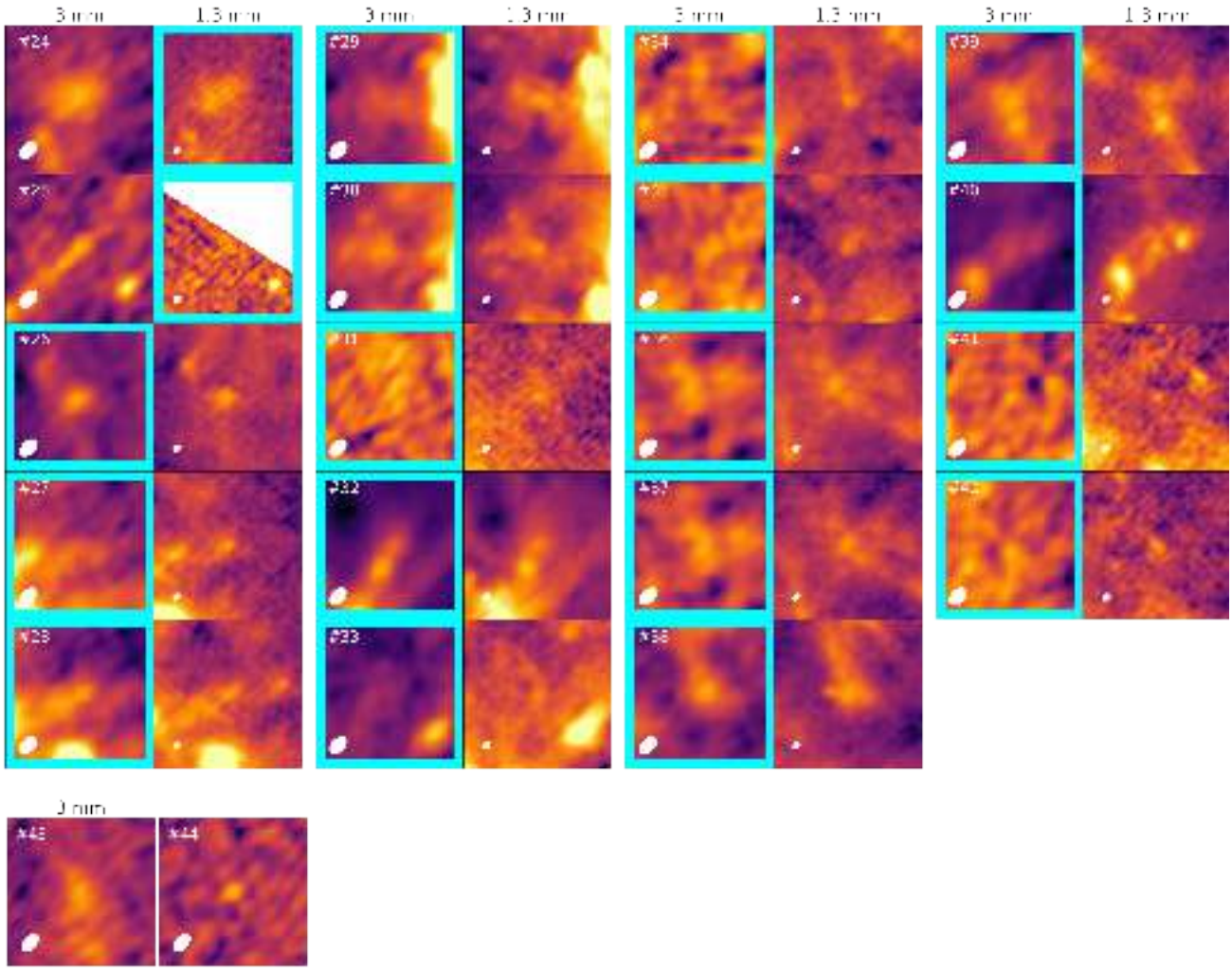

Figure 35. Figure 34 continued. The sources #43 and #44 are outside of the field of view of the 1.3 mm continuum image.

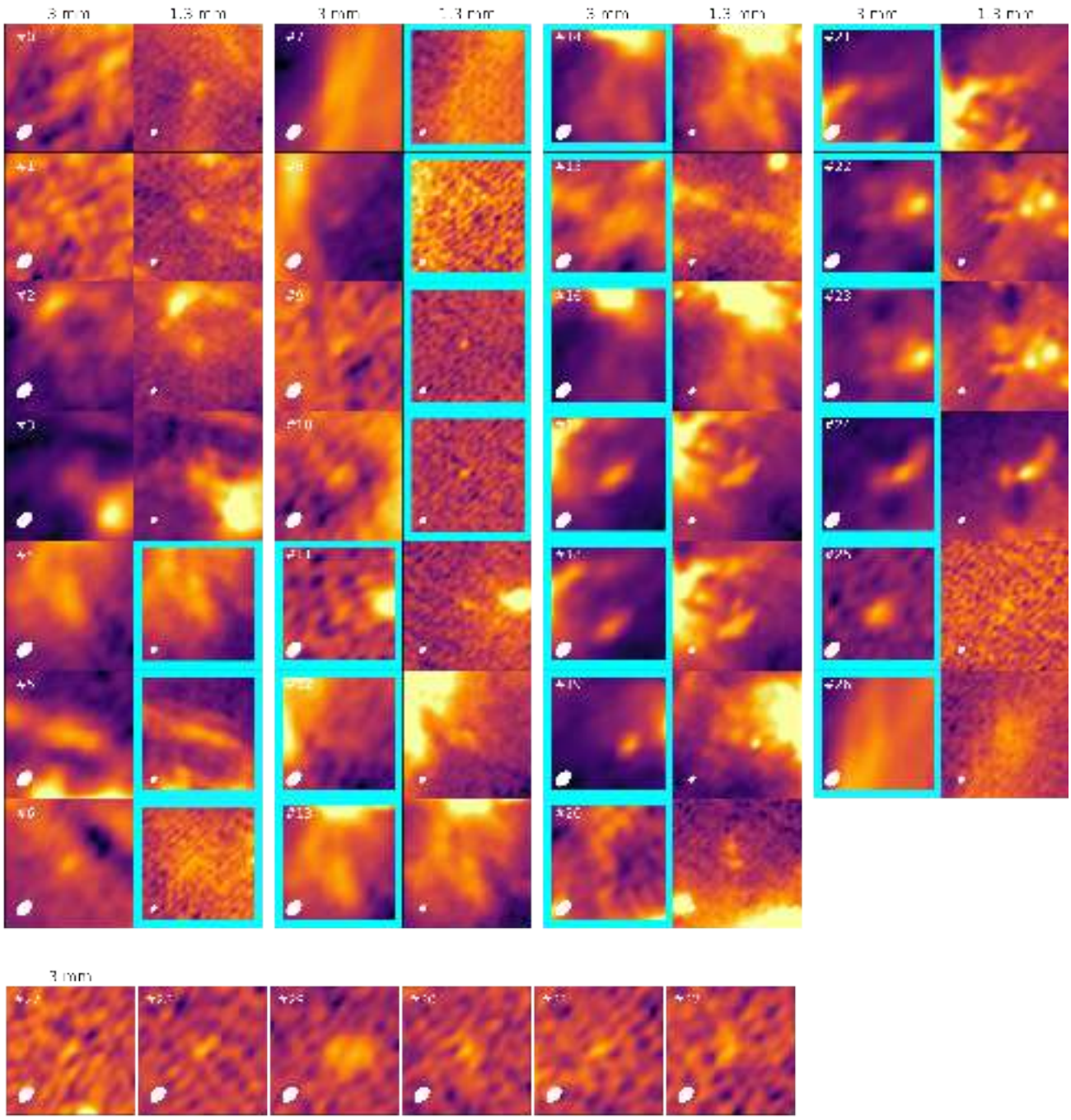

Figure 36. Snapshots of ambiguous sources in W51-IRS2. The sources #27–#32 are outside of the field of view of the 1.3 mm continuum image.

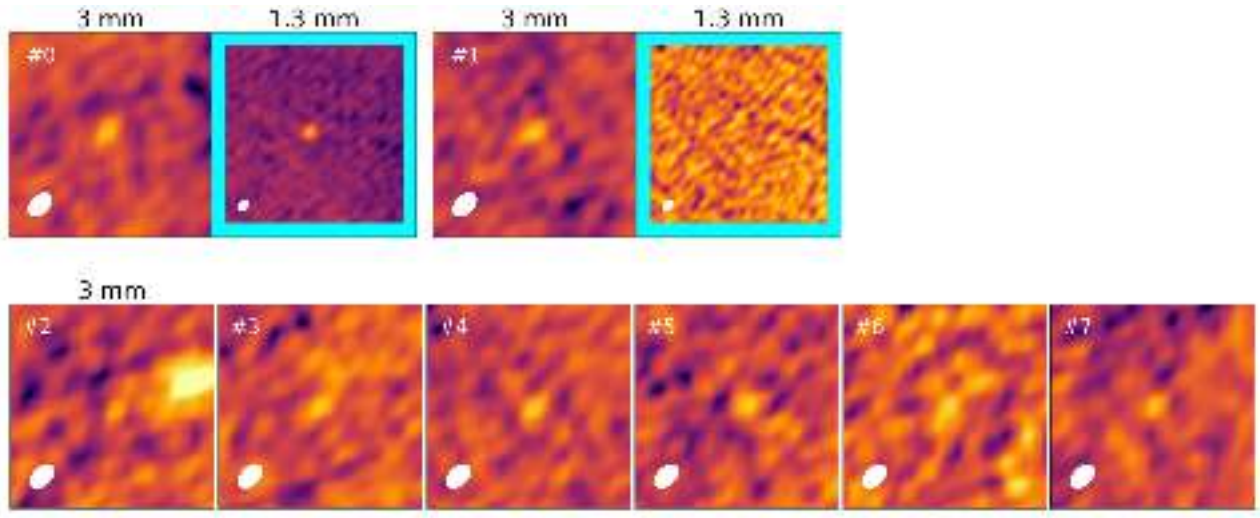

Figure 37. Snapshots of low-S/N sources in W51-E. Sources #2–#7 are outside of the field of view of the 1.3 mm continuum image.

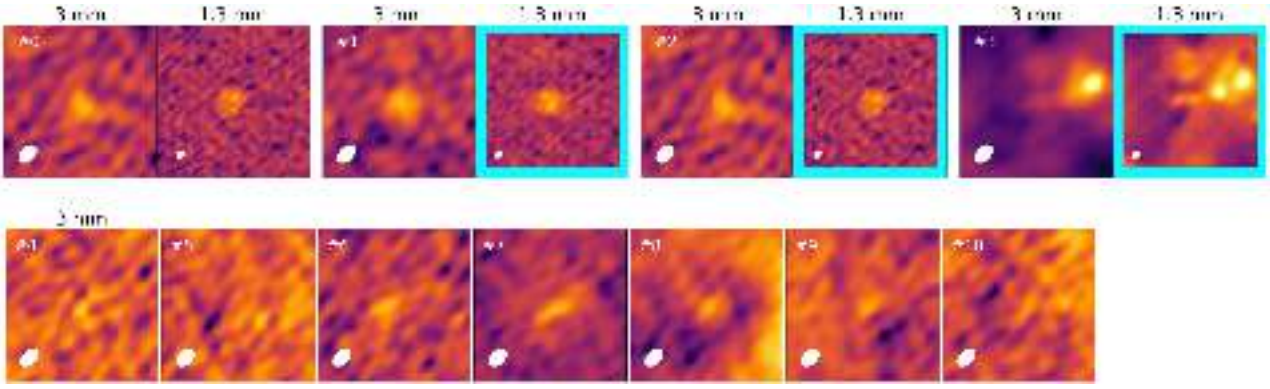

Figure 38. Figure 37 continued. The sources #4–#10 are outside of the field of view of the 1.3 mm continuum image.

ORCID iDs

T. Yoo https://orcid.org/0000-0003-2968-5333
A. Ginsburg https://orcid.org/0000-0001-6431-9633
N. Budaiev https://orcid.org/0000-0002-0533-8575
F. Motte https://orcid.org/0000-0003-1649-8002
A. M. Stutz https://orcid.org/0000-0003-2300-8200
L. Bronfman https://orcid.org/0000-0002-9574-8454
G. Busquet https://orcid.org/0000-0002-2189-6278
T. Csengeri https://orcid.org/0000-0002-6018-1371
J. Di Francesco https://orcid.org/0000-0002-9289-2450
D. J. Díaz-González https://orcid.org/0000-0002-6325-8717
C. Goddi https://orcid.org/0000-0002-2542-7743
A. Koley https://orcid.org/0000-0003-2713-0211
H.-L Liu https://orcid.org/0000-0003-3343-9645
F. Olguin https://orcid.org/0000-0002-8250-6827
P. Sanhueza https://orcid.org/0000-0002-7125-7685
L. A. Zapata https://orcid.org/0000-0003-2343-7937
Q. Zhang https://orcid.org/0000-0003-2384-6589

References

Álvarez-Gutiérrez, R. H., Stutz, A. M., Sandoval-Garrido, N., et al. 2024, A&A, 689, A74
Alves, J., Lombardi, M., & Lada, C. J. 2007, A&A, 462, L17
André, P., Men'shchikov, A., Bontemps, S., et al. 2010, A&A, 518, L102
Ansdell, M., Williams, J. P., Trapman, L., et al. 2018, ApJ, 859, 21
Armante, M., Gusdorf, A., Louvet, F., et al. 2024, A&A, 686, A122
Astropy Collaboration, Robitaille, T. P., Tollerud, E. J., et al. 2013, A&A, 558, A33
Astropy Collaboration, Price-Whelan, A. M., Sipőcz, B. M., et al. 2018, AJ, 156, 123
Bastian, N., Covey, K. R., & Meyer, M. R. 2010, ARA&A, 48, 339
Binney, J., & Tremaine, S. 1987, Galactic Dynamics (Princeton, NJ: Princeton Univ. Press)
Bonfand, M., Csengeri, T., Bontemps, S., et al. 2024, A&A, 687, A163
Bonnell, I. A., & Bate, M. R. 2002, MNRAS, 336, 659
Bonnell, I. A., Bate, M. R., Clarke, C. J., & Pringle, J. E. 2001, MNRAS, 323, 785
Bontemps, S., Motte, F., Csengeri, T., & Schneider, N. 2010, A&A, 524, A18
Brown, R. D., & Cragg, D. M. 1991, ApJ, 378, 445
Budaiev, N., Ginsburg, A., Jeff, D., et al. 2024, ApJ, 961, 4
Comrie, A., Wang, K.-S., Hsu, S.-C., et al. 2021, CARTA: Cube Analysis and Rendering Tool for Astronomy, Astrophysics Source Code Library, ascl:2103.031
Comrie, A., Wang, K.-S., Hwang, Y.-H., et al. 2024, CARTA: The Cube Analysis and Rendering Tool for Astronomy, v4.1.0, Zenodo, doi:10.5281/zenodo.15172686
Crapsi, A., van Dishoeck, E. F., Hogerheijde, M. R., Pontoppidan, K. M., & Dullemond, C. P. 2008, A&A, 486, 245
Csengeri, T., Bontemps, S., Wyrowski, F., et al. 2017, A&A, 600, L10
Davidson-Pilon, C. 2019, JOSS, 4, 1317
Dell'Ova, P., Motte, F., Gusdorf, A., et al. 2024, A&A, 687, A217
di Francesco, J., Evans, N. J., I., Caselli, P., et al. 2007, in Protostars and Planets V, ed. B. Reipurth, D. Jewitt, & K. Keil (Tucson, AZ: Univ. Arizona Press), 17

Díaz-González, D. J., Galván-Madrid, R., Ginsburg, A., et al. 2023, ApJS, 269, 55
Eisner, J. A., Greenhill, L. J., Herrnstein, J. R., Moran, J. M., & Menten, K. M. 2002, ApJ, 569, 334
Etoka, S., Gray, M. D., & Fuller, G. A. 2012, MNRAS, 423, 647
Fernández-López, M., Curiel, S., Girart, J. M., et al. 2011, AJ, 141, 72
Galván-Madrid, R., Liu, H. B., Izquierdo, A. F., et al. 2018, ApJ, 868, 39
Gaume, R. A., Johnston, K. J., & Wilson, T. L. 1993, ApJ, 417, 645
Genzel, R., Downes, D., Schneps, M. H., et al. 1981, ApJ, 247, 1039
Ghavamian, P., & Hartigan, P. 1998, ApJ, 501, 687
Ginsburg, A. 2017, arXiv:1702.06627
Ginsburg, A., & Goddi, C. 2019, AJ, 158, 208
Ginsburg, A., Bally, J., Battersby, C., et al. 2015, A&A, 573, A106
Ginsburg, A., Goss, W. M., Goddi, C., et al. 2016, A&A, 595, A27
Ginsburg, A., Goddi, C., Kruijssen, J. M. D., et al. 2017, ApJ, 842, 92
Ginsburg, A., Csengeri, T., Galván-Madrid, R., et al. 2022, A&A, 662, A9
Girichidis, P., Federrath, C., Banerjee, R., & Klessen, R. S. 2012, MNRAS, 420, 613
Goddi, C., Ginsburg, A., & Zhang, Q. 2016, A&A, 589, A44
Goddi, C., Ginsburg, A., Maud, L. T., Zhang, Q., & Zapata, L. A. 2020, ApJ, 905, 25
Guszejnov, D., & Hopkins, P. F. 2015, MNRAS, 450, 4137
Guszejnov, D., & Hopkins, P. F. 2016, MNRAS, 459, 9
Harris, C. R., Millman, K. J., van der Walt, S. J., et al. 2020, Natur, 585, 357
Henkel, C., Wilson, T. L., Asiri, H., & Mauersberger, R. 2013, A&A, 549, A90
Hennebelle, P., & Grudić, M. Y. 2024, ARA&A, 62, 63
Hildebrand, R. H. 1983, QJRAS, 24, 267
Hosek, M. W. J., Lu, J. R., Anderson, J., et al. 2019, ApJ, 870, 44
Hoyle, F. 1953, ApJ, 118, 513
Hunter, J. D. 2007, CSE, 9, 90
Imai, H., Watanabe, T., Omodaka, T., et al. 2002, PASJ, 54, 741
Kelly, B. C. 2007, ApJ, 665, 1489
Keto, E., Zhang, Q., & Kurtz, S. 2008, ApJ, 672, 423
Koch, P. M., Tang, Y.-W., Ho, P. T. P., et al. 2022, ApJ, 940, 89
Kong, S. 2019, ApJ, 873, 31
Krumholz, M. R., Klein, R. I., & McKee, C. F. 2007, ApJ, 656, 959
Krumholz, M. R. 2015, arXiv:1511.03457
Kumar, M. S. N., Kamath, U. S., & Davis, C. J. 2004, MNRAS, 353, 1025
Li, J. I.-H., Liu, H. B., Hasegawa, Y., & Hirano, N. 2017, ApJ, 840, 72
Li, S., Sanhueza, P., Beuther, H., et al. 2024, NatAs, 8, 472
Lin, Y., Csengeri, T., Wyrowski, F., et al. 2019, A&A, 631, A72
Louvet, F., Motte, F., Hennebelle, P., et al. 2014, A&A, 570, A15
Louvet, F., Sanhueza, P., Stutz, A., et al. 2024, A&A, 690, A33
Lu, J. R., Do, T., Ghez, A. M., et al. 2013, ApJ, 764, 155
Lu, X., Cheng, Y., Ginsburg, A., et al. 2020, ApJL, 894, L14
Maia, F. F. S., Moraux, E., & Joncour, I. 2016, MNRAS, 458, 3027
Marsh, K. A., Whitworth, A. P., & Lomax, O. 2015, MNRAS, 454, 4282
McKee, C. F., & Tan, J. C. 2002, Natur, 416, 59
McKee, C. F., & Tan, J. C. 2003, ApJ, 585, 850
McMullin, J. P., Waters, B., Schiebel, D., Young, W., & Golap, K. 2007, in ASP Conf. Ser. 376, Astronomical Data Analysis Software and Systems XVI, ed. R. A. Shaw, F. Hill, & D. J. Bell (San Francisco, CA: ASP), 127
Men'shchikov, A. 2021, A&A, 649, A89
Morii, K., Sanhueza, P., Nakamura, F., et al. 2023, ApJ, 950, 148
Morii, K., Sanhueza, P., Zhang, Q., et al. 2024, ApJ, 966, 171
Morita, K.-I., Hasegawa, T., Ukita, N., Okumura, S. K., & Ishiguro, M. 1992, PASJ, 44, 373
Motte, F., Andre, P., & Neri, R. 1998, A&A, 336, 150
Motte, F., Bontemps, S., & Louvet, F. 2018, ARA&A, 56, 41
Motte, F., Bontemps, S., Csengeri, T., et al. 2022, A&A, 662, A8
Motte, F., Pouteau, Y., Nony, T., et al. 2025, A&A, 694, A24
Newville, M., Stensitzki, T., Allen, D. B., & Ingargiola, A. 2015, LMFIT: Non-Linear Least-Square Minimization and Curve-Fitting for Python, v0.8.0, Zenodo, doi:10.5281/zenodo.11813
Nony, T., Galván-Madrid, R., Motte, F., et al. 2023, A&A, 674, A75
Offner, S. S. R., Clark, P. C., Hennebelle, P., et al. 2014, in PPVII, 53
Offner, S. S. R., Moe, M., Kratter, K. M., et al. 2023, in ASP Conf. Ser. 534, Protostars and Planets VII, ed. S. Inutsuka et al. (San Francisco, CA: ASP), 275
Oh, S., & Kroupa, P. 2016, A&A, 590, A107
Oh, S., Kroupa, P., & Pflamm-Altenburg, J. 2015, ApJ, 805, 92
Okumura, S.-i., Mori, A., Nishihara, E., Watanabe, E., & Yamashita, T. 2000, ApJ, 543, 799
Ossenkopf, V., & Henning, T. 1994, A&A, 291, 943
Padoan, P., & Nordlund, Å. 2002, ApJ, 576, 870
Padoan, P., Pan, L., Juvela, M., Haugbølle, T., & Nordlund, Å. 2020, ApJ, 900, 82
Padoan, P., Pelkonen, V. M., Juvela, M., Haugbølle, T., & Nordlund, Å. 2023, MNRAS, 522, 3548
Palau, A., Ballesteros-Paredes, J., Vázquez-Semadeni, E., et al. 2015, MNRAS, 453, 3785
Palau, A., Zhang, Q., Girart, J. M., et al. 2021, ApJ, 912, 159
Pan, S., Liu, H.-L., & Qin, S.-L. 2024, ApJ, 960, 76
Phillips, C., & van Langevelde, H. J. 2005, in ASP Conf. Ser. 340, Future Directions in High Resolution Astronomy, ed. J. Romney & M. Reid (San Francisco, CA: ASP), 342
Pokhrel, R., Myers, P. C., Dunham, M. M., et al. 2018, ApJ, 853, 5
Pouteau, Y., Motte, F., Nony, T., et al. 2022, A&A, 664, A26
Reipurth, B., & Clarke, C. 2001, AJ, 122, 432
Richardson, T., Ginsburg, A., Indebetouw, R., & Robitaille, T. P. 2024, ApJ, 961, 188
Rong, J., Qin, S.-L., Zapata, L. A., et al. 2016, MNRAS, 455, 1428
Rosolowsky, E. W., Pineda, J. E., Kauffmann, J., & Goodman, A. A. 2008, ApJ, 679, 1338
Salpeter, E. E. 1955, ApJ, 121, 161
Sandoval-Garrido, N. A., Stutz, A. M., & Álvarez-Gutiérrez, R. H. 2025, A&A, 696, A202
Sanhueza, P., Contreras, Y., Wu, B., et al. 2019, ApJ, 886, 102
Sanhueza, P., Girart, J. M., Padovani, M., et al. 2021, ApJL, 915, L10
Sato, M., Reid, M. J., Brunthaler, A., & Menten, K. M. 2010, ApJ, 720, 1055
Simpson, R. J., Nutter, D., & Ward-Thompson, D. 2008, MNRAS, 391, 205
Tang, M., Palau, A., Zapata, L. A., & Qin, S.-L. 2022, A&A, 657, A30
Tobin, J. J., Sheehan, P. D., Megeath, S. T., et al. 2020, ApJ, 890, 130
Townsley, L. K., Broos, P. S., Garmire, G. P., et al. 2014, ApJS, 213, 1
Vázquez-Semadeni, E., Palau, A., Ballesteros-Paredes, J., Gómez, G. C., & Zamora-Avilés, M. 2019, MNRAS, 490, 3061
Virtanen, P., Gommers, R., Oliphant, T. E., et al. 2020, NatMe, 17, 261
Wainer, T. M., Williams, B. F., Johnson, L. C., et al. 2024, AJ, 168, 86
Waskom, M. L. 2021, JOSS, 6, 3021
Weisz, D. R., Johnson, L. C., Foreman-Mackey, D., et al. 2015, ApJ, 806, 198
Wilson, T. L., Rohlfs, K., & Hüttemeister, S. 2013, Tools of Radio Astronomy (Berlin: Springer)
Xu, F., Wang, K., Liu, T., et al. 2024, ApJS, 270, 9
Xu, Y., Reid, M. J., Menten, K. M., et al. 2009, ApJ, 693, 413
Yang, D., Liu, H.-L., Tej, A., et al. 2023, ApJ, 953, 40
Yoo, T., & Ginsburg, A. 2024, TGIF: Two d Gaussian In Fitting, v1, Zenodo, doi:10.5281/zenodo.13973837
Zapata, L. A., Ho, P. T. P., Schilke, P., et al. 2009, ApJ, 698, 1422
Zapata, L. A., Tang, Y.-W., & Leurini, S. 2010, ApJ, 725, 1091
Zhang, Q., & Ho, P. T. P. 1997, ApJ, 488, 241
Zhang, Q., Wang, Y., Pillai, T., & Rathborne, J. 2009, ApJ, 696, 268
Zhang, Q., Wang, K., Lu, X., & Jiménez-Serra, I. 2015, ApJ, 804, 141